2010

Quantifying the impact of data quality on searches for gravitational waves from binary coalescing systems with LIGO

Jacob Peter Slutsky
Louisiana State University and Agricultural and Mechanical College, jsluts1@tigers.lsu.edu

QUANTIFYING THE IMPACT OF DATA QUALITY ON SEARCHES FOR GRAVITATIONAL WAVES FROM BINARY COALESCING SYSTEMS WITH LIGO

A Dissertation

Submitted to the Graduate Faculty of
the Louisiana State University and
Agricultural and Mechanical College
in partial fulfillment of the
requirements for the degree of
Doctor of Philosophy

in

The Department of Physics and Astronomy

by
Jacob Peter Slutsky
B.S., The University of Michigan, 2004
M.S., Louisiana State University, 2008
August, 2010

To David and Nancy Slutsky, for inspiring and supporting my interest in science.

Acknowledgments

I would like to thank Gabriela Gonzalez for hiring me on from the start of my time at LSU, for advising me on my path through academics and research, and for showing perhaps superhuman patience with me. I would like to thank Keith Riles for giving me my first non-retail job, introducing me to research and LIGO, and continuing to occasionally offer good advice and assistance long after I was no longer his responsibility.

I would like to gratefully acknowledge professors Jeffrey Blackmon, Joel Tohline, Joseph Giaime, Hwang Lee, and James Madden, for agreeing to take the time and effort of serving on my thesis committee.

I would like to thank the entire Inspiral/CBC group for their helping me to understand the searches, their code, my code, and for giving me all those triggers to work with in the first place. In particular, I'd like to thank Patrick Brady, Duncan Brown, Stephen Fairhurst, Nick Fotopoulis, Drew Keppel, and Eirini Messaritaki.

I would also like to thank the entire Detchar/Glitch group, for their collaboration in stemming the seemingly infinite tide of blips and glitches in the data. I'd like to specifically thank Laura Cadonati, Marco Cavaglia, Nelson Christenson, John Zweizig, Josh Smith, Andrew Lundgren, Larne Pekowsky.

Thanks to my fellow Astrowatchers, especially first shifters Berit Bernake, Pinkesh Patel, Evan Goetz, Phillip Roberts, and Junyi Zang. I'd also like to thank Matt West and Nicolas Smith in particular for help along the way. I would like to thank Anamaria Effler for teaching me much of what I know about H2 and interferometer operations in general, Fred Raab for supporting Astrowatch with gusto, and all the LHO staff for their indispensable help.

I'd like to thank Rupal Amin, Sarah Caudill, Chad Hanna, Jeff Kissel, Andres Rodriguez, Kate Dooley, Tobin Fricke, and all my fellow students. In particular, thanks to Chad for wise advice, patient explanations, and this LaTeX template, and thanks to Tobin for helping fix my laptop that broke 10 days before my defense.

Thank you Rachel, for maintaining my sanity through it all.

Table of Contents

List of Tables

List of Figures

Abstract

Gravitational waves are ripples in space-time itself, predicted by Einstein's General theory of relativity, which propagate at the speed of light and are not scattered or extinguished by passing through matter almost at all. In particular, the gravitational waves from the coalescences of binary systems of compact objects, such as neutron stars and black holes, are exciting prospects for observation. The Laser Interferometer Gravitational-wave Observatory experiment intends to make the first direct measurement of gravitational waves, and use the results to uncover new astrophysics. These observations will not be limited by extinction from dust and gas, and will probe astrophysical systems at distances of tens of millions to hundreds of millions of parsecs. The LIGO Scientific Collaboration searches for gravitational waves from a variety of astrophysical sources amongst this data. These searches are complicated by the presence of transients of non-astrophysical origin in the interferometer data. Control system and equipment malfunctions, as well as coupling from ground motions and electromagnetic fields, are the most common noises that detract from the LIGO data quality. These sources of noise increase the false alarm rate for gravitational wave searches, and need to be vetoed to search the data effectively for detections, or to set upper limits properly. Vetoes for the searches are created from the available data quality information, and their effect on the overall sensitivity of LIGO to these sources must be analyzed. During the S5 science run, I evaluated the data quality information for use as vetoes for the LIGO search for compact binary coalescences. The use of these vetoes made this search more sensitive to distant gravitational radiation sources by decreasing the non-astrophysical background from noise transients. In this dissertation, I quantify the impact of data quality on searches for gravitational waves with LIGO, and the resulting increased sensitivity to binary coalescing systems.

1. Gravitational Waves: Theory and Detection

1.1 Introduction

Historically, humanity has observed the stars and attempted to explain their properties. With the invention of telescopes, especially the observation of light far outside of the human visual range, astronomers have greatly increased understanding of the nature and composition of the universe. Observations of high energy charged particles, so-called cosmic rays, and neutrinos have expanded observations of the universe beyond electromagnetic radiation. Today, astronomers examine objects up to billions of light-years from the Earth. Thus far, observations of such distant objects have been performed using only their electromagnetic radiation. As effective as this has been, a cloud of interstellar gas or dust can completely obscure most frequencies of light, blocking from view the universe behind it. Such limitations are inherent in the use of light to probe the distant universe. The galactic magnetic field deflects all but the highest energy cosmic rays, and those with the closest sources, making direct astronomy more difficult. Neutrinos are abundantly produced in the Sun and Earth, and change type while travelling over short distances, complicating their use to investigate extra-galactic events.

Within the past 50 years, scientists and astronomers have begun preparing for an entirely new form of astronomical observation, the detection of gravitational waves. Predicted by Einstein's *General Theory of Relativity*, these weak ripples in space and time emanate in the wake of accelerating massive systems, and are neither scattered nor extinguished by intervening matter almost at all. The most developed of these projects is the Laser Interferometer Gravitational Wave Observatory (LIGO) (1), funded by the National Science Foundation, which measures differential changes in the arm lengths of interferometers. Amongst this data, the LIGO Scientific Collaboration (LSC) (2) searches for gravitational waves from a variety of astrophysical sources.

These searches are complicated by the presence of transients of non-astrophysical origin in the interferometer data. These transients increase the false alarm rate for gravitational wave searches, and need to be vetoed to search the data effectively for detections, or to set upper limits properly. This Chapter gives and overview of the physics and likely sources of gravitational radiation, of the LIGO interferometers, and of the methods and challenges involved in searching for this radiation in the LIGO data.

1.2 Gravitational Radiation

In General Relativity, the space-time separation of events is given by

$$ds^2 = g_{\mu\nu} dx^\mu dx^\nu \tag{1.1}$$

where ds is the space-time interval, and g is the metric, which encodes all of the information about space-time curvature(3; 4). The relationship of mass-energy in space to the curvature of said space is defined by Einstein's equation

$$G_{\mu\nu} = 8\pi G T_{\mu\nu}, \tag{1.2}$$

where on the right-hand side $T_{\mu\nu}$ is the energy-momentum 4-tensor, and on the left-hand side $G_{\mu\nu}$ is the Einstein 4-tensor, which is calculated from its derivatives. If we first try to approach these coupled, nonlinear, differential equations by way of looking for weak effects, we can define the metric such that

$$g_{\mu\nu} = \eta_{\mu\nu} + h_{\mu\nu}, \tag{1.3}$$

where η is the Minkowski metric (flat-space), and $|h|$ is a perturbation from uncurved space-time such that we can expand the left-hand side of Eqn 1.2 and keep only the terms to first order in $|h|$(5). Far from whatever source is causing the perturbation (see Chapter 1.3), we can take $T_{\mu\nu} = 0$. The choice of the "Transverse Traceless" gauge reduces 1.2 to a wave equation in vacuum:

$$\left(\nabla^2 - \frac{1}{c^2}\frac{\partial^2}{\partial t^2}\right) h_{\mu\nu} = 0. \tag{1.4}$$

The transverse nature of the gauge means that the curvature will be transverse to the direction of propagation of the wave, which by nature of Eqn 1.4 will propagate at the speed of light. Explicitly, being transverse means that $h_{\mu\nu}$ will have no components not contained in the transverse spatial coordinates (x and y), and being traceless requires the form:

$$h_{\mu\nu} = \begin{array}{c} \\ t \\ x \\ y \\ z \end{array} \begin{array}{c} \begin{array}{cccc} t & x & y & z \end{array} \\ \begin{pmatrix} 0 & 0 & 0 & 0 \\ 0 & h_+ & h_\times & 0 \\ 0 & h_\times & -h_+ & 0 \\ 0 & 0 & 0 & 0 \end{pmatrix} \end{array} \tag{1.5}$$

with h_+ and $h_\times$ conveniently labeling the two possible polarizations of this radiation. This wave travels in direction z at the speed of light c. From conservation of energy and angular momentum, we find no mono-polar or dipolar component to the source distribution will produce radiation (3; 5), so the leading order is the quadrapole moment. The effect of this quadrapolar radiation on a ring of particles shown below, in Figure 1.2. The electromagnetic interactions of particles in solids acts in opposition to this distortion, so particles not rigidly connected experience the largest displacement. This distortion of coordinate separation of free non-interacting masses is the effect searched for by LIGO.

1.3 Gravitational Wave Sources

The LIGO Observatory was designed to be sensitive to gravitational radiation from astrophysical sources. There are four types of sources that are believed to emit gravitational radiation in the sensitive frequency band of LIGO. These sources include a stochastic background, continuous-wave sources, unmodeled short duration burst sources, and coalescence of compact objects in binary systems. Only the latter is predicted to produce radiation of sufficient amplitude to be detected within a short time with the advanced detectors, but the data is searched for all four.

The stochastic background is a gravitational wave background of cosmological origin, analogous to the Cosmic Microwave Background in electromagnetic radiation. LIGO's searches for the stochastic background attempt to either find or place an upper limit on it by calculating the cross-correlation of the data from the different detectors.

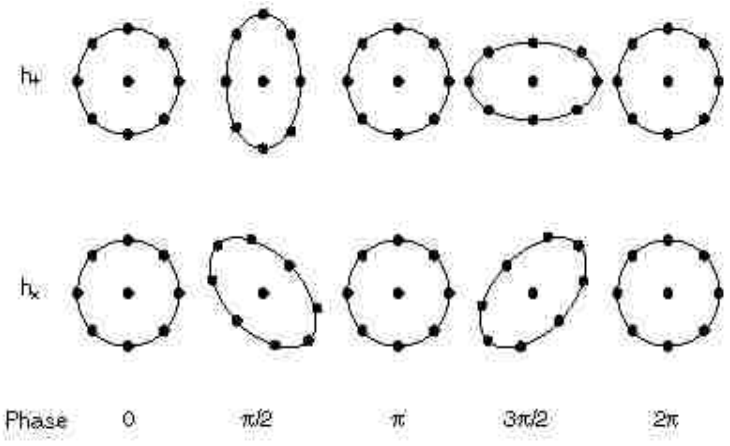

Figure 1.1: An schematic of how the separations of test masses are stretched and compressed by each polarization of gravitational radiation.

The continuous wave sources are thought to be just that, individual sources that persistently emit gravitational radiation at a constant, intrinsic frequency. An example of this type of object would be a rotating neutron star that is not symmetric around the axis of rotation. While over short time intervals, these objects radiate extremely weakly, the advantage of such a search is a linear increase in signal amplitude by integration over an extended period of time, provided frequency modulations due to relative motion of the source and LIGO detectors are properly taken into account.

Unmodeled bursts of gravitational radiation include both predicted sources with unknown or incompletely understood waveforms, as well as completely unknown sources. Searching for a burst is essentially a search for excess power in some frequency range over a short time interval. Possible sources include type II Supernovae, in which massive stars burn out their fuel and collapse under their own gravitation. As the core is compressed by the deepening potential well, the proton and electrons in the material in the center combine into neutrons, and the neutron degeneracy pressure of said material is though to halt the collapse, cause much of the remaining infalling material to bounce off and explode outward. If this explosion is non-axisymmetric, it should produce a burst of gravitational radiation, and the newborn neutron star at the core may provide a continuous wave source. Such events are unlikely to be observed by LIGO outside of our Galaxy, in which the occurrence rate of such events is roughly one per fifty to one hundred years (6). Other types of supernovae, or other systems as of yet unpredicted, are also possible sources for this search.

The coalescence of compact objects (CBCs), such as black holes or neutron stars, in binary orbits is perhaps the most completely understood of the expected types of sources. In 1975 Taylor and Hulse observed a pulsar, dubbed PSR 1913+16, and from modulations of the arrival time of the pulses of radio emission they deduced that the pulsar was in a binary system, with an orbital period of 7.752 hours (7). Over the past thirty years, the period of this system has repeatedly been measured, and the decrease in period has been determined to be, within the (small) observational errors, that predicted for loss of angular momentum to gravitational radiation. By Kepler's law, this necessitates a corresponding decrease in orbital separation and increase in orbital speed. This in turn increases the amount of gravitational radiation emitted, leading to a runaway process of orbital decay. For an idealized case of

two point masses orbiting each other, it can be shown that to leading order the strain

$$h_{\mu\nu} = \frac{2G}{Rc^4}\ddot{I}_{\mu\nu}(\tau), \tag{1.6}$$

where R is the distance from the source to the observer, and $\ddot{I}_{\mu\nu}$ is the second time derivative of the quadrapole moment evaluated at retarded time $\tau = (t - R/c)$. The orbital energy is radiated at a luminosity

$$L_{GW} = \frac{G}{5c^5} < \dddot{I}_{\mu\nu} \dddot{I}^{\mu\nu} > . \tag{1.7}$$

Since we only care about the purely quadrapolar motion we can, using Newton's law, Keppler's law, and equating the orbital energy rate of change to the gravitational wave luminosity, find the rate of change of the period for such a system of

$$\frac{dP}{dt} = -3.4 \times 10^{-12} \left(\frac{M}{M_\odot} \frac{1\text{hour}}{P} \right)^{5/3}, \tag{1.8}$$

where M is the component mass of each object, $M_\odot$ is the mass of the Sun, and P is the period(5). Figure 1.5 illustrates the increase in frequency and amplitude of the expected strain output.

For PSR 1913+16, this works out to roughly $10\mu s$ per year. The waveform of this radiation is well modeled by a 2^{nd} order Post-Newtonian approximation, and is parameterized by the masses of the compact objects (if the objects have significant individual rotation, this must be included in the modelling). While the Taylor-Hulse binary pulsar is still millions of years away from the collision of the compact objects, the ensuing merger into a black hole, and the ring down of this black hole to a Kerr black hole (collectively referred to as the coalescence), it provides evidence of the existence and evolution gravitational radiation from these types of systems.

1.4 LIGO

The Laser Interferometer Gravitational-wave Observatory (LIGO) (8) , funded by the National Science Foundation through the LIGO lab, and administered by MIT and Caltech, was designed and built to detect gravitational waves. The Observatory consists of three interferometers at two widely distant sites in the US; the Hanford, WA site has two interferometers with arm lengths of 4km and 2km (dubbed H1 and H2), and the Livingston, LA site has one 4km arm length interferometer (L1). The "Y" arms of the detectors are co-aligned on a great circle on the surface of the Earth. In order to improve the sensitivity of the LIGO interferometers, the arms are Fabry-Perot cavities, in which the light is resonant. Additional observatories in collaboration with LIGO include GEO (9), a British-German 600m interferometer in Hanover, Germany, and Virgo (10), a French-Italian 3km interferometer just outside Pisa, Italy.

Figure 1.2 shows that a gravitational wave incident on free test masses will contract the separation along one axis perpendicular to the propagation direction, while expanding it along the other axis perpendicular to propagation. Michelson interferometers measure the differential change in length of perpendicular arms, and therefore lend themselves to measuring gravitational waves. In a modern interferometer, light from a laser is sent down the arms by a beam splitter, and at the end of each arm is reflected back. This light interferes

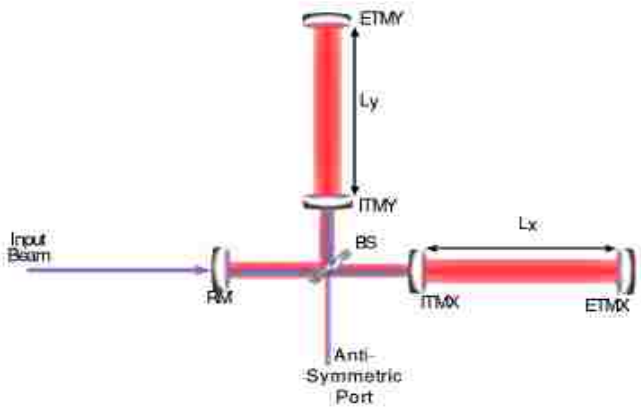

Figure 1.2: Schematic of the LIGO interferometer layout. In addition to the beam-splitter (BS) and end mirrors along the arms labeled X and Y (ETMX and ETMY), LIGO uses two mirrors to make the arms into resonant Fabry-Perot cavities (ITMX and ITMY). Also, a recycling mirror (RM) is used to create a cavity with the two ITMs that resonates on a frequency modulated sideband (blue lines above) of the carrier light (red lines above); the widths of the lines illustrates the power buildup in the resonant cavities. The sideband is measured at the anti-symmetric port, while the carrier light returns to the symmetric port, and is "recycled" into the interferometer by the RM. (11)

upon returning to the beam splitter. This is measured by photodiodes at the antisymmetric port of the interferometer, where changes of relative phase between light from each arm alters the destructive interference, translating arm-length distance into transmitted light.

This relative phase is of order

$$\Delta\Phi = B\frac{\Delta L}{\lambda} = B\frac{hL}{\lambda}, \tag{1.9}$$

Where λ is the wavelength of the light and B is the mean number of passes the light makes in the arm cavities before returning to the beam splitter. The factor B is constrained by the transit time of the gravitational wave; if $BL/c \geq$ half the period of the gravitational wave, $\Delta\Phi$ decreases. This measurement of relative phase is limited by the shot noise of photons arriving at the beam splitter. For Gaussian noise this scales as $\sqrt{N}$, where N is the mean number of photons that will arrive at the beam splitter per unit time. The signal, however, scales as N, so the relative noise scales as $\Delta\Phi \sim 1/\sqrt{N}$.

Taking $L \equiv (L_x + L_y)/2$, as the gravitational wave passes one arm will be shortened, and the other lengthened, and with differential arm length $\Delta L \equiv L_x - L_y$, we expect to observe a *strain*

$$h(t) = \frac{\Delta L}{L} = F_+ h_+(t) + F_\times h_\times(t). \tag{1.10}$$

Coefficients F_+ and $F_\times$ are the "antennae pattern" of sensitivity (8). That is, they depend on the orientation of the interferometer with respect to the impinging wave, and are of order unity[5]. From the above equation, it follows that, for a given precision limit for ΔL, the larger the arm length L, the smaller the strain one can measure.

In LIGO, this differential arm length signal (DARM) is used in a feedback control loop to keep the Fabry Perot cavities resonant, which is known as being "in lock". This is accomplished by four length sensing and control feedback control systems, including DARM (11). The other degrees of freedom that are controlled are the motion in common between the arm lengths (CARM), the differential change in optical path between the ITMs and the recycling mirror (called the simple Michelson, or MICH), and the common change in optical path of the power recycling cavity between the ITMs and the RM (PRC). DARM is controlled by actuating the ETMs, MICH by actuating the BS, PRC by actuating the RM, and CARM by changing the frequency of the main laser itself. In addition to the four length degrees of freedom, the pitch and yaw motions of all of the major optics mentioned earlier must be controlled. There are a variety of systems used to monitor and feedback to the angular controls.

The theoretical sensitivity of LIGO is further constrained by two other major sources of detector noise, pictured in Figure 1.3. Thermal noise internal to, and in the suspensions of, the test masses adds displacement noise, dominating it below 100Hz (above which the shot noise dominates) and above ∼40Hz. Below 40Hz the main noise is from the continuous seismic motion of the Earth. The experts who work on the detectors have made enormous progress on increasing the sensitivity of the LIGO detectors, as evidenced by the Figure 1.4, which shows the progression of the power spectral density from the first Science Run (S1) in 2002 to the design sensitivity run (S5). On the way, a variety of technical noise sources, some broad and some narrow band, some intermittent and some continuous, had to be fixed.

In October 2007, the LIGO detectors completed a fifth data run over a two-year long period, denoted as S5, during which one year of triple-coincidence data was collected at design sensitivity. The LIGO detectors were sensitive to the coalescences of massive compact binaries up to 30 Mpc for neutron stars (12; 13), and even farther for binary black holes. The

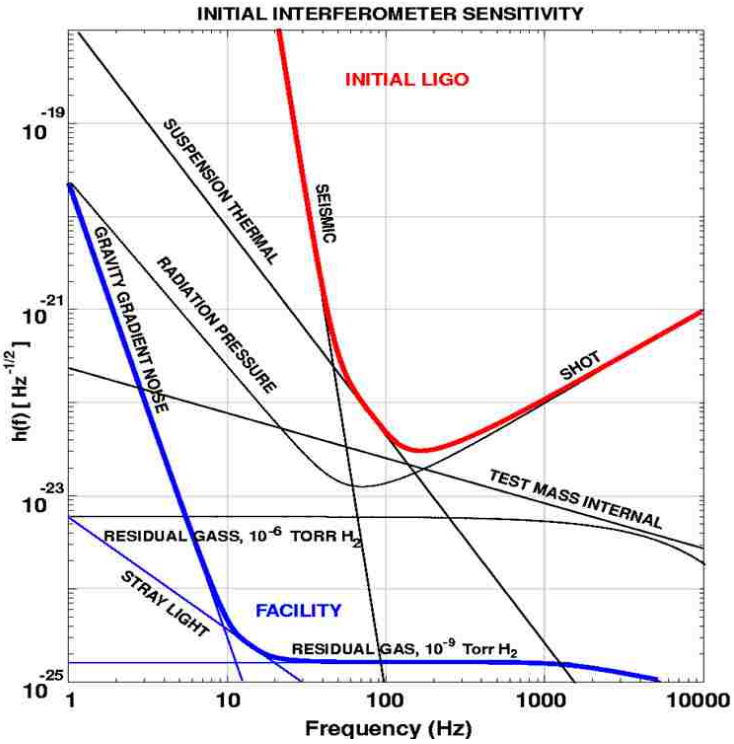

Figure 1.3: Theoretical estimation of noise(1)

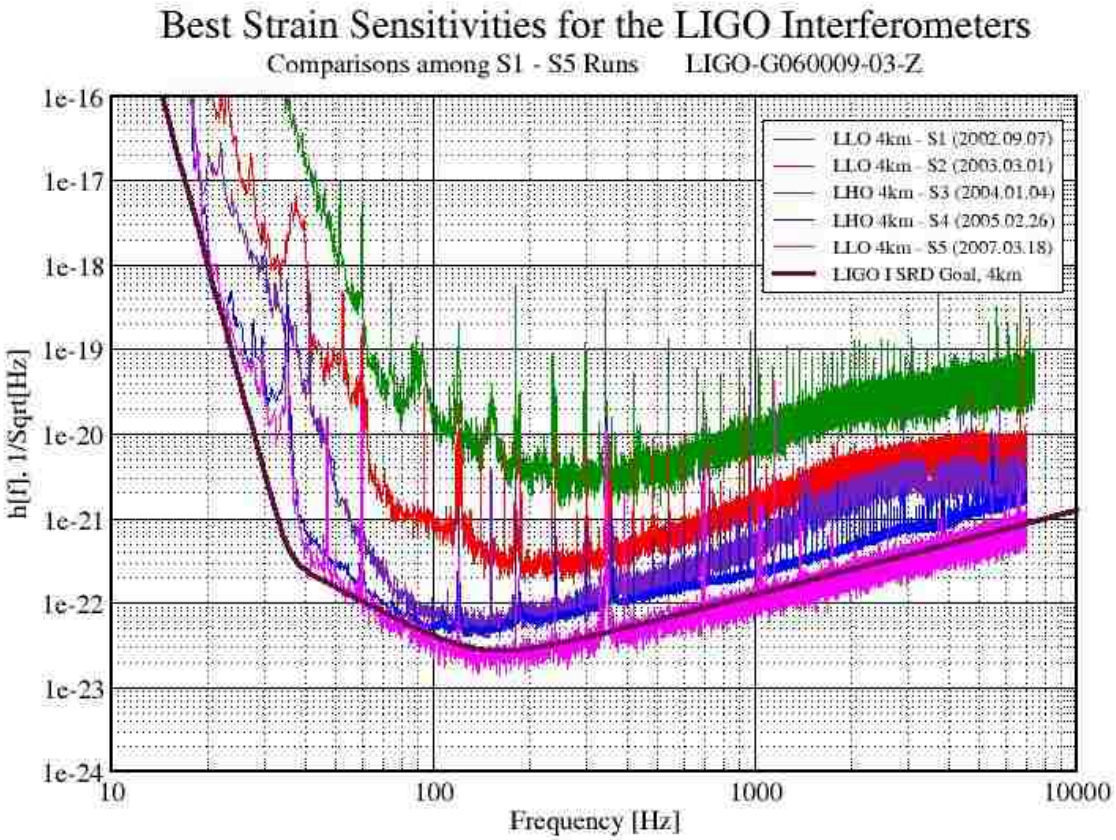

Figure 1.4: The above figure shows the progressive improvement in strain sensitivity from S1 to S5. Now, during S5, LIGO has achieved design sensitivity.

future "Advanced" LIGO upgrades are planned to increase the sensitivity significantly (14; 15).

1.5 The LSC Search for Compact Binary Coalescences

1.5.1 The LIGO Scientific Collaboration

The LIGO Scientific Collaboration (LSC) performs astrophysical searches for gravitational waves from compact binary coalescences (CBCs), including the inspiral, merger, and ringdown of compact binary systems of neutron stars and black holes. These searches use matched filtering with template banks that include a variety of durations and frequency ranges for inspirals or ringdowns. When a LIGO interferometer is locked and operational, data are recorded in what it is called "science mode." In order to confidently make statements on astrophysical upper limits and detections from science mode data, characterization of the LIGO detectors and their data quality is vital. The LIGO detectors are sensitive to a variety of noise transients of non-astrophysical origin, including disturbances within the instrument and environmental noise sources. Triggers so generated constitute a false alarm population of non-astrophysical coincident disturbances above that expected from Gaussian noise, which limit the sensitivity of the searches for gravitational waves.

1.5.2 The CBC Single Interferometer Analysis

Matched filtering is the optimal method of finding known signals in data with stationary Gaussian noise (16). The searches for CBCs in S5 data used a matched filter method to compare theoretically predicted waveforms with the LIGO gravitational wave channel data (17). Because the masses of the components of the binary determine both the duration and the frequency profile of the gravitational radiation, template banks consisting of many different waveforms are used (18). The aforementioned sources of background noise constrain the sensitivity of the detectors to gravitational waves, and hence they constrain the distance from a source at which the interferometers can find a signal significantly above the noise. In order to mitigate these effects, information about the detector state is used to create *veto* time intervals, which are used to remove or re-weight the significance of the output detection candidates.

Matched filtering is the optimal method of detecting known signals in data with stationary Gaussian noise. The reality of the LIGO detectors is that non-stationary and generally non-Gaussian transients in the data are a significant source of noise. These transient noises includes seismic transients, such as earthquakes, ocean waves, trains, and others. Also of importance is acoustic noise, such as from airplanes and the air conditioning at the detector sites. Finally electromagnetic noise can also be a problem, such as from power lines glitches. These transients are described in Chapter 2, and are the focus of veto studies, discussed in Chapter 3. These transient noise sources complicate matters by increasing the frequency of false alarms in the matched filter searches, making it harder to identify true detections.

Defining detector output signal $s(t) = n(t) + h(t)$, where $n(t)$ is the noise and $h(t)$ the short duration signal being searched for, and the waveform template $h'(t)$, the complex output of the matched filter equation is

$$z(t) = 4 \int_{f_{\rm low}}^{f_{\rm final}} \frac{\tilde{s}(f)^* \tilde{h'}(f) e^{2\pi i f t}}{S_n(f)} df, \tag{1.11}$$

where $S_n(f)$ is the power spectral density of the detector output(19). The lower and upper frequency bounds are determined by the noise curve and the final frequency of the coalescence for the template, respectively. We also require a template normalization factor

$$\sigma^2 = 4\mathrm{Re}\int_{f_{\mathrm{low}}}^{f_{\mathrm{final}}} \frac{\tilde{h'}(f) * \tilde{h'}(f)}{S_n(f)} df, \tag{1.12}$$

which allows us to define properly the Signal to Noise Ratio (ρ)

$$\rho = \frac{|z|}{\sigma}\,. \tag{1.13}$$

While sensitive to gravitational radiation, such a search is also likely to detect locally induced transients in the data, as any loud transient will have significant ρ, despite bearing little resemblance to the target waveform. Therefore the LIGO CBC searches employ a number of waveform consistency checks, called signal-based vetoes. One of these is a χ^2 test (21), which works by dividing the waveform $\tilde{h'}(f)$ into p bins, with ρ_i the ρ of each bin, and comparing how well the ρ matches that of the expected waveform for each bin, as follows

$$\chi^2 = p\sum_{i=1}^{p} \left(\rho_i - \rho/p\right)^2. \tag{1.14}$$

When the signal to noise ratio ρ of a template rises above a pre-set threshold ρ_*, and below a threshold in χ^2, a trigger corresponding to the time of coalescence for the binary system is recorded (17). This operation must be repeated for each signal that is being searched for. The CBC searches use banks of templates, each starting from a low frequency cutoff of 40 Hz (defined by the detector sensitivity) and increasing in amplitude and frequency until the coalescence time of the represented system. These templates have durations of up to 44 seconds for the lowest mass templates (binary of 1 solar mass objects).

One additional quantity of note is the "effective distance",

$$D_{eff} = (1Mpc)\frac{\sigma}{\rho}, \tag{1.15}$$

which corresponds to the distance at which a binary directly above the interferometer, and oriented optimally with respect to it, would produce the strain $h(t)$.

1.5.3 The CBC Coincident Analysis Pipeline

A powerful detection advantage of LIGO is the 3000km distance between the two sites. Local sources that introduce transients into the data do so at only one site, but gravitational radiation would affect both sites simultaneously (within the light-travel time between them, $3 \times 10^3\mathrm{km}/(3 \times 10^5\mathrm{km/s}) \sim 10^{-2}\mathrm{s}$). This means that the requirement for coincidence in time between candidates at each site can be an effective veto. In order to exploit this, the CBC search employs a data analysis pipeline, schematically represented in figure 1.6, used in the S3, S4, and S5 searches (19; 20).

Proceeding from top to bottom, the first stage of the pipeline involves matched filtering of data from single IFOs, in parallel. The χ^2 is not computed at this step due to expensive computational cost. The templates that trigger the matched filter above the ρ_* threshold for the search then proceed to the first coincidence stage, where they are analyzed to see if

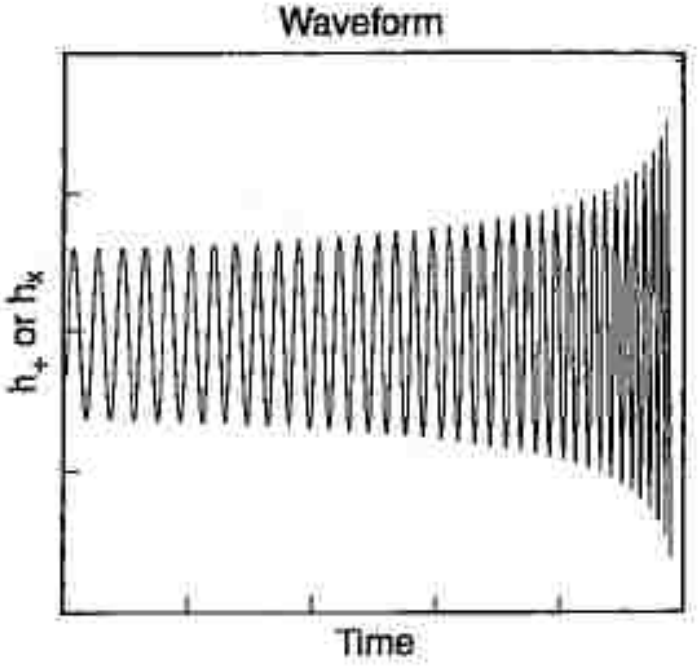

Figure 1.5: Chirp waveform increases in frequency and amplitude over time. The inspiral phase of CBC gravitational radiation waveform is such a chirp, neglecting spin.

they are coincident in time with triggers from the other interferometers, and if so, whether the parameters of the coincident templates match (the component masses of the compact objects in the binary determine the waveform, as per section 2.2). That is, only if the search finds the same waveform at physically consistent times does a coincident trigger become a possible detection candidate.

The second stage of the pipeline again performs the matched filtering of templates against single IFO data, though at this stage only those templates which triggered above threshold in coincidence (though each template is filtered over all of the data, not just those times it triggered earlier). At this stage, the signal-based vetoes are applied, including the χ^2. Again, the surviving templates are analyzed for coincidence. At this stage, the CBC group folds in the extra information about the single interferometer triggers that comes from χ^2 by defining the *effective signal to noise ratio* as,

$$\rho_{\text{eff}}^2 = \frac{\rho^2}{\sqrt{\left(\frac{\chi^2}{2p-2}\right)\left(1+\frac{\rho^2}{250}\right)}}, \tag{1.16}$$

where p is the degrees of freedom of the χ^2, and 250 is an empirically tuned quantity. A further derived quantity called combined ρ_{eff}^2 is simply the sum of the ρ_{eff}^2 values for each single interferometer trigger.

Also at this stage, data quality vetoes are applied to reduce the effect of local transients on both the coincident triggers (the foreground) and the time slide background. In order

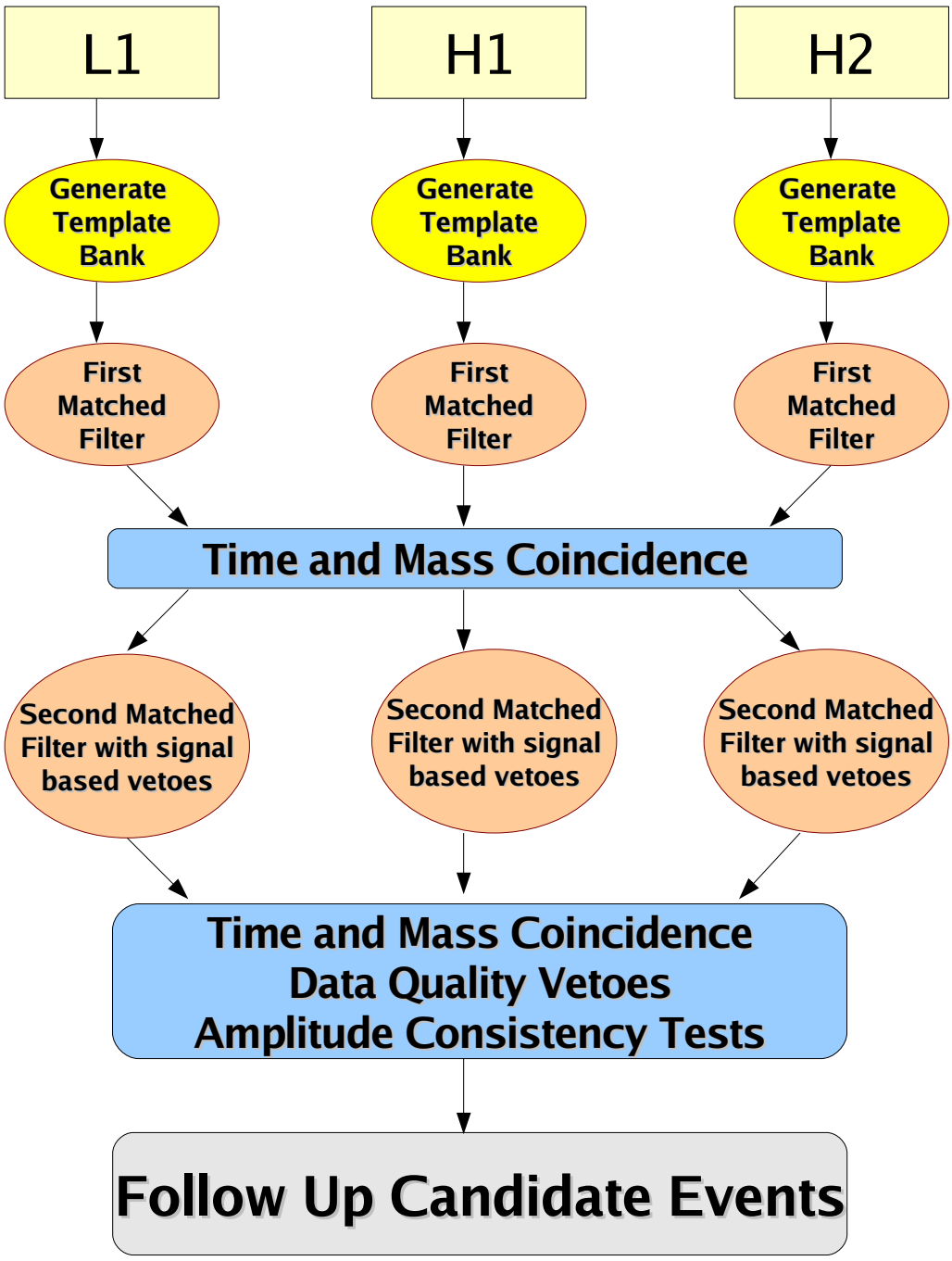

Figure 1.6: Schematic of the analysis pipeline.(19)

to estimate the rate at which the detector noise and local transients induce coincidences, a parallel step is run at this stage in which an offset is added to the time recorded for single interferometer events (different for each interferometer), such that any coincident events found are *known* to be false alarms. The coincidences found in the time slides allow the estimation of the background rate for coincident triggers found in the searches using no time slide (or "zero lag"). The loudest remaining triggers are then compared to the background to look for statistically significant candidate events. These candidates are then followed up exhaustively to ensure that they are not contaminations of the data from local transients, or to determine any astrophysical properties of the detected gravitational waves. To date, there have been no confirmed detections of gravitational waves. Plots of the inverse false alarm rate of the loudest events (all consistent with background) are in Figure 1.7[1].

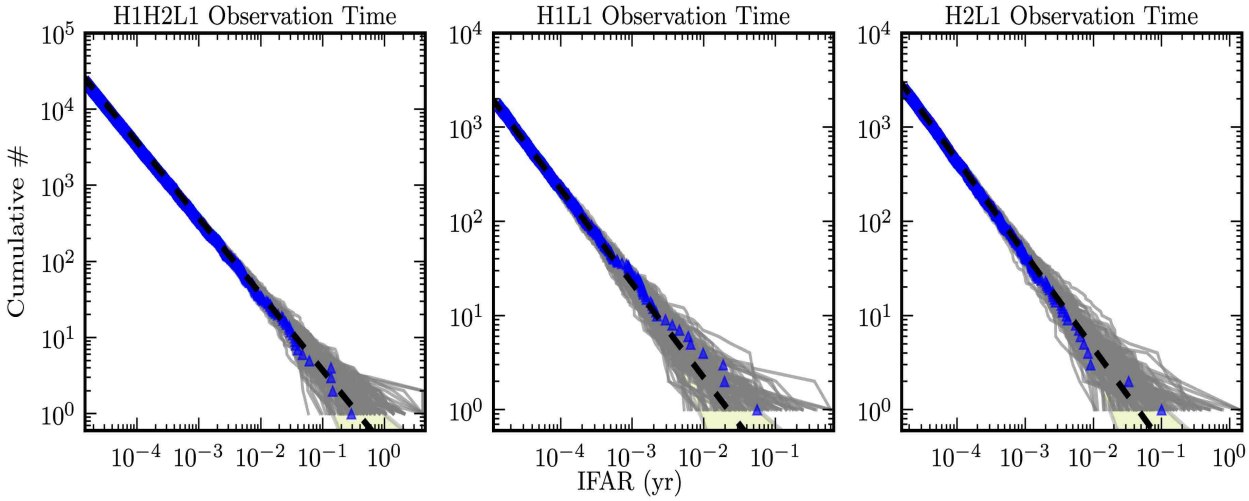

Figure 1.7: Results for the search for CBCs with component masses greater than 1 solar mass and total mass less than 35 solar masses in the first year of S5 data. The cumulative distribution of events above a threshold inverse false alarm rate IFAR, for in-time coincident events, shown as blue triangles, from all coincidence categories for the observation times H1H2L1, H1L1, and H2L1 respectively. The expected background is shown as a dashed black line. The 100 experimental trials that make up our background are also plotted individually as the solid grey lines. The shaded region denotes the errors, calculated as the square-root of number of time-side triggers.

1.5.4 False Alarms and Transients of Non-Astrophysical Origin

We stated that matched filtering was optimal for finding signals in stationary Gaussian noise, but the LIGO detectors contain significant non-astrophysical sources of transient non-Gaussian noises. The details of the data quality will be discussed in Chapter 2. For CBC searches, noise transients in the sensitive frequency range of the detector risk of non-astrophysical origin often produce triggers of large ρ, as there is significant power in these

[1]Figure and caption reproduced consistent with APS copyright policy (12)

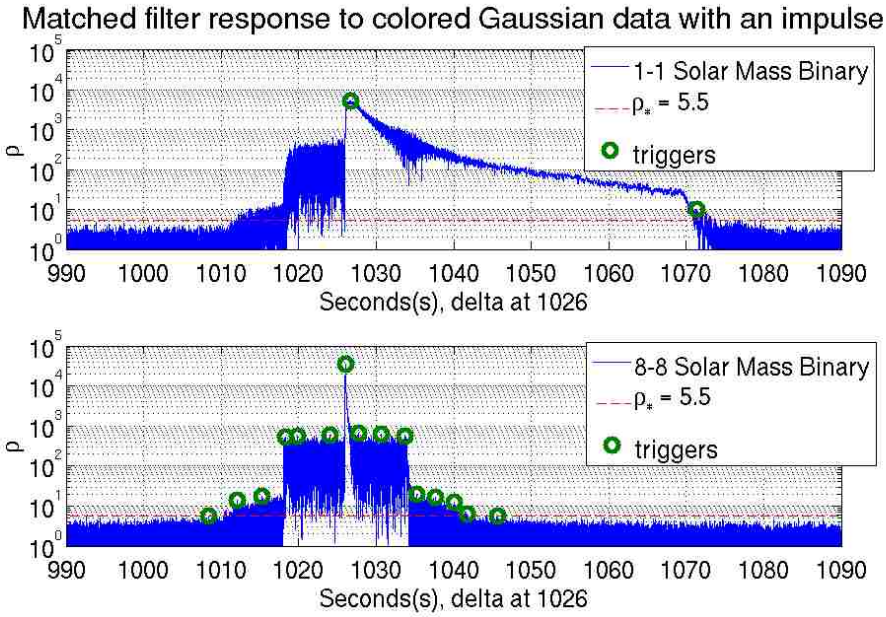

Figure 1.8: Filtering an impulse in Gaussian noise, colored based on the LIGO design sensitivity, using the CBC search with a single template. The result for two templates, top consisting of a binary of 1 solar mass objects, and bottom a binary of 8 solar mass objects. The red dashed line is the search threshold ρ_* of 5.5, and the green circles indicate the positions of the resulting triggers.

transients (19). Even with the signal consistency checks, disturbances of non-astrophysical origin increase the false alarm rate in the time-slides, as well as producing accidental coincidences from non-astrophysical events in the unshifted data. This has the effect of reducing the significance of the loudest events which are not caused by these transients, as the rate of coincidences in the time-slides is increased, and thus the measured false alarm rate of the events in unshifted time is elevated. It therefore has the effect of "burying" good gravitational wave candidates, as coincidences due to transient detector noises can produce significant outliers. In order to reduce these effects, we have learned to define time intervals within which triggers should not be trusted. These are called *vetoes*, and will be discussed at length in Chapter 3.

Figure 1.8 depicts the filtering of an impulse in Gaussian noise, colored to match the LIGO noise spectrum, using the CBC search for a single template. We show the result for two different templates, the top panel consisting of a binary of 1 solar mass objects, and the bottom panel a binary of 8 solar mass objects. The dashed line is the search threshold ρ_* of 5.5, and the circles indicate the positions of the resulting triggers. The response of the matched filter search to loud impulsive transients in the data is complicated, with multiple simultaneous effects of the data and search code. While the ρ time series of both templates have a clear peak near the time of the impulse, the peaks do not perfectly overlap. The lower mass template has a long tail down from the peak, and there is a plateau of high ρ extending 8 seconds before and after the time of the impulse. Additionally, while filtering with both templates results in a trigger with a large ρ value, the higher mass template results in many

more triggers. While many of the triggers shown would fail the χ^2 test mentioned above, any that even marginally pass this test will increase the rate of accidental coincidences in the time-slides, adversely effecting the significance calculation of unshifted coincidences.

The difference in time and ρ of the peak occurs because ρ is recorded at the coalescence time of the matching template, and frequencies in each template are weighted by the frequency dependent noise spectrum of the detector. The time of the maximum ρ value in the top panel, marked by a trigger, is 0.66 seconds after that of the bottom panel, whereas their ρ values are 5000 and 34000, respectively. The effective distance for these two candidates are 0.16 Mpc and 0.13 Mpc, respectively. Notice that although the effective distances are quite similar ρ is nearly 10 times higher for the high mass template, showing that for actual signals, we can detect higher mass signals at greater distances above a fixed threshold in ρ. For a broadband transient, the time between when the transient occurs and when the coalescence time is recorded is determined by the time remaining in the waveform after its frequency content matches the sensitive frequency band of the detector (40 Hz to 1 kHz). No transient is a perfect delta function, and there are many types transients that have different timescales and frequency content.

The ρ tail visible in the top panel of Figure 1.8 occurs due to the aforementioned 44 second template duration. When any part of the template is matched against the impulse, the ρ is significantly above threshold. Rather than record a trigger for all times with $\rho \geq \rho_*$, a trigger is only recorded if there is no larger value of ρ within one template duration of its coalescence time. The higher mass template therefore results in more triggers because its duration is of order 3 seconds, while the plateau is 16 seconds long. The plateau is not caused by any attribute of the waveform, nor by the data adjacent the impulse, but rather is a phenomena intrinsic to the method used to estimate the power spectral density of the data. This occurs in the presence of impulsive transients in the data, as described in sections 4.6 and 4.7 of Ref. (22). Vetoes of impulsive transients for CBC searches must take this into consideration.

In cases of extraordinarily powerful transients, we observe a second trigger slightly more than one template duration from the trigger at the peak of the ρ timeseries, as is the case in the top panel of Figure 1.8. Because the actual search is performed using a bank of thousands of templates of different durations, a significant number of triggers multiple seconds away from the impulse are recorded, as can be observed for the triggers with $\rho \sim 100$ to the right of the peak ρ triggers in Figure 3.1. The veto paddings required to address this are discussed in Chapter 3.3.

1.6 Description of Remaining Chapters

The rest of this dissertation describes the complications that imperfect data quality has on LIGO CBC searches, how they may be overcome, and how the understanding of data quality improved the searches for CBC systems in S5. Chapter 2 details the transients of non-astrophysical origin that degrade LIGO data quality, and the efforts made to characterize them. Chapter 3 describes how this information is used to create vetoes for searches for CBCs in LIGO data. Chapter 4 details how the vetoes for S5 effectively reduce the single interferometer false alarm rate, and in so doing improve the chances of making a detection in the coincident analysis. Chapter 5 describes the 5th Astrowatch run, which took place after S5, and both the overall data quality and how vetoes were created for an opportunistic triggered search. Chapter 6 summarizes results and conclusions.

2. Data Quality in LIGO Detectors

2.1 Introduction

There are two broad categories of spurious transients in LIGO data, produced by instrumental and environmental sources. Within these two classes of noise sources, there are dozens of identified phenomena that require vetoing. LIGO records hundreds of channels of data on the state of controlled degrees of freedom of the interferometers, as well as the output from environmental sensors located within the different buildings of the Observatory.

When a set of transients effect the stability or sensitivity of the gravitational wave data, members of the Detector Characterization and Glitch groups within the LIGO Scientific Collaboration (LSC) work to determine the source of these transients, using the auxiliary channel data (23). When a given noise source is identified, it is documented with sets of time intervals referred to as data quality flags. These data quality flags are discussed in Chapters 2.1.2 and 2.1.3. As an example, the investigation of a significant environmental noise source at Livingston related to nearby trains, and effort that was involved in creating a data quality flag for it, is discussed in detail in Chapter 2.2.

2.1.1 Science Data

When a LIGO interferometer is locked and operational, time intervals are called "science mode." In order to confidently make statements on astrophysical upper limits and detections from science mode data, characterization of the LIGO detectors and their data quality is vital. This work is carried out by the Detector Characterization working group, including the "Glitch" group mentioned earlier, within the LSC, and is detailed in the rest of Chapter 2.1.

2.1.2 Data Quality Flags from Instrumental Noise Sources

Each LIGO interferometer makes an extremely sensitive comparison of the lengths of its arms. This necessitates the ability to sense and control minute changes in displacement and alignment of the suspended optics, as well as intensity and phase in the laser (8), using feedback control systems. The control systems have both digital and analog components, as well as a variety of complex filtering schemes. Instrumental noise transients, or *glitches*, are fluctuations of large amplitude and short duration in the control systems. While these may be prompted at times by environmental effects, they can be identified and vetoed by using the control channels alone, as they are well known error modes of the control systems. We describe some examples in the following paragraphs.

- Overflows in In-Loop Control Signals

  The feedback control signals used to control the interferometer arm lengths and mirror alignments are processed and recorded in digital channels. When the amplitude of such a signal exceeds the maximum amplitude the analog-to-digital and digital-to-analog converters can accommodate, it "overflows", and the signal abruptly flattens to read as this maximum value, until the quantity falls back below this threshold. This discontinuity in the control signal usually introduces transients at the time of the

overflow. As seen in Figure 2.1, these transients are short in duration, but broadband, covering a frequency range across the entire sensitive band of the interferometer.

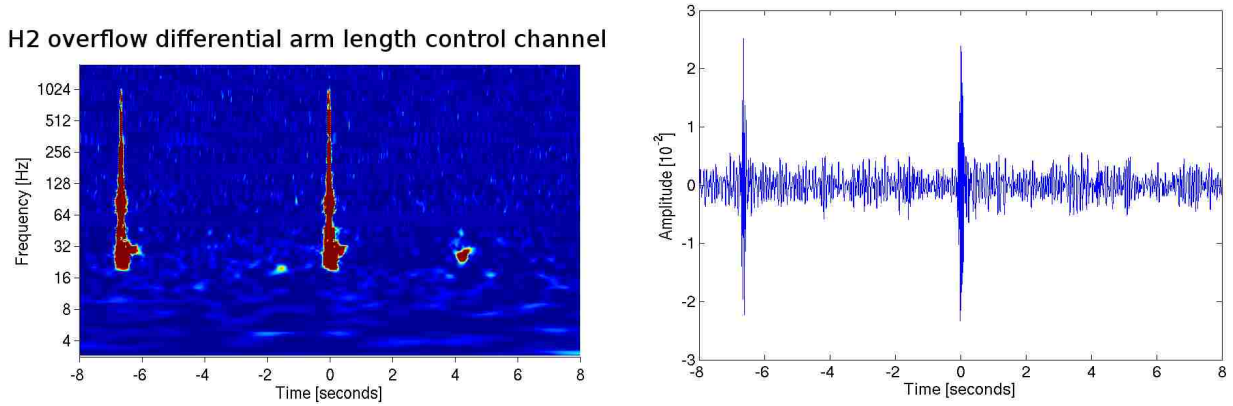

Figure 2.1: Time-frequency representation of H2 gravitational wave channel during control loop overflows. The energy in a given time-frequency bin increases from blue to red. At right, the time series of the same data.

- Alignment Instabilities

  Brief mirror misalignments caused drops in the power in the arm cavities, and thus transients in the data. These light dips are often correlated with the larger amplitude noise transients from known instrumental or environmental couplings. These intervals are labeled according to the percent decline from nominal arm power, with larger percents therefore corresponding to increasingly significant drops.

- Scattered Light between Interferometers

  The two interferometers at the Hanford site share the same vacuum enclosure. During times when one of the interferometers was locked and in science mode, and the other was not locked, the swinging of the uncontrolled mirrors of the unlocked interferometer scattered light into the locked interferometer. This produced strong, short duration transients.

  An example is illustrated in Figure 2.2. At left, a single "swing" that produced a single interferometer trigger in H1 that was found in coincidence with L1, before vetoes. At right, many more such bursts of noise from scattered light during the surrounding seconds.

- Actuation of Differential Arm Motion

  Signals of single frequency are continuously injected into the feedback control system to provide calibration. Occasionally, these signals "drop out" for short periods of time, usually one second. This discontinuous jump in the control signal produces artifacts in the data both when the calibration line drops out and when it resumes. These are plainly visible in Figure 2.3.

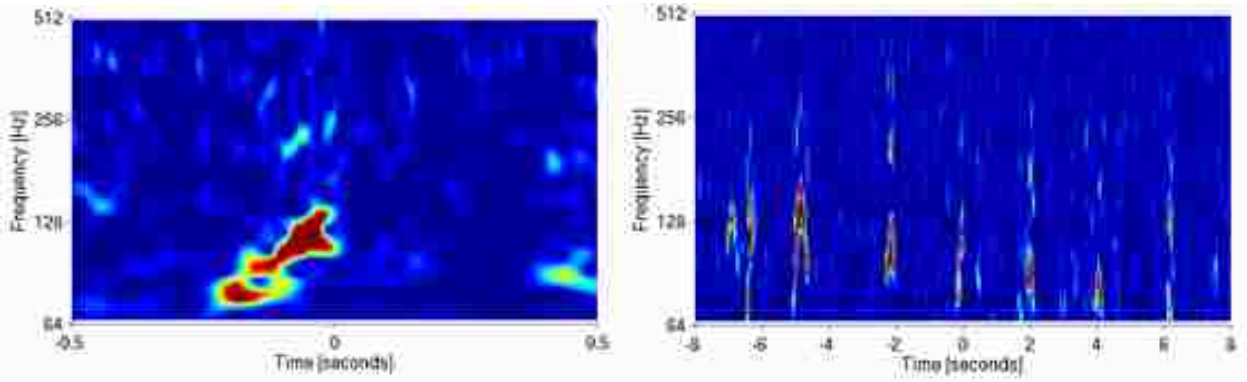

Figure 2.2: Time-frequency representation of H1 gravitational wave channel containing scattered, Doppler shifted light from swinging H2 optics. Both plots are centered around the same transient in the first year of S5, with the right hand plot showing adjacent transients in the science segment. The energy in a given time-frequency bin increases from blue to red.

2.1.3 Data Quality Flags from Environmental Noise Sources

Environmental noise transients correspond to the coupling of mechanical vibrations and electromagnetic glitches that enter into the interferometer. Seismic motion, human activity near the LIGO sites, and weather are the most common sources of mechanical vibrations. Similarly to instrumental transients, we describe some examples that have been identified by the LIGO detector characterization group in the following paragraphs.

- Electromagnetic Noise from Power Systems

  The electronic systems of the interferometers are susceptible to electromagnetic interference, due both to glitches in the power lines and electronics noise at both sites. Magnetometers arrayed around the detector are used to diagnose these signals. Figure 2.4 is a time-frequency representation of one such glitch as it couples into the H2 gravitational wave channel.

- Ground Motion from Seismic Activity and Weather

  Seismic activity from different noise sources have different characteristic frequencies. Earthquakes around the globe introduce transient noise in the frequency range 0.03 Hz to 0.1 Hz. The Hanford site is arid, with little to block the wind from pushing against the buildings housing the interferometers. Times at Hanford with wind speeds above 30 MPH are problematic. Weather and ocean waves also contribute to ground motion in the frequency range 0.1 Hz to 0.35 Hz at both sites, particularly Livingston.

- Ground Motion from Antropogenic Sources

  Nearby human activities such as trucks, logging, and trains, produce disturbances with frequencies greater than 1 Hz, and up to 10 Hz, and can be so extreme that the interferometers often cannot stay locked. Even when they remain locked, significant noise transients frequently occur. As Figure 2.5 shows that these lower frequency effects can couple to higher frequencies, into the sensitive band of the gravitational wave channel.

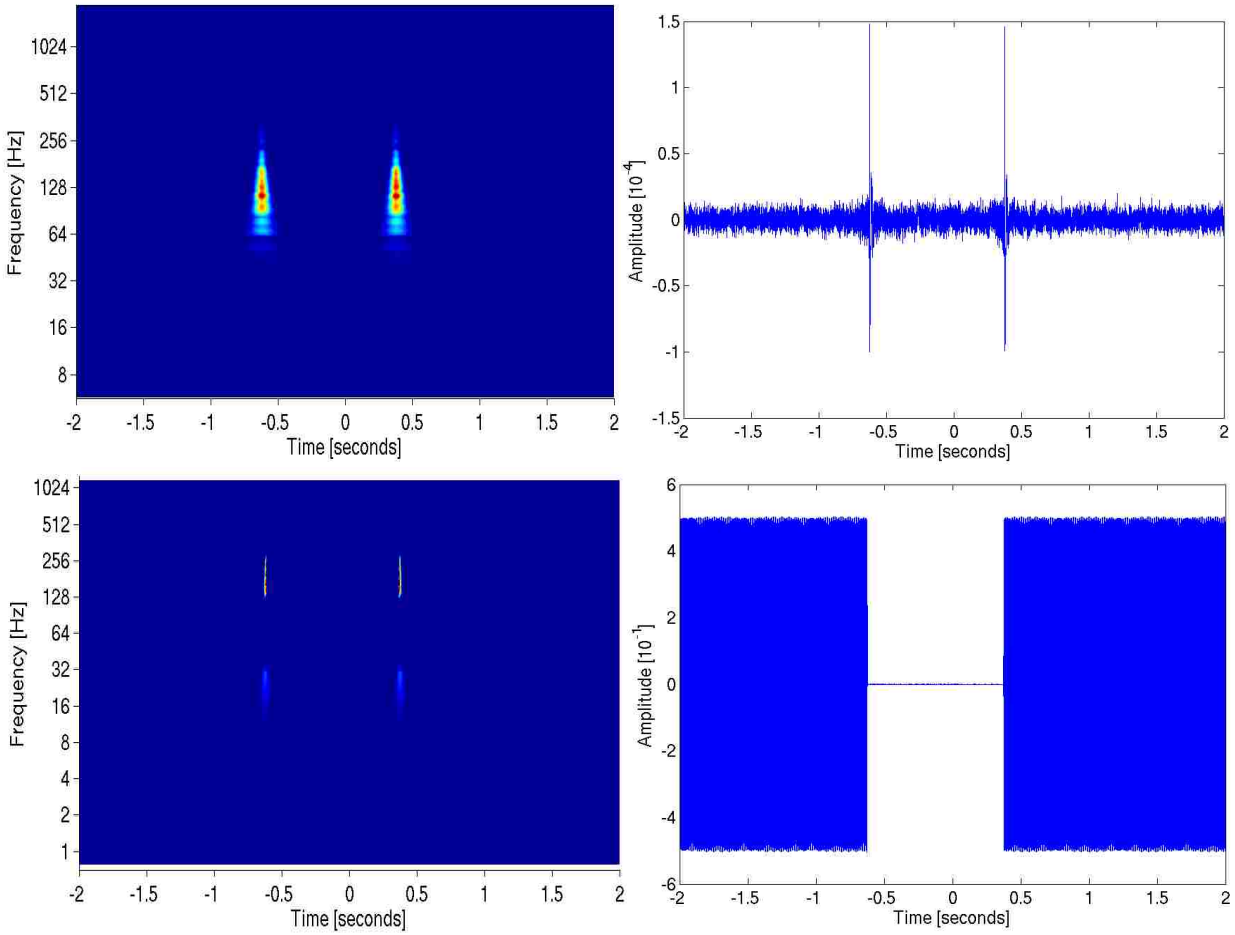

Figure 2.3: Time-frequency representations (left column) and time series plots (right column) for a time when the calibration line injections dropped out for 1 second. Shown are the L1 gravitational wave channel (top row) and differential arm motion excitation channel (bottom row), with two clear impulsive transients in the gravitational wave channel due to the abrupt stopping and restarting of the injection signal. The gravitational wave channel time series plot has been whitened so that the impulses are visible, which the time series plot for the excitation channel has not been filtered. The energy in a given time-frequency bin (for the time-frequency plots) increases from blue to red.

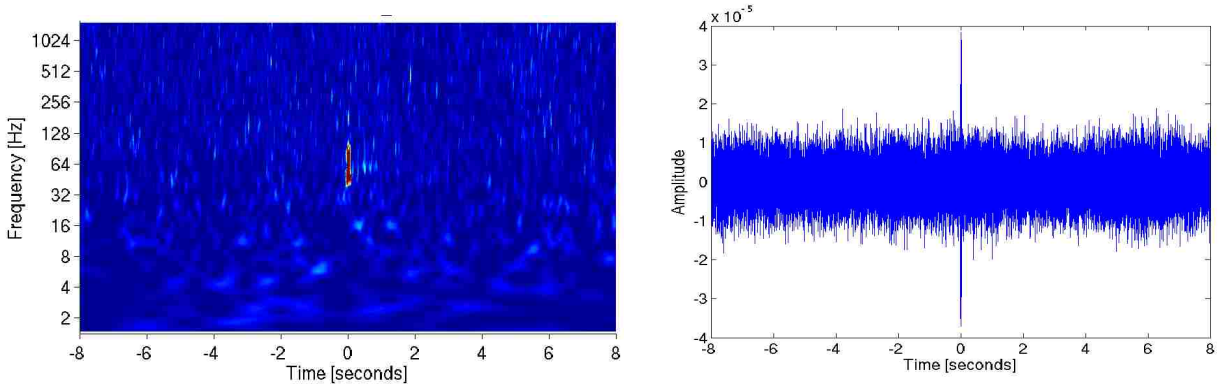

Figure 2.4: At left, a time-frequency representation of H2 gravitational wave channel during electro-magnetic activity. The impulse in the data occurs with short duration near the power-line frequency of 60 Hz. The energy in a given time-frequency bin increases from blue to red. At right, the whitened time series of the same data.

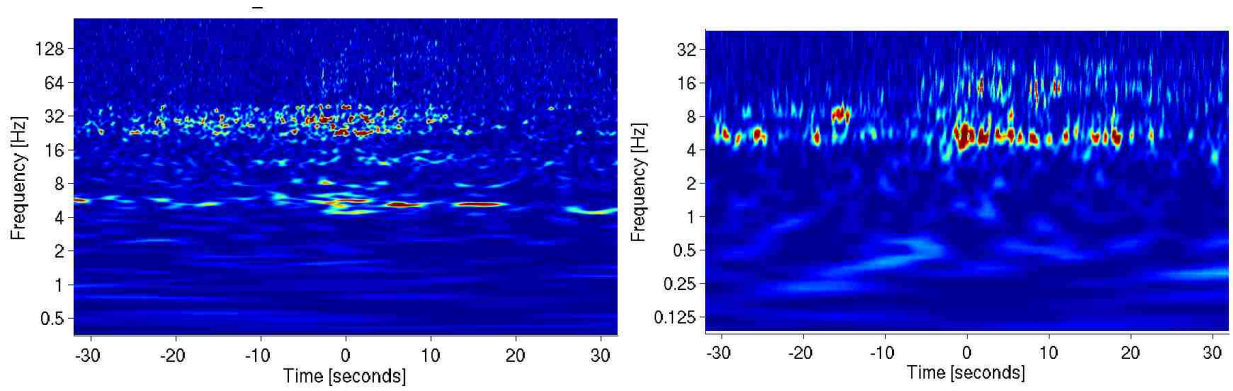

Figure 2.5: At left, a time-frequency representation of H2 low frequency gravitational wave channel during seismic activity. At right, the simultaneous low frequency motion as measured by a seismometer in the corner station. The energy in a given time-frequency bin increases from blue to red.

2.2 Case Study: Seismic Coupling from Freight Trains at LLO

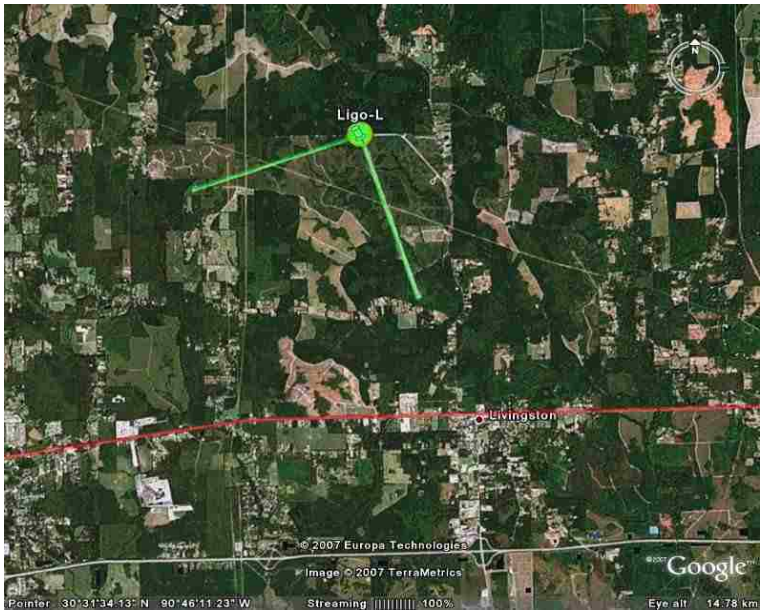

Figure 2.6: LIGO-Livingston IFO highlighted in green, with the train tracks highlighted in red, from Google Earth^{TM}. At the closest approach, the trains pass within 3 km of the Y end station.

Early in S5, investigations illustrated that the frequent trains traveling past L1 not only caused loss of interferometer lock, but were often correlated with transient glitches that loudly triggered the online searches, of both the CBC and burst groups, at times when the interferometers were still in science mode. These trains carried freight on an east-west set of tracks several kilometers south the of closest LIGO building (the Y end station) at irregular intervals, usually several a day. While this was not unexpected, there also seemed to be glitches up to tens of minutes preceding the loudest seismic noise from the trains. It was important to understand if this anecdotal inference could be statistically confirmed. The rest of this Chapter will discuss the characteristics of the ground motion, and investigate correlation with the triggers from the L1 single interferometer CBC search.

2.2.1 Ground Motion due to Trains Passing the Y-End Station

Ground motion caused by nearby anthropogenic activity is carried by surface waves, at frequencies above 1 Hz, and trains in particular produce ground motion in the 1 to 3 Hz band (24). As such frequency bands are sensitive to different sources of ground motion, the band limited root mean square (BLRMS) values are computed for a variety of frequency bands every minute from seismometer channels. The remainder of this chapter focuses on the 1 to 3 Hz band.

There are two main types of surface waves, called Love waves, for which the oscillation is in the plane of the surface and perpendicular to the direction of motion, and Rayleigh

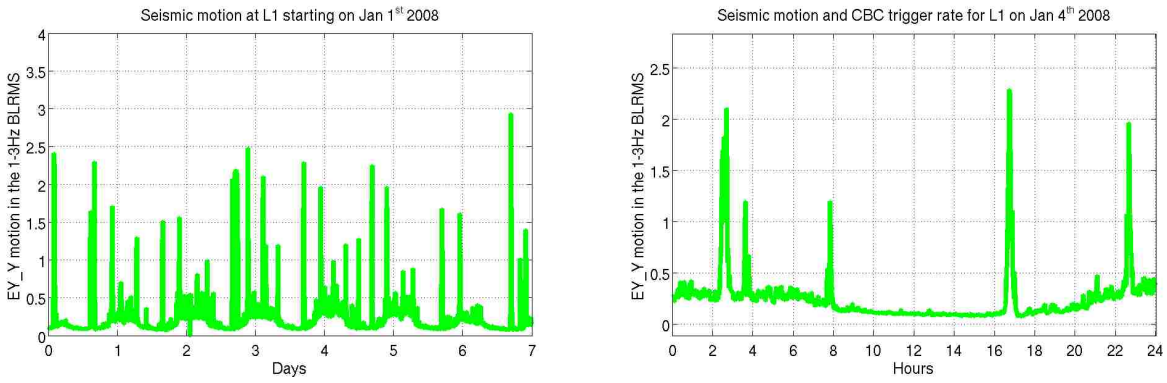

Figure 2.7: Time series of the RMS of the motion in the 1 to 3 Hz band of the ground motion in the direction of the Y arm, measured at the Y end station for each minute. The left plot shows a typical week in S5, and the right plot zooms in on the third day of the left plot. The diurnal variation is readily apparent, as are the spikes the correspond to passing trains. On the second day of the left plot, there is a spike that has longer duration and appears more like a step in seismic level, which is likely caused by a magnitude 6.6 earthquake off Baja California at that time. All other motion above 0.75 μm/s in this week are clearly identifiable as originating with trains.

waves, in which the particles on the surface move in an ellipse with axes along the direction of motion and vertically (25). From measurements taken at the Y end station, it was found that the largest amplitude motion (95th percentile BLRMS minute) was 1.7μm/s in the Y direction (along the line from the train-tracks to the end station), and 1.1μm/s in the Z direction (vertical) and X direction (24).

When a train passes Livingston, the 1 to 3 Hz BLRMS smoothly rises and falls with a well defined peak, as shown in Figure 2.8. They have measurable durations of tens of minutes, and characteristic amplitudes that vary from just less than 1μm/s up to 3μm/s in the RMS minute trends, and more rarely can exceed 4μm/s. The seismic motion from the trains was also apparent in other seismometers, such as at the corner station and at the X end station, but with lower amplitudes. Since the trains' closest approach to the Y station is 2.8 km, 5.5 km to the X end station, and 6.6 km to the corner station, the signal is strongest at the Y end. Specifically, the velocities measured are surface waves, so we expect the amplitudes to vary as $1/r$, where r is the distance between the origin of the waves and the stations. Thus, the amplitude ratios are simply

$$\frac{V^Y_{rms}}{V^X_{rms}} = \frac{r_X}{r_Y} = \frac{5.5km}{2.8km} = 2.0 \tag{2.1}$$

and

$$\frac{V^Y_{rms}}{V^C_{rms}} = \frac{r_C}{r_Y} = \frac{6.6km}{2.8km} = 2.4, \tag{2.2}$$

where V^Y_{rms}, V^X_{rms},and V^C_{rms} are the rms velocities in the 1-3Hz band per minute at the X, Y, and corner station, respectively, and r_Y, r_X, and r_C are the distances of closest approach

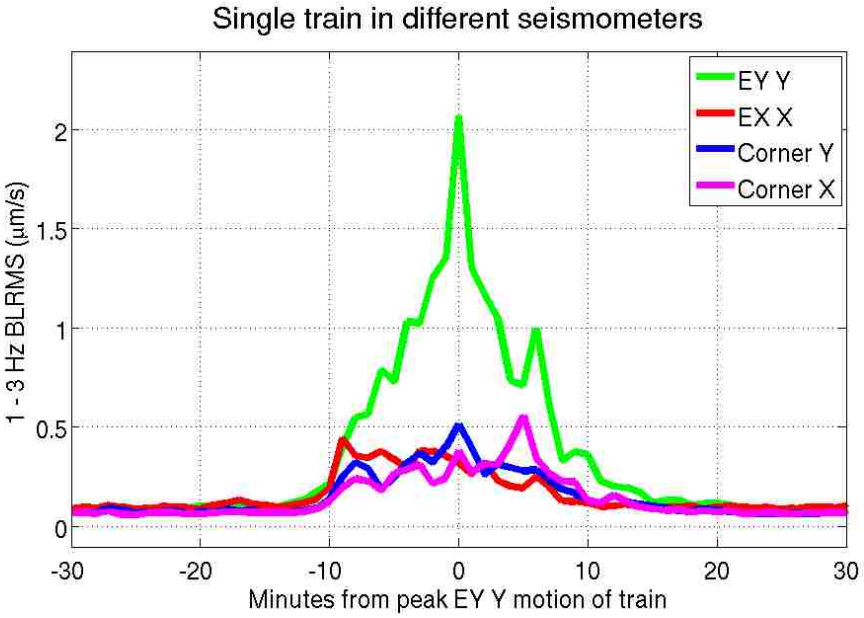

Figure 2.8: Plot of the 1 to 3 Hz BLRMS for a train in January of 2006. Shown is the motion along the Y arm direction for the Y end and the large vacuum enclosure area (LVEA) at the corner station, as well as the X arm direction at the X end and the LVEA.

between the tracks and the X, Y and corner stations. In reality, both ratios are closer to 3, confirming that the Y end station is the most sensitive to passing trains.

Individual trains can be identified automatically by identifying all times above a characteristic threshold in the EY BLRMS, and then clustering these times by the highest motion. This will catch the occasional motion with an alternate source such as nearby earthquakes or logging. Such sources are far rarer than the multiple trains that pass through Livingston daily, and are usually not associated with science data, the logging due to its severity, and the earthquakes due to the broader frequency content and the peaking of the seismic amplitude at the start of a given earthquake.

Figure 2.9 shows the distribution in velocity of the seismic motion in the band. The quiescent level of activity at night and the anthropogenically dominated level during the day can be found from the histogram to be 0.09μm/s and 0.28μm/s, respectively. The smallest trains peak at above 0.6μm/s.

2.2.2 Correlation of CBC False Alarms with Trains

As described in Chapter 1.5.4, the CBC search used matched filtering to search the gravitational wave data with a large bank of templates, and transient noises not of astrophysical origin trigger false alarms in this data. In order to test the above hypothesis that passing trains in Livingston trigger these false alarms, we would like to estimate the rate of false alarms in the search, and see if it increases with the presence of trains.

We calculate the trigger rate by counting the number of raw, unclustered single interferometer triggers in each second of science mode. All science and data quality segments are an integer number of seconds in duration. The second trends so computed have units of

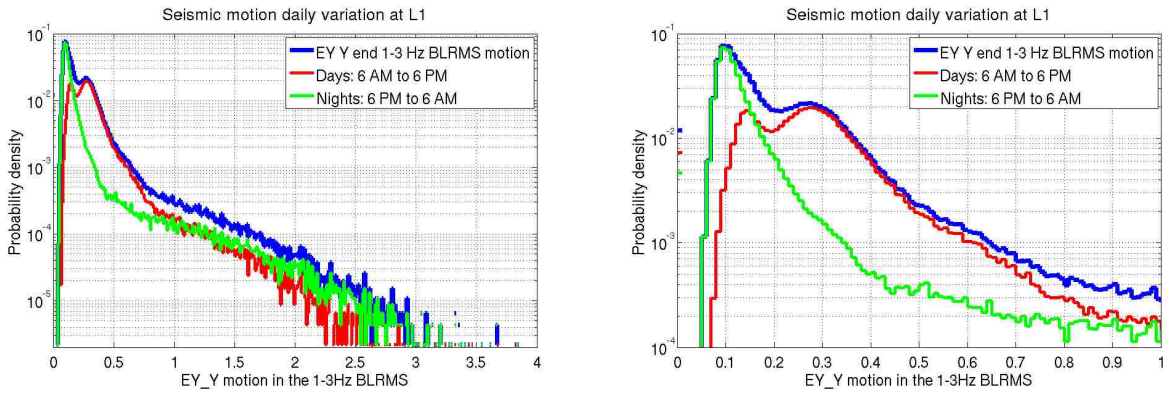

Figure 2.9: Histogram (left) and zoomed histogram (right) of EYY 1-3Hz RMS motion during the day and night at L1. The vast majority of these measurements fall into a bimodal distribution corresponding to the different daytime and nighttime levels of anthropogenic ground motion. The tail to high velocity corresponds to loud transient ground motions, the most common of which were trains. The bulge at lower amplitude for the daytime is due to the lower anthropogenic activity on weekends.

triggers per second, and can be collected into minute trends by counting the total triggers in science mode in 60 sequential seconds, divided by the number of seconds in science mode.

Figure 2.10 shows the same day as in Figure 2.7, but with the addition of the minute trends of the CBC trigger rate. There are a number of drops from science mode at night, one of which (at hour 16) is coincident with the times when a train passed L1, as visible from the seismic motion. While there is a clear elevation in trigger rate during the train when the detector stayed in science mode prior to hour 8, there are other elevations of trigger rate in the day not clearly correlated with seismic motion, including the higher rate minutes after the train at hour 17. In order to move beyond anecdotal evidence, a broader study is required. In particular, to define a data quality flag, it is necessary to decide what duration around the peak seismic motion to flag.

It is therefore useful to compute correlation of the two data streams. A standard approach is to calculate the correlation, as defined by the linear correlation coefficient (26). To do so with two variables X and Y, we compute their covariance as

$$\begin{aligned} s_{X,Y} &= \frac{1}{N}\sum_i^N X_i Y_i - \left(\frac{1}{N}\sum_i^N X_i\right) * \left(\frac{1}{N}\sum_i^N Y_i\right) \\ &= \langle XY\rangle - \langle X\rangle\langle Y\rangle, \end{aligned} \tag{2.3}$$

where N is the number of data points in each variable, and $\langle\ \ \rangle$ denotes the mean. To compute the correlation $r_{X,Y}$, we need to normalize the covariance by the square root of the product of the variances of X and Y, which are calculated as the covariance of X with X, and Y with Y. We then obtain

$$r_{X,Y} = \frac{\langle XY\rangle - \langle X\rangle\langle Y\rangle}{\sqrt{(\langle X^2\rangle - \langle X\rangle^2) * (\langle Y^2\rangle - \langle Y\rangle^2)}}. \tag{2.4}$$

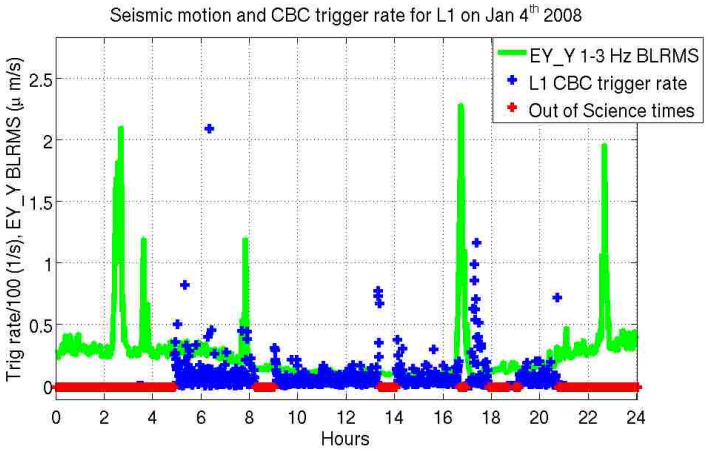

Figure 2.10: The same day as in Figure 2.7, with the addition of minute trends of trigger rate for science times shown in blue, and times not in science labeled in red. The trigger rate has been divided by 100 in order to be able to show it on the same plot as the seismic motion. There is a train at hour 16 that corresponds to a drop from science mode.

The range of r is from -1 to 1, with 1 corresponding to perfect correlation, -1 corresponding to perfect anti-correlation, and 0 indicating uncorrelated inputs. In order to understand the time dependence of the correlation, the correlation can be computed between time-shifted data streams. To illustrate, consider the case of the left plot in Figure 2.11. The trigger rate and seismic plots are shown centered on the peak time of seismic motion from a passing train. Computing the correlation coefficient requires an equal amount of data be input into Equation 2.4. The seismic data in the plot extends three times the duration away from the train peak time as the ± 60 minutes that the trigger rate extends because this data is necessary when computing the correlation of the time-shifted trigger rate. The third plot shows the resulting correlation plotted with time-shift τ from negative 120 to positive 120 minutes. There is evidence of a peak around zero, though there is also significant variation further away from the train.

To get a clearer picture, the average correlation was computed. This was performed by taking the average of the time dependent correlation for all trains identified by clustering minutes above a threshold, as described in Chapter 2.2.1, that had science data for the entire trigger rate sample. With a threshold of 0.8μm/s, there are 93 trains occurring with at least an hour of science data on either side. The average of the computer correlations are plotted on the right in Figure 2.11. Also plotted is the average correlation found between the trigger rate and the train times with an offset of 10 hours. There were 354 intervals that had sufficient science data in this case. The four fold increase in such segments can be attributed to the high seismic motion from trains commonly inducing a drop from science mode due to lock-loss.

While the amplitude of the correlation is not large even in the averaged plot, the correlation found between time shifted trigger rate and the seismic motion is narrowly distributed around zero. Further, the correlation drops off in less than ten minutes on either side of the train. The calculation for the ten hour offset from the train peak times confirms the lack of average correlation away from the peak seismic motion from the trains.

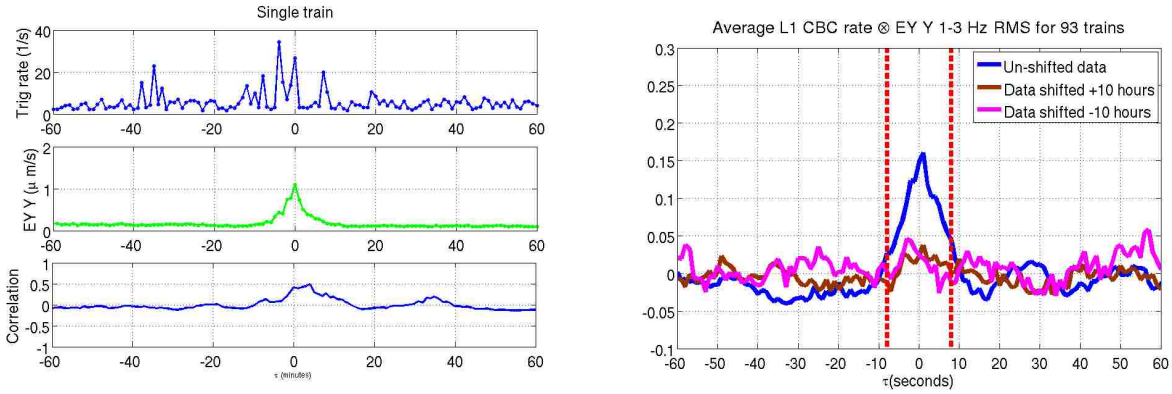

Figure 2.11: At left, three subplots showing the trigger rate (top), seismic motion (middle), and correlation coefficient (bottom) for a single train. The 121 minutes of trigger rate is slid from -90 minutes to +90 minutes against the seismic trace, and the correlation coefficient r computed at each point are shown in the bottom plot. At right, the average of 93 such correlation plots (blue), and the average of 93 non-train times made by sliding the trigger rate time series against seismic traces 10 hours before (magenta) and after (brown) the train. The red dashed vertical lines indicate the ± 8 minutes marked by the data quality flag motivated by this study.

From this result, we defined a data quality interval of ± 8 minutes around the minute containing the peak seismic motion. During the initial design of this data quality flag, a threshold of $\sim 1.4 \mu$m/s was chosen, to correspond to trains of significant amplitude (this corresponded to exactly 10^7 counts of the uncalibrated channel). This was later revised downward to $\sim 0.8 \mu$m/s to catch weaker trains as well, as L1 was more likely to remain in science mode during their passage.

Figure 2.12 shows the attributes of the time marked by the resulting data quality flag. From the green points on the scatter plot, we can see that the trigger rates for the times during which trains pass by are not higher than the highest trigger rates when seismic motion is less pronounced. The minimum trigger rate during elevated seismic activity, however, is generally at least an order of magnitude higher than the minimum trigger rate in generic times. The times surrounding the peak train times do not contain all the minutes above some threshold in seismic motion, but do concentrate at or above a trigger rate of 1 trigger per second. Since density is hard to discern from a scatter plot, the right-hand plot in Figure 2.12 is a histogram of the trigger rate. We see that the median trigger rates are at least 50% higher for times at or near the peak of a train than for all times. This data quality flag, defined by the correlation of elevated seismic noise with elevated CBC raw single interferometer trigger rates can now be evaluated for use as a veto in the searches for gravitational waves. This process of evaluation is described in Chapter 3.

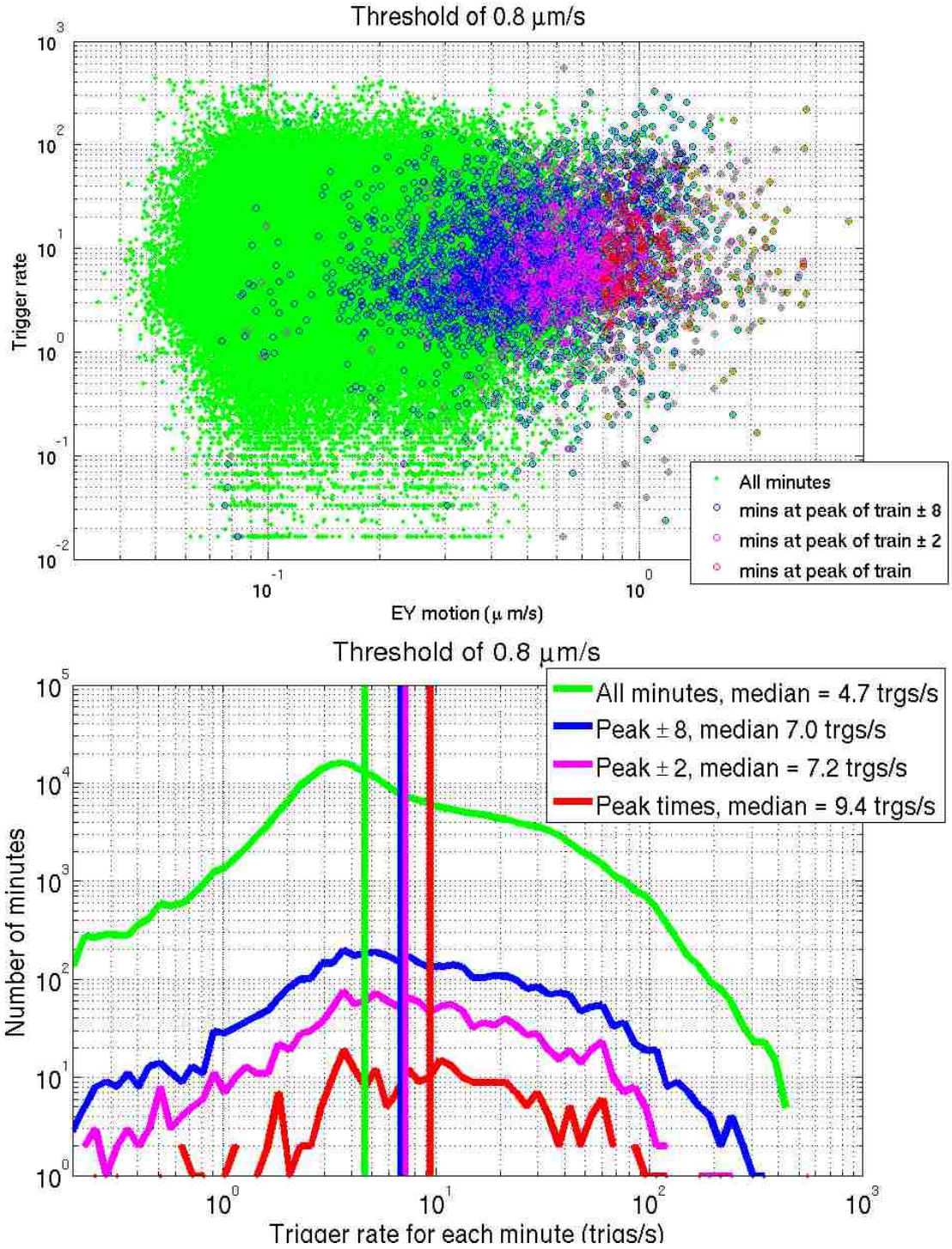

Figure 2.12: At top, a scatter plot of seismic motion versus trigger rate for minutes in the first year of S5. At bottom, a histogram of trigger rates for all minutes, and histograms of triggers vetoed by the train data quality flag, with a vertical line denoting the median of each distribution. For both plots, all minutes are in green, minutes identified as the peak of a train are shown in red, minutes within two minutes of the peak of a train are in magenta, and minutes within eight minutes of the peak of a train are in blue.

3. Vetoes for Searches of Coalescing Binary Star Systems[1]

3.1 Introduction

The LIGO Scientic Collaboration (LSC) search for gravitational waves from compact binary coalescences (CBCs), as described in Chapter 1.5, use matched filtering of banks of template waveforms against the detector output to find candidate signals. These searches also produce false alarms due to noise transients of non-astrophysical origin in the detectors. In this section we discuss techniques for using the detector characterization work described in Chapter 2 to create vetoes for matched filter CBC searches. We illustrate our methods with examples from CBC searches in the first year of LIGO's fifth science run, on which they were developed and implemented (12; 13). The veto techniques discussed in this section are implemented by creating lists of times during which triggers from a search are suspected of originating not from gravitational radiation, but from instrumental or environmental disturbances. When deciding to use sets of time intervals as vetoes, the goal is to include as much of the bad times of the interferometers, and as little of the surrounding science mode, as possible. Since not all artifacts are well understood, we need to create figures of merit, or metrics, to evaluate the effectiveness of the vetoes. These metrics are derived in Chapter 3.2. The padding of data quality flags to become vetoes, motivated in Chapter 1.5.4, is explained in Chapter 3.3. These veto intervals are derived from data quality flags, as detailed in Chapter 3.4. Rather than apply all data quality vetoes together, these vetoes are categorized by physical understanding and statistical effectiveness, and these veto categories are applied successively. This categorization is described in Chapter 3.5, and the effect of veto categories on the sensitivity of the CBC search to gravitational waves is discussed in Chapter 3.6.

3.2 Veto Metrics

There are several quantitative measures of the effectiveness of data quality intervals as vetoes for CBC searches, which are referred to as *veto metrics*. Veto metrics were developed on single-interferometer triggers, from CBC searches in the first year of LIGO's S5 science run, as well as previous runs. For this purpose, the triggers were clustered by keeping a trigger only when there are no triggers with larger value of ρ within 10 seconds. With this clustering, triggers from a single loud transient occurred in one or two clusters, as seen in Figure 1.8. This had the effect of making the figures of merit independent of the number of waveforms in the template bank of the search. A minimum ρ of 8 for the clustered triggers was chosen in order to be sensitive to glitches that produce loud triggers from the template bank. This threshold applies to the clusters used to measure the metrics, but the resulting vetoes are applied to all triggers falling in vetoed times.

The percentage of triggers vetoed defines the *efficiency* of the veto $E = \frac{N_{vt}}{N_t} \cdot 100\%$, where N_{vt} is the number of clustered triggers vetoed and N_t is the total number of clustered triggers. If all outliers came from a single source, then the ideal veto would have 100% efficiency. In

[1]Reprinted by permission of the Classical and Quantum Gravity (31).

reality, there are many different sources of transient noise, as detailed in Chapter 2, and each may be responsible for only a few percent of the clustered triggers, and only in some specific range of ρ values. The efficiency quantifies the effectiveness of the veto for removing clusters, but more information is required to determine whether this removal is warranted. Because the clustering is by loudest ρ, veto efficiency as a function of ρ can be used to learn more about what population of clusters correspond to the transient event being vetoed.

To determine the statistical significance of the efficiency, we need to compare it with the *deadtime*. The percentage of science mode contained in a set of veto intervals defines the deadtime $D = \frac{T_v}{T} \cdot 100\%$, where T_v is the time vetoed and T is the total science mode time, including the vetoed time. If the veto only includes truly bad times, then by vetoing triggers within these times we are not reducing our chance of detection, as the noise transients already polluted this data. In practice, the integer second duration of data quality flags, as well as the need for padded veto windows due to the nature of the CBC search (described in Chapter 3.3), limits how small the deadtime can be for veto intervals that remove common transient noises. It also adds to the probability that a true gravitational wave event, occurring when the detectors are in science mode, will be missed if these times are vetoed. This reduction is a small part of a small detection probability, while the probability of a false alarm being present as measured by the efficiency is significantly larger. Most vetoes have deadtimes of at least several tenths of a percent of the science mode time, although less understood or longer duration disturbances may lead to vetoes with larger deadtime percentages.

Important to the determination of what vetoes are effective is the ratio of the efficiency over the deadtime. Effective vetoes have a deadtime small compared to the efficiency, indicating that many more clusters are vetoed than one would expect by random chance. This ratio is unity for ineffective flags proposed as vetoes, and large for effective vetoes, and can be expressed as

$$R_{ED} = \frac{E}{D} = \frac{N_{vt} \cdot T}{N_t \cdot T_v}. \tag{3.1}$$

The percentage of veto intervals that contain at least one clustered trigger defines the *used percentage* such that $U = \frac{N_{wt}}{N_w} \cdot 100\%$ where N_{wt} is the number of veto windows that contain at least one cluster and N_w is the total number of windows. For an ideal veto, every vetoed interval should contain at least one cluster, corresponding to one or more loud transient noises. For vetoes with short time spans compared to the clustering time, it is more common to obtain values of the used percentage of less than 100%, even for effective vetoes. The statistical significance of this metric is made by comparing the used percentage for a veto to that expected if its intervals are uncorrelated with the triggers. This expected used percentage is obtained by multiplying the length of a given veto interval T_w by the average trigger rate, given by dividing the number of triggers by the available science mode time. The ratio behaves similarly to R_{ED}, and can be expressed as

$$R_U = \frac{U}{T_w \frac{N_t}{T} \cdot 100\%} = \frac{N_{wt} \cdot T}{N_w \cdot T_w \cdot N_t} = \frac{N_{wt} \cdot T}{N_t \cdot T_v}, \tag{3.2}$$

assuming that the data quality intervals are all the same duration $T_v = T_w \cdot N_w$. In the S5 run, there was a clustered trigger on average every 6 to 17 minutes, depending on interferometer. Effective vetoes have an expected used percentage small compared to the actual used percentage, indicating more intervals contain clusters than one would expect by random chance.

The *safety* of the veto intervals must also be ensured. A veto is unsafe if it could be triggered by a true gravitational wave. In order to insure that our instrumental vetoes are

safe, we investigate their correlation with the *hardware injections* mentioned in Chapter 4.3. To evaluate the safety of each veto, the percentage of hardware injections that are vetoed is compared to the veto deadtime. If veto intervals are correlated with the hardware injections, as indicated by a R_{ED} for injections significantly greater than 1, the veto could be generated by an actual gravitational wave signal. Such a veto is therefore "unsafe" and is not used. In S5, no data quality flags were found to be unsafe.

3.3 Veto Interval Padding

For the reasons discussed in Chapter 1.5.4, intervals containing transients not of astrophysical origin often must be padded with extra duration to make them into effective vetoes for the CBC searches. This is done by examining the falloff of the triggers in ρ before and after the transients in vetoed times, in order to include those triggers associated with the transient while working to minimize the deadtime by not padding more than necessary. For the S5 searches, this was determined by examining plots of the maximum and median amplitude transients, as measured by the peak trigger ρ. Figure 3.1 illustrates an example of this process.

Prior to S5, all CBC searches used a single set of veto definitions (27; 28; 29). During S5, CBC searches extended over a broad range of component masses. The wide distribution in the template durations of the waveforms caused the triggers associated with transients in the data to appear at different times, and be sensitive to different frequency ranges. Thus veto window paddings must be defined based on template waveforms included in each search, which are determined by the possible component masses of the binaries.

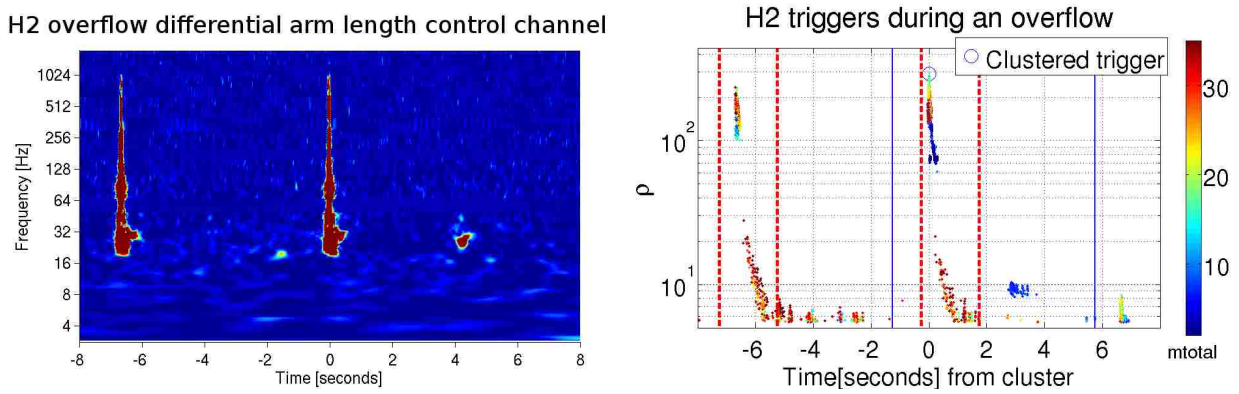

Figure 3.1: A pair of overflows in the length sensing and control system of H2. At left, a time-frequency representation (27). At right, the effect of the transient on the production of unclustered triggers for the CBC search with total mass between 2 and 35 solar masses (dots), the 10 second clusters of these raw triggers (circle), the original Data Quality flags (dashed lines), and the expanded data quality veto after duration paddings are applied (solid lines).

3.4 Data Quality Flags as Vetoes

We apply our veto metrics and window paddings to data quality flags created by the Detector Characterization and Glitch groups within the LSC, as mentioned in Chapter 2. While for some data quality flags, such as the train flag I discussed creating in Chapter 2.2, such investigations were part of the definition process, most flags only indicated times when the issues present might effect the searches. This left the determination of relevance, and the decision to use a flag as a veto, to the search groups.

A concrete example of a veto based on a data quality flag marking instrumental transients can be seen by examining the case of identified intervals containing an overflow in the length sensing and control loops for the H2 interferometer. These overflows cause severe glitches, and are identified within a second of their occurrence. The overflows themselves are caused by other disturbances to the control systems such as seismic motion, but irrespective of the physical origin, the overflow itself produces glitches in the gravitational wave channel. Figure 3.1 shows a time-frequency representation (27) of the gravitational wave channel, as well as a plot of the unclustered triggers as a function of time, for the CBC search with total mass between 2 and 35 solar masses, around two typical transients caused by a type of overflow. The data quality flag intervals start and stop on GPS seconds, and have a minimum duration of two seconds, centered around the times of the overflows, to ensure the glitches are not too close to the edges of the intervals. The loudest raw triggers occur near the transients, corresponding to the clustered trigger. Raw triggers subsequently fall off in ρ over the next several seconds after the data quality interval.

As shown in Figure 3.2, this flag has a used percentage of 62% for a typical month during the first year of S5, indicating that these veto segments are well suited to vetoing triggers from transients. These data quality veto segments have efficiency on all triggers of 1.4%, and deadtime of 0.0037%. The ratio of the efficiency to the deadtime is more than 300. This indicates a veto with a very high correlation to the triggers, as the expectation for random chance would be a ratio of 1. The efficiency is strongly dependent on the ρ of the clustered triggers; for clusters with $\rho \geq 50$ it is 14%, while for clusters with $\rho \geq 1000$, the efficiency is 64%. This indicates that the overflows cause false alarms with high ρ. Two-thirds of the loudest triggers found from the H2 interferometer in this month were due to overflows.

To attempt to account for as many triggers as possible associated with this transient, the veto interval is given 1 second of padding prior to the data quality interval, and 4 seconds after. This alters the metrics, leading to a deadtime of 0.013%, an efficiency for all clusters of 1.7 %, a used percentage of 78 %, and an efficiency to deadtime ratio of 130. The expected used percentage from the trigger rate was only 0.58 %, giving R_U of slightly over 130. For veto intervals with duration equal or less than the clustering time, only one cluster can be vetoed per interval, thus the number of veto windows used N_{wt} approaches the number of triggers vetoed N_{vt}. Comparing Eqns 3.1 and 3.2, this means we expect $R_{ED} \approx R_U$, as we see in this example with a value of 130.

For such loud transients, we expect all veto intervals to be used, but even for the loudest intervals we have tens of percent of the intervals that contain no cluster, as is the case with the aforementioned overflow flags. Of the 22% of the overflow veto intervals that are unused, 20 % are within a clustering time of a clustered trigger. These intervals, therefore, may well have many raw triggers with significant ρ, but these were within the 10 seconds of a louder raw trigger from an adjacent overflow that was marked by a clustered trigger. This is illustrated by the overflow at -6 seconds in the right hand plot in Figure 3.1, which does not have a clustered trigger associated with it, despite hundreds of raw triggers with $\rho \geq 100$, because of the raw trigger 6 seconds later with higher amplitude. In CBC searches performed after the first year low-mass search, the problem is significantly mitigated by employing a clustering window of 4 seconds rather than 10 seconds. The efficiency versus

ρ of the veto interval is shown in Figure 3.2. This rises rapidly with the minimum ρ of the clustered triggers, and the efficiency to deadtime ratio reaches 1300 for clusters with ρ above 50 and over 5000 for clusters with ρ above 500. Efficiency and used percentage would be independent of ρ if the times vetoed were random and uncorrelated with transient noises.

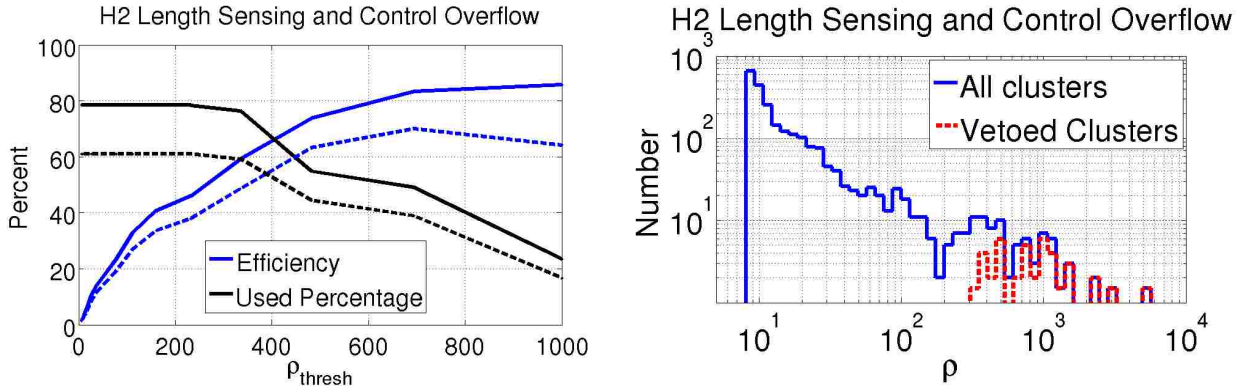

Figure 3.2: The left plot shows the efficiency and used percentage as a function of a minimum threshold single-interferometer cluster ρ for the H2 Length Sensing and Control Overflow veto. The dashed lines are the values for the data quality flag before window paddings are added. The solid lines are the values after windows are added to veto the associated triggers. The right plot shows a log-log histogram for the same veto. All clusters found in science mode are shown in solid lines and vetoed clusters are shown in dashed lines.

The example from Chapter 2.2 of a data quality flag for an environmental transient that we used to make a veto was the flag marking the times of elevated seismic motion due to trains passing through Livingston. Early in S5, investigations of loud noise transients in L1 indicated that many such transients occurred in the minutes preceding loss of interferometer lock due to the passage of trains near the detector. At each LIGO site, seismometers are located in each major building. Since the trains pass closest to the end of the "Y" arm, the seismometer located there is most sensitive to the trains. Specifically, the train-induced seismic motion was most pronounced along the direction of the arm in the 1-3 Hz frequency band. Seismic disturbances due to trains were visible upon examining the 1-3 Hz band limited root mean square (BLRMS) value for minutes of the aforementioned seismometer channel. Setting a minimum seismic threshold in that channel of $0.75 \mu m/s$ in the 1-3 Hz BLRMS to identify times of passing trains, the two to three trains per day that passed the interferometer were identified. Studies of the seismic motion induced by these trains compared with single interferometer online glitch monitoring codes (23) showed correlation for up to a minute before and after the minute of peak seismic amplitude for each train. Data quality flag vetoes were defined to mark these times.

For this example, our metrics then yielded a deadtime of 0.69 %, an efficiency of 2 % for all clusters and 20 % for clusters with $\rho_{thresh} \geq 100$, and used percentage of 60 % and 32 % for each threshold respectively. R_{ED} therefore increases from 3 to 30 with increasing ρ_{thresh}. R_U for the same values of ρ_{thresh} increases from 0.78 to 16. This veto is effective at eliminating a population of significant glitches, though not as loud or common as those from the overflows mentioned earlier. Techniques for combining together the information from these data quality vetoes is discussed in Chapter 3.6.

3.5 Veto Categorization

The goal of using vetoes is to reduce the false alarm rate, in order to more accurately assess whether gravitational wave candidates are true detections. Upon evaluating the available vetoes, we found that they do not all perform similarly, and divided them into categories. Well understood vetoes have a low probability of accidentally vetoing gravitational waves, and significantly reduce the background. More poorly understood vetoes can also reduce the background significantly, but with an increased chance of falsely dismissing actual gravitational waves. We classified the vetoes into categories in order to allow searches to choose between using only the well established vetoes or aggressively using more poorly understood vetoes.

Those vetoes classified as well understood almost always had higher R_{ED} and R_U, as well as lower overall deadtime, than the less understood transients that correspondingly had less effective, longer intervals with poorer ratios. This was because when the mechanism behind a transient was well understood, such as an overflow in the digital control channels of the interferometer, it was easier to identify the specific times at which these transients occurred. In some cases, however, well understood vetoes may include little enough time that statistics are difficult to perform due to the small number involved, and these can still be categorized as well understood, providing sufficient evidence for coupling is present. Conversely, when only the general cause was known, as in the case of transients related to passing trains at the Livingston site, long intervals of time when these conditions were present needed to be vetoed in order to capture the related transients, despite the short duration of each particular transient. In this latter case, a statistical argument based on the veto metrics was required to prove the utility of a set of veto intervals.

The idea of this categorization scheme was to allow the followup of candidate triggers after applying sequentially each category of vetoes with the consequently lowered background false alarm rate, in order to search for detections (12; 13). In the CBC searches in LIGO's S5 science run, we decided on four categories in descending order of understanding of the problems involved:

3.5.1 Category 1 Vetoes

The first category includes vetoed times when the detectors were not taking data in the design configuration. A fundamental list of science mode times is compiled for each interferometer, and only the data in these times is analyzed. These times are logged automatically by the detectors with high reliability, though on rare occasions DQ flags marking non-science mode data mistakenly marked as science quality need to be generated after the fact. These are the same for all searches, and do not need to be padded with extra windows, as the data are not analyzed.

3.5.2 Category 2 Vetoes

The second category contains well understood vetoes with well tuned time intervals, low deadtimes and a firm model for the coupling into the gravitational wave channel. For many transients, this results in a high efficiency, particularly at high ρ, though this is not necessarily the determining factor in categorization. A well understood noise coupling into the gravitational wave channel may consistently produce triggers of moderate amplitude, or at a lower rate than more common transients. These are still considered to be of category 2 if several conditions are met. The ratios R_{ED} and R_U should be statistically significant, of order 10 or higher, for all clusters above some ρ threshold characteristic of the transients.

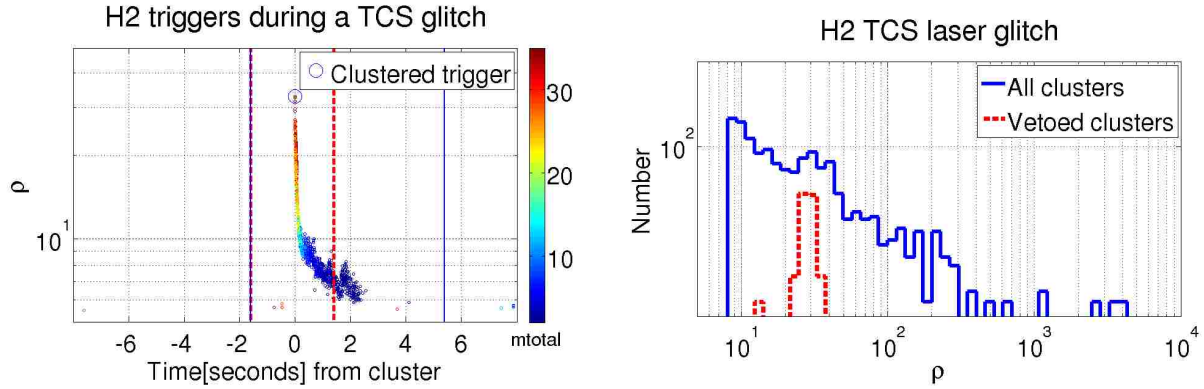

Figure 3.3: A category 2 data quality veto for a month containing glitches in the TCS lasers of H2. At right, a log-log histogram of single interferometer clusters for the CBC search with total mass between 2 and 35 solar masses, with all clusters in blue and vetoed clusters in red. At left, the effect of the transient on the production of unclustered triggers (dots), the 10 second clusters of these raw triggers (circle), the original Data Quality flag (dashed lines), and the expanded data quality veto after the window paddings are applied (solid lines).

One example of a category 2 veto is the overflow veto mentioned in Chapter 2.1.2. As is clear from the right hand plot in Figure 3.2, these veto intervals include most of the loudest clusters. Not all category 2 vetoes need to have this level of efficiency, or any efficiency at all at the most extreme ρ. For instance, we also used vetoes based on data quality flags for glitches in the lasers for the thermal compensation system (TCS). TCS heats the mirrors in order to offset changes in curvature due to heating by the main laser. These flags, with 4 seconds added to the end of the original 2 second intervals, had a R_{ED} ratio of nearly 500 for triggers above ρ of 20, but zero efficiency above ρ of 40. The R_U for this veto was over 100. As is clear in Figure 3.3, there is a population of clusters with ρ from 20 to 40 that correspond to the transients from TCS glitches in this particular search.

3.5.3 Category 3 Vetoes

The third category contains vetoes which were significantly correlated with transients, but with less understanding of the exact coupling mechanism, and thus often poorer performance in the metrics of deadtime and used percentage than category 2 vetoes. There are many sources of transient noises whose coupling is only partly understood. Site-wide events of significant duration, such as heavy winds or elevated seismic motion, intermittently lead to loud transient noises. Category 3 vetoes also include the minutes immediately preceding the loss of lock of the interferometer, when the triggers were likely due to the same instabilities that contributed to the lock loss. These vetoes, based more on the probability of transients than a direct measurement, tend to have lower used percentages, higher deadtimes, and therefore smaller ratios between the efficiency and deadtime.

The train data quality flag veto mentioned in Chapter 2.2 was in this category, for while the trains themselves were well understood, the nonlinear coupling to create sporadic high frequency glitches was not. This caused large windows defined by the presence of heightened

ground motion alone to be created, rather than targeted vetoes of the individual noise transients.

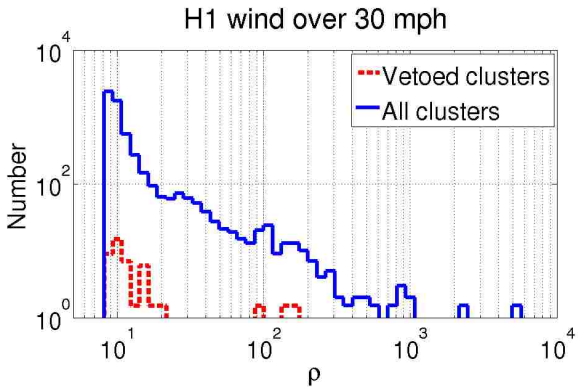

Figure 3.4: A category 3 data quality veto for a month of high winds at Hanford. A log-log histogram of single interferometer clusters, total in solid lines and vetoed in dashed lines.

Another example was elevated winds above 30 MPH at the Hanford site. This data quality veto had a R_{ED} of 17, and a R_U of 31. While this is significant, it is less than the typical value of category 2 vetoes.

3.5.4 Category 4 Vetoes

The fourth category contains vetoes with low statistical significance, often with high deadtimes. The used percentages are often near 100%, but this is a representative of the typical veto interval durations ranging from tens minutes to entire science mode segments being flagged, and thus the high probability that at least one cluster will be within the time defined (as mentioned earlier, the average clustered trigger rate was of order one per 10 minutes). Seismic flags with lower thresholds, aircraft passing within miles of the detectors, and problems recorded in the electronic logbooks at the detectors all fall within this category. These long intervals are not used as vetoes for searches, but rather are identified for the purposes of providing input to the follow up of gravitational wave candidates, when all possible factors that prompted the creation of these flags at the time of the detection candidate are scrutinized.

3.6 Examining Candidate Events After Vetoes

Candidate coincident events that occur during the times of category 2, 3, and 4 vetoes are not automatically discarded. The total deadtime of category 2 vetoes for the low mass CBC search, for example, was of order 1%. Category 3 had a deadtime of order 5%, and category 4 many times that. As the search reported no detections, it therefore included a calculation of the upper limit on the number of compact binary coalescences. The first three categories, including both data quality flag vetoes and auxiliary channel used percentage vetoes, were applied in this example search before calculating the upper limit, as they reduced the false alarm rate from these transients. Because the total veto deadtime of the applied categories

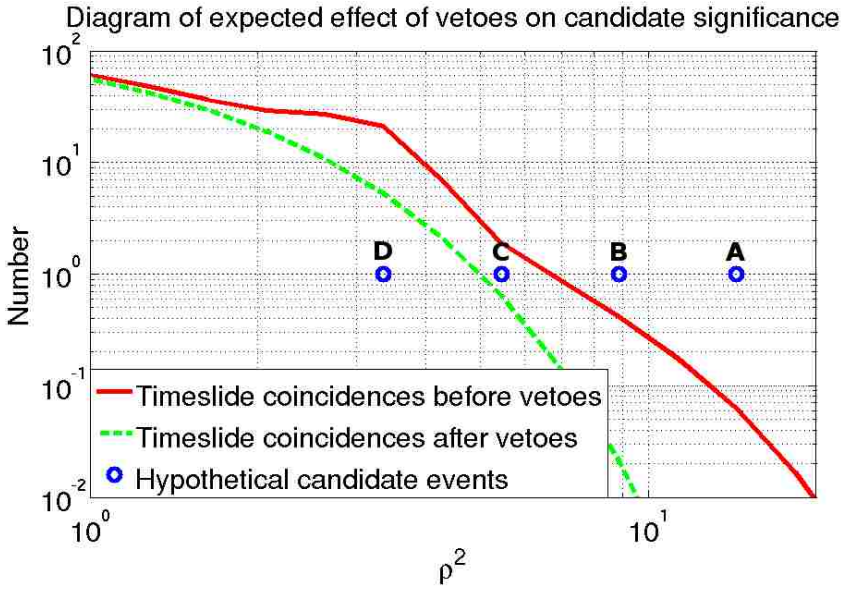

Figure 3.5: This diagram schematically represents the anticipated effect of vetoes on the significance of candidate events. The lines represent the estimated background number of coincident events expected from timeslides before (solid) and after (dashed) vetoes. The circles denote the number of foreground coincidences with ρ^2 equal to or greater than the x axis value. For the purpose of the discussion in Chapter 3.6, the points A, B, C, and D are denote hypothetical detection candidates.

was between 5% and 10% per interferometer, the probability that a true gravitational wave could be in a vetoed interval is significant.

The decisions on which vetoes to use are made prior to examination of candidates. While the veto choices were tuned on single interferometer triggers, the end product of the CBC searches are detection candidates found in coincidence in the data from multiple interferometers. In the rest of this section, we will discuss the effect that the veto categories have on coincident CBC searches.

While we are unwilling to precipitously remove all candidates in vetoed times from consideration, it is imperative to reduce the rate of accidental coincidences from the noise transients that have been identified. This can be done by examining all significant candidates with respect to the background present after each category is consecutively applied. If a candidate is not vetoed by successive veto categories, it becomes more significant, as more of the background false alarm candidates against which it is compared are removed. If a candidate is in vetoed time for a given category, it is not completely ruled out as a detection, but further investigation would be required to show such a candidate is not an artifact due to the disturbance that triggered the veto. Candidates that are vetoed by lower numbered categories are more suspect, given the firmer understanding of the vetoes that populate the first two categories. A true gravitational wave is not impossible, as a sufficiently nearby (within the Milky Way) binary system coalescence could theoretically overflow the feedback control systems. It would be apparent, however, in follow up investigations as the spectro-

gram for the data would show a large amplitude chirp signature leading up to the overflow, coherently between multiple detectors.

The diagram in Figure 3.5 illustrates the effect of vetoes that we anticipate on the significance of detection candidates. Superimposed are four hypothetical candidates with the labels A, B, C, and D. For illustration only, let us assume that there is a gravitational wave candidate at one of these points.

If the candidate is at point A, it is visible above background and significant before any vetoes are applied. If A is not vetoed after subsequent veto categories are applied, it will be the loudest candidate and significantly above the rest of the distribution, and thus a strong gravitational wave candidate. If A is vetoed, it would be plausible to believe it could still be significant with strong evidence that it did not originate from the same problems used to define the veto, as in the hypothetical example of the galactic coalescence mentioned above. Even if A is recovered, it would be compared to the background estimation before vetoes are applied, and thus have a lower significance than had it survived the vetoes originally.

If the candidate is at point B, it is visible above background, though not as significant as if it were at point A. If it is not vetoed, then B is a good candidate, and having cleared away the understood accidental triggers from transient noises, it can be followed up in depth. The reason for defining vetoes is precisely to uncover these candidates, which would be buried in the background otherwise. If it is vetoed, it is again necessary to confirm that the data artifacts prompting the veto intervals are not responsible for the candidate.

If the candidate is at point C, it is likely among the triggers with the largest ρ^2 before the vetoes are applied. Surviving the vetoes improves its ranking, reducing the background of triggers with equal or lower ρ^2. If it is vetoed, it is a problematic candidate given the population of spurious triggers that it sits in. If it survives the vetoes, it is still only a marginal candidate. Follow up analysis of the highest ρ^2 triggers will likely uncover reasons to distrust the surrounding loud candidates, but that is not enough to make C into a strong candidate. Additional veto definitions and revisions would make a candidate at C somewhat more significant, providing it is not vetoed, plausibly making it significant.

A candidate at point D is within the accidental population of triggers after vetoes are applied, with tens of triggers surrounding it with similar ρ^2. Such candidates are not detectable without additional reduction of the background. Additional veto definitions and revisions might make a candidate at D marginally more significant, but it is not at all likely to become detectable through veto efforts.

In this scenario, despite the deadtime is incurred by the vetoes, the detection confidence is increased significantly for candidates that were marginal to unobservable before, due to the reduced deadtime. It was with this philosophy the led to the application of veto categories, as described in this Chapter, to the S5 search for low mass CBC's. This veto effort is detailed in the next chapter (Chapter 4).

4. Vetoes in Searches for Compact Binary Coalescences in S5

4.1 Introduction

In October 2007, the LIGO (8) detectors completed a fifth data run over a two-year long period, denoted as S5, during which one year of triple-coincidence data was collected between the H1, H2, and L1 detectors. During the final six months of S5, the Virgo detector in Cascina, Italy joined the LIGO detectors in operation.

Veto definition efforts for S5 were complicated by several factors. The science run took place over two years, and the detectors changed significantly during this time. The search groups were interested in searching the data as quickly as possible, so unlike the shorter previous science runs of durations ranging several days to two months, the data was searched even as more data was being taken. The first CBC search performed end to end was the so called "First Epoch", consisting of the first two and a half months of S5.

The first published CBC search on S5 data was the search for systems with component masses from 1 to 34 solar masses, with a total mass less than or equal to 35 solar masses, during the first calendar year of S5 (12). This parameter range will be referred to as "low-mass". The remainder of S5 low mass searches were split in two, with the time from the end of the first year until Virgo began operation termed S5 "months 12 to 18", and from the start of Virgo's participation until the end of S5 as "LIGO-Virgo".

The veto metrics described in Section 3.4 had been used prior to S5 to evaluate the usefulness of different vetoes, though there were only a few dozen different vetoes defined at that time, rather than the over one hundred defined by the end of S5. Some of these vetoes applied in S4 and earlier runs had window paddings applied, though most were not padded before S5. Likewise, veto categorization was first attempted before S5, but candidate events were only examined after the combination of all veto categories had been applied, ignoring the substantive differences between veto categories. This was different in S5, where I determined that most vetoes needed padding, and where candidates were examined in all cases after two categories (2 and 3) and for the first year after all four veto categories.

In the following sections, the tables of veto metrics were calculated using the clustered single interferometer triggers. The clustering, as described in Chapter 3, was performed with a 4 second time window, for triggers with a minimum ρ of 8. Listed from left to right are the veto name, negative and positive window paddings, deadtime, efficiency, ratio of efficiency to deadtime, used percentage, and normalized used percentage. The metrics below are calculated for all of S5 using the recommendations for the second year of S5, unlike the actual analysis which used a less refined set of vetoes for the first year search (33). This was due to a combination of timeline pressure for publication of the first year search, and because many of the choices for the second year search were based in part on data not yet collected when the first year search was completed.

4.2 Category 1

As described in Section 2.1.2, not all the time marked as science quality data was properly searchable. Category 1 vetoes are the set of these times, which are subsequently not analyzed

despite being marked with the SCIENCE flag. These flags are synonymous with category 1 vetoes, and by their nature do not require veto padding, which are only relevant for data quality issues in time to be analyzed. In this matter, my work was limited to keeping records straight from the detector characterization, calibration, and search groups within the LSC. Metrics of veto effectiveness were not relevant; these category 1 veto times were not searched.

The OUT OF LOCK flag marked times at the end of science segments that were ended via lock loss, which the controls logging software often was 1-2 seconds late registering this end of lock. The AS TRIGGER flag refers to times in early S5 when the system that automatically switched to a more robust yet less sensitive photodiode readout was activated without dropping science mode (this was primarily an L1 phenomenon, in response to passing trains). The INVALID DARMERR flag is set based upon errors in the writing of the data files containing the gravitational wave data. The CORRUPTER RDS C03 LX flag marks times where data required to process the data in to so-called $h(t)$ strain data contains unrecoverable corrupted data. The H2 PEM INJECTION flag contains 0.2% of the H2 SCIENCE time during which experimental tests of the physical and environmental couplings of the detector were underway. These tests included generating ground and acoustic vibrations inside the LVEA, as well as large electromagnetic fields, and was mistakenly recorded as SCIENCE mode, but which was properly recorded in the electronic log as not searchable.

Table 4.1: Category 1 vetoes

H1	H2	L1
OUT OF LOCK	OUT OF LOCK	OUT OF LOCK
AS TRIGGER	AS TRIGGER	AS TRIGGER
INVALID DARMERR	INVALID DARMERR	INVALID DARMERR
CORRUPTED RDS C03 LX	PEM INJECTION	CORRUPTED RDS C03 LX
MISSING RDS C03 L2	MISSING RAW	MISSING RDS C03 L2
MISSING RAW		MISSING RAW

4.3 Category 2

In defining vetoes in S5 as Category 2, we took into account all of the metrics described in Chapter 3.4, as well as more specific knowledge of the mechanism and origins of the transients. This section describes the evaluation of the data quality flags for the category with the most significant artifacts in data that was analyzed. Category 2 vetoes generally correspond to malfunctions of the interferometer itself, in which case the veto efficiencies and deadtimes provided more confirmation of categorization than the initial impetus itself.

The Category 2 vetoes listed in table 4.2 include malfunctions in the overflows in the length and angular sensing and control systems, and in the readout photodiodes. The ASI CORR OVERFLOW flags contain times when the Anti-Symmetric port In-phase (ASI) photodiode signals rose above a threshold at which they coupled to the gravitational wave channel. The ASI channel theoretically insensitive to differential arm motions (such as might be caused by gravitational waves), but sensitive to interferometer angular alignment. The ASC Overflow flags contain times when the angular sensing and control (ASC) systems reached their maximum digital value. The MASTER OVERFLOW ASC flags are generated from

automatically generated second trends that monitor the counts in important ASC channels, respectively, and increment when any of the selected channels goes over the threshold chosen for that channel. The SEVERE OVERFLOW LSC flags are generated similarly, but with a set of only the channels that monitor the DARM, CARM, MICH, and PRC degrees of freedom of the interferometer. The PD Overflow flag contains seconds in which any of the four photodiodes reading out the anti-symmetric port saturate. The PHOTODIODE GLITCH flag contains times when one of the four readout photodiodes measures values significantly different than the other three, indicating possible alignment or electronics issues, or even dust in the beamline.

The deadtimes of these flags were all quite small with the exception of the injection flags, on order tenths of a percent for the Hanford detectors, and several times that for L1 due to greater instability induced by the larger seismic background. The majority of the deadtime for the overflow flags came from the need to add 8 second paddings before and after each two second overflow flag to account for the biasing of the inverse power spectrum estimation discussed in Chapter 1.5.4. The ratio values for H2 in particular were often highest, signifying that a greater portion of the transients in H2 were flagged by known category 2 vetoes.

Table 4.2: Category 2 vetoes for in-loop overflows. In addition to the data quality veto name and padding (P) added before and after the data quality flags, the deadtime (D), efficiency (E), ratio of efficiency to deadtime (R_{ED}), percent of veto intervals used to veto at least one triggers (U), and ratio of U to the expected value from the clustered trigger rate R_U are listed.

Name	P(s)	D(%)	E(%)	R_{ED}	U(%)	R_U
H1 ASI CORR OVERFLOW	8 8	0.00	NA	NA	NA	NA
H2 ASI CORR OVERFLOW	8 8	0.03	1.21	39.96	58.51	20.75
L1 ASI CORR OVERFLOW	8 8	1.38	7.18	5.19	35.27	3.74
H1 ASC Overflow	8 8	0.05	1.01	18.65	73.98	11.29
H2 ASC Overflow	8 8	0.04	1.60	37.60	80.31	22.01
L1 ASC Overflow	8 8	0.29	0.68	2.37	18.78	1.88
H1 MASTER OVERFLOW ASC	8 8	0.06	1.06	18.11	74.02	10.70
H2 MASTER OVERFLOW ASC	8 8	0.05	1.70	35.71	73.70	20.20
L1 MASTER OVERFLOW ASC	8 8	0.73	1.72	2.36	25.77	2.45
H1 PHOTODIODE GLITCH	0 4	0.03	0.42	14.42	84.29	3.62
H2 PHOTODIODE GLITCH	0 4	0.01	0.12	19.33	75.61	7.12
L1 PHOTODIODE GLITCH	0 4	0.08	0.55	6.63	66.97	1.89
H1 PD Overflow	8 8	1.18	1.93	1.63	15.43	2.23
H2 PD Overflow	8 8	0.02	1.39	63.39	76.18	25.52
L1 PD Overflow	8 8	0.19	1.86	9.84	54.09	5.42
H1 SEVERE LSC OVERFLOW	8 8	0.02	0.60	31.82	84.74	12.93
H2 SEVERE LSC OVERFLOW	8 8	0.02	1.38	64.03	76.28	25.56
L1 SEVERE LSC OVERFLOW	8 8	0.19	1.83	9.86	54.82	5.49

The Category 2 vetoes listed in table 4.3 correspond to problems with the calibration line generation, and the hardware injection flags. The all the flags begining with CALIB were generated by examining the output of the arbitrary waveform generator (AWG), which is

responsible for calibration lines, hardware injections, and other excitations. The DROPOUT 1 SAMPLE flag denotes times when a single sample was dropped, resulting in the injection of a discontinuity. The DROPOUT 1 SECOND flag marks times when the AWG dropped out completely for a second or more. The DROPOUT AWG STUCK contains times when the AWG repeated the same single second of data. The flag CALIB GLITCH ZG contains other large disturbances in the AWG output. The flag CALIB DROPOUT BN provides equivalent information derived from a burst algorithm termed "blocknormal", for the beginning of S5 at L1, when the other algorithms were not running. The Injection flag is unlike the other flags in that it marks times when the AWG was running correctly, and introduced transients into the data to simulate the effect of strain from gravitational waves in the interferometer. Hardware injections are performed in order to properly tune the various searches in LIGO for gravitational wave signals. Since these hardware injections are intentional and controlled, they exist entirely within known time intervals, for which data quality flags are produced. Figure 4.1 shows one such injection of a simulated CBC, with the characteristic chirp waveform evident in the increasing frequency and amplitude with time.

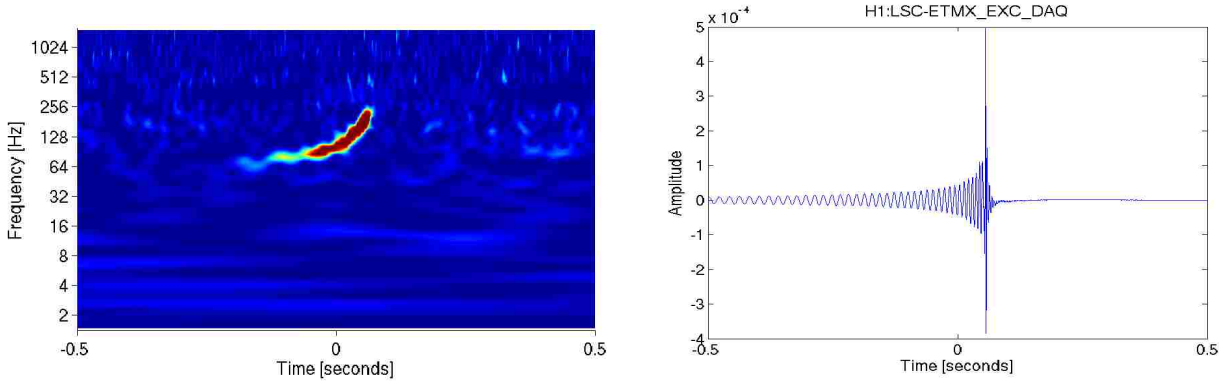

Figure 4.1: At left, a time-frequency representation of H1 gravitational wave channel during inspiral hardware injection of waveform from a binary of 10 solar mass objects at a disctance of 40 Mpc. The energy in a given time-frequency bin increases from blue to red. At left is the injected signal.

The deadtimes of these flags were all quite small, on order tenths of a percent for the Hanford detectors, and several times that for L1, with the exception of the injection flags. Injection times were chosen deterministically, and the deadtime was a function of that choice, and of the 80 total seconds of padding to each 90 second injection interval. This padding was added to veto false alarm triggers from the high amplitude Burst waveform injections that were injected up till the end of the flagged interval. Additionally, the detectors did not exist in a steady state over the run. Some of the most effective vetoes in the beginning of S5 were obsolete by the end, the artifacts they had labeled no longer being generated due to commissioning and repairs. The one second calibration line dropouts in particular are a case of this. Even though the choice to place these vetoes in category 2 was not made primarily with the veto metrics in mind, in almost all cases the ratio of efficiency to deadtime R_{ED} and the ratio of used ratio to the expected random used ratio R_U values were of order 10 to 100, indicating high statistical significance.

The vetoes listed in table 4.4 include the times when light was likely scattered from one Hanford interferometer into to the other Hanford interferometer. The H1 H2 LOCKGAIN

Table 4.3: Category 2 vetoes for calibration line errors and hardware injections. In addition to the data quality veto name and padding (P) added before and after the data quality flags, the deadtime (D), efficiency (E), ratio of efficiency to deadtime (R_{ED}), percent of veto intervals used to veto at least one triggers (U), and ratio of U to the expected value from the clustered trigger rate R_U are listed.

Name	P(s)	D(%)	E(%)	R_{ED}	U(%)	R_U
H1 CALIB DROPOUT 1SEC	10 0	0.00	0.04	22.99	98.31	20.78
H2 CALIB DROPOUT 1SEC	10 0	0.00	0.15	32.96	68.12	31.60
L1 CALIB DROPOUT 1SEC	10 0	0.00	0.00	1.50	10.53	1.58
H1 CALIB DROPOUT 1SAMPLE	10 0	0.00	0.00	0.00	0.00	0.00
H2 CALIB DROPOUT 1SAMPLE	10 0	0.00	NA	NA	NA	NA
L1 CALIB DROPOUT 1SAMPLE	10 0	0.00	0.00	1.49	8.33	1.37
H1 CALIB GLITCH ZG	10 0	0.00	0.00	24.98	80.00	19.98
H2 CALIB GLITCH ZG	10 0	0.00	0.02	91.37	66.67	36.55
L1 CALIB GLITCH ZG	10 0	0.00	0.00	16.39	100.00	16.39
L1 CALIB DROPOUT BN	0 0	0.00	NA	NA	NA	NA
H1 CALIB DROPOUT AWG STUCK	10 0	0.02	0.11	6.41	100.00	0.14
H2 CALIB DROPOUT AWG STUCK	10 0	0.00	NA	NA	NA	NA
L1 CALIB DROPOUT AWG STUCK	10 0	0.00	NA	NA	NA	NA
H1 Injection	64 16	0.56	3.04	5.46	87.93	1.78
H2 Injection	64 16	0.59	5.10	8.62	60.35	2.68
L1 Injection	64 16	0.56	2.12	3.78	84.14	1.12

flag marks the 300 seconds before H2 gains lock as a veto for H1, and H2 H1 LOCKGAIN marks the 400 seconds before H1 gains lock as a veto for H2. The H1 H2 LOCKLOSS flag vetoes the 10 seconds prior and 100 seconds after H2 loses lock as a veto for H1, while H2 H1 LOCKLOSS marks 20 seconds before and 300 seconds after H1 loses lock as a veto for H2. The reasoning is that during the times when one interferometer is unstable and its optics are swinging to either maintain or regain lock, there is a significant chance of that interferometer scattering light into the other interferometer. The H1H2 SCATTERING flags were created by examining the 1-4 Hz BLRMS minute trends of the gravitational wave channel itself, which was found to correlate with light scattering between the interferometers.

These flags have less significant ratios than the rest of the category 2 vetoes. These vetoes were a refinement on earlier flags denoting simple lack of lock of the complimentary Hanford detector (originally category 3 due to its large deadtime), which included times of transients that by their nature significantly increased the false alarm rate. The reduced deadtime of the newer flags allowed them to be treated as well understood transients in the same manner as the above vetoes, though the fewer, longer intervals did not perform as effectively.

Vetoes related to the suspension systems are shown in table 4.5. The flags with H1 SIDECOIL in their name all mark times when the H1 end test masses at the X or Y end had large currents flowing through the magnetic actuators that control the side to side mirror motion. The flags with RMS 6HZ in their name focused on a narrow BLRMS around 6 Hz of the coil readout channels. The TIDAL SERVO DESATURATION flag mark times when the tidal servo, which accounts for strains on the interferometer arms due to tidal effects

Table 4.4: Category 2 vetoes for Hanford detector crosstalk. In addition to the data quality veto name and padding (P) added before and after the data quality flags, the deadtime (D), efficiency (E), ratio of efficiency to deadtime (R_{ED}), percent of veto intervals used to veto at least one triggers (U), and ratio of U to the expected value from the clustered trigger rate R_U are listed.

Name	P(s)	D(%)	E(%)	R_{ED}	U(%)	R_U
H1 H2 LOCKGAIN	0 0	1.82	3.63	2.00	52.65	0.48
H2 H1 LOCKGAIN	0 0	2.06	5.34	2.58	35.41	0.53
H1 H2 LOCKLOSS	0 0	0.59	2.70	4.56	70.03	1.75
H2 H1 LOCKLOSS	0 0	1.43	5.03	3.51	41.72	0.79
H1 H1H2 SCATTERING	0 0	0.18	1.12	6.12	48.07	2.20
H2 H1H2 SCATTERING	0 0	0.25	2.46	9.88	27.20	2.73

on Earth due to the Moon, returns to its dynamic range after being saturated (there is a PRESATURATION flag, but it is less significant, and is thus is category 3).

The two types sidecoil vetoes had similar efficiencies and deadtimes, neither was a pure subset of the other, and so given the R_{ED}'s and R_U's of nearly 10 and 20 respectively, and the deadtimes of much less tha 1 %, we placed both in category 2. The tidal servo desaturations were short and rare, but with 93.75% used percentage, 4 times the expected random value, they were clearly strongly correlated with noise transients in H1. The high R_{ED} confirms that these events are appropriately vetoes at category 2.

Table 4.5: Category 2 H1 suspension system vetoes. In addition to the data quality veto name and padding (P) added before and after the data quality flags, the deadtime (D), efficiency (E), ratio of efficiency to deadtime (R_{ED}), percent of veto intervals used to veto at least one triggers (U), and ratio of U to the expected value from the clustered trigger rate R_U are listed.

Name	P(s)	D(%)	E(%)	R_{ED}	U(%)	R_U
H1 SIDECOIL ETMX	8 8	0.01	0.21	18.93	76.73	9.58
H1 SIDECOIL ETMY	8 8	0.20	4.02	19.99	70.42	8.79
H1 SIDECOIL ETMX RMS 6HZ	8 8	0.01	0.14	16.14	72.85	9.10
H1 SIDECOIL ETMY RMS 6HZ	8 8	0.16	2.92	18.36	69.31	8.66
H1 TIDAL SERVO DESATURATION	0 0	0.00	0.07	26.39	93.75	4.09

For other flags we examined, the decisions were complicated by limited statistics, as seen in table 4.6. The POWMAG flag was implemented to detect electromagnetic noise that could couple into the interferometers. It required coincident transients in multiple magnetometers, as individual magnetometers were shown to be unreliable detectors of significant glitches. The TCS GLITCH LOUD flag was made by examining the output of a burst search algorithm called KleineWelle (27) run on the thermal compensation system (TCS) laser power output for events of large significance, indicating glitches in the laser power pushing the ITM mirrors.

The POWMAG vetoes were useful, as evidenced by the various R_{ED} and R_U values ranging from around 5 to 20, depending on the interferometer. The very low deadtime of the flag was actually problematic in its categorization, as very little statistical evidence

was available early in S5 using CBC clusters. The combination of the understanding that electromagnetic glitches present across the site were a problem, and the metric information produced on single interferometer KleineWelle triggers, allowed us to categorize these flags as Category 2, a decision that was validated by the statistics available later, as the ratio metrics below are significant, especially for H2. The TCS GLITCH LOUD flag was another example of a flag with initially low statistics that was evaluated to belong in category 2 based on strong physical evidence, and was similarly later confirmed to belong.

Table 4.6: Category 2 POWMAG and TCS GLITCH vetoes. In addition to the data quality veto name and padding (P) added before and after the data quality flags, the deadtime (D), efficiency (E), ratio of efficiency to deadtime (R_{ED}), percent of veto intervals used to veto at least one triggers (U), and ratio of U to the expected value from the clustered trigger rate R_U are listed.

Name	P(s)	D(%)	E(%)	R_{ED}	U(%)	R_U
H1 POWMAG	4 0	0.00	0.02	8.58	17.10	7.83
H2 POWMAG	4 0	0.00	0.05	18.49	17.26	17.35
L1 POWMAG	4 0	0.04	0.29	7.00	19.99	6.00
H1 TCS GLITCH LOUD	4 0	0.00	0.04	17.91	44.68	17.54
H2 TCS GLITCH LOUD	4 0	0.00	0.24	68.33	78.48	67.61
L1 TCS GLITCH LOUD	4 0	0.00	0.00	20.31	88.89	22.89

Not all category 2 vetoes address ongoing and persistent problems in the detectors. The array of vetoes for the three detectors listed in table 4.7 mark specific time intervals that unambiguously contain manifestations of severe malfunction or anthropogenic noise coupling. The SLEDGEHAMMER flags refer to times when sledgehammers and jackhammers were being used on concrete on the Hanford site. The H2 MMT3 OPTLEVER flag contains times when the optical level that senses alignment of one of the mode matching telescope (MMT) optics that ensure the light entering the interferometer is Gaussian in profile was malfunctioning. The H2 OSEM GLITCH flag marks times for H2 when the optical sensing electro-magnets (OSEM) were glitching early in S5, which was later prevented with additional low pass filtering in the control system. The H2 ISCT10 TABLE GLITCH flags mark times when the pneumatic optical table upon which the H2 detector photodiodes were installed had insufficient pressure, meaning that the coupling to ground motion was significantly increased. The L1 BAD SENSING flag marks a time when insufficient temperature control in the Livingston LVEA, which caused mechanical resonances to shift, allowing coupling into the gravitational wave channel that distorted the calibration for this segment. The L1 RAILED RBS PZT flag contains times when a servo involving the reflected beam off of the recycling mirror at L1 was saturated. The L1 DAQ ERROR flag is analogous to the INVALID DARMERR flag of category 1, but marks the entire minute containing such issues.

These flags have metric ratios ranging from the tens to well over one hundred, and deadtimes in the hundredths of percent of science time. The SLEDGEHAMMER flag for H1 had ratios of order 30, though the H2 version had ratios only in the single digits. The MMT3 glitches were reasonably effective, with ratios of order 10, though the physical knowledge of the disturbances in the input optic mean it must be places in category 2. The OSEM GLITCH flag is amongst the most significant vetoes of all, with ratios ~ 170. Both types of H2 ISCT10 TABLE GLITCH flags performed similarly, and significantly, with R_{ED}s and R_Us of of 62 and 38, respectively. The remaining vetoes were not significant with respect to

the veto metrics, but corresponded to time intervals in which a candidate event would not be trusted, and considering their very low deadtimes, were reasonable to be vetoed.

Table 4.7: Category 2 "one time issue" vetoes. In addition to the data quality veto name and padding (P) added before and after the data quality flags, the deadtime (D), efficiency (E), ratio of efficiency to deadtime (R_{ED}), percent of veto intervals used to veto at least one triggers (U), and ratio of U to the expected value from the clustered trigger rate R_U are listed.

Name	P(s)	D(%)	E(%)	R_{ED}	U(%)	R_U
H1 SLEDGEHAMMER	0 0	0.00	0.02	30.44	39.29	35.98
H2 SLEDGEHAMMER	0 0	0.00	0.00	3.25	2.11	6.35
H2 MMT3 OPTLEVER	0 0	0.08	0.58	7.29	4.66	9.37
H2 OSEM GLITCH	2 0	0.00	0.12	168.42	83.78	168.42
H2 ISCT10 TABLE GLITCH	10 0	0.01	0.75	62.41	88.18	37.98
H2 ISCT10 TABLE GLITCH MILD	10 0	0.01	0.73	62.32	88.00	37.91
L1 BAD SENSING	0 0	0.05	0.17	3.16	50.00	0.10
L1 RAILED RBS PZT	0 0	0.02	0.24	12.87	100.00	0.27
L1 DAQ ERROR	0 0	0.00	0.00	0.67	12.50	0.19

Very few flags marking environmental or anthropogenic noise are included in this category. This is because the algorithms use to generate these flags are based on the external source of the glitches, for example on the relevant frequency of seismic noise as measured by a seismometer, rather than on the specific failure point of systems within the interferometers. These flags, and flags of interferometric origin that were cast a wider net, were placed in categories 3 or 4, based upon their performance.

4.4 Category 3

Category 3 is comprised of several groups of vetoes. There are flags derived from transients in the gravitational wave channel, and other closely related interferometer channels. There are vetoes that trigger on environmental conditions conducive to glitches, primarily seismic conditions. Finally, there are many of the most effective vetoes from category 2 that have greater paddings when included in this category. This is in order to capture the effects of the biasing of the power spectrum, as described in Section 1.5.2.

Flags derived from behavior of the interferometer are shown in table 4.8, such as drops in arm power or excess noise in the gravitational wave channel in frequency bands below one Hz, marked effects of glitchy behavior of the interferometer indicative of alignment problems and upconversion of seismic noise, respectively. The CALIB BAD COEFFS 60 flags contain minutes for which the variation of noise in the interferometer in the frequency ranges of the calibration lines caused the calibration to become less certain. The LIGHTDIP PERCENT flags mark times when alignment fluctuations cause the resonant arm power to drop by at least the percent in the title of the flag. The H1 DARM dHz flags were created by analyzing the BLRMS of the gravitational wave data in low frequencies far below the sensitive band of the interferometer, looking for the effects of seismic, as does the similar H1 SEIS DARM 5 7HZ flag. The MASTER OVERFLOW IOO flags are derived as the MASTER OVERFLOW ASC flags, but from channels corresponding to the input/output

optics (IOO) instead of angular control channels. The PRE LOCKLOSS 120 SEC flags contain the times 120 seconds before a lock-loss in any interferometer, on the understanding that these periods are likely to contain increased instability.

These flags had higher deadtime in general than the flags of category 2, and metric ratios that were lower, with metric ratios between of order 3 and 20. They therefore were correlated statistically with glitches, but by their nature demanded close inspection of their safety with respect to vetoing actual gravitational wave signals. The 5 to 7 Hz motion in differential arm motion and the overflows in the input optics both would have qualified for category 2 by veto metrics, as would the L1 CALIB BAD COEFFS 60. The former was placed in category 3 due to initially low number statistics, combined with safety concerns due to the use of the gravitational wave channel. Though it has proved safe and effective in retrospect, this was not obvious initially. The overflows were late additions, with no H2 intervals left in science time, and only a small number of intervals available for L1. The slight efficiency of 0.01 % over 96 seconds of vetoed time did not have a significant impact on the overall veto effort by being placed in category 3.

Table 4.8: Category 3 vetoes from differential arm motion transients. In addition to the data quality veto name and padding (P) added before and after the data quality flags, the deadtime (D), efficiency (E), ratio of efficiency to deadtime (R_{ED}), percent of veto intervals used to veto at least one triggers (U), and ratio of U to the expected value from the clustered trigger rate R_U are listed.

Name	P(s)	D(%)	E(%)	R_{ED}	U(%)	R_U
H1 CALIB BAD COEFFS 60	0 0	0.00	NA	NA	NA	NA
H2 CALIB BAD COEFFS 60	0 0	0.04	0.14	3.94	100.00	0.16
L1 CALIB BAD COEFFS 60	0 0	0.00	0.03	24.72	100.00	0.76
H1 LIGHTDIP 02 PERCENT	2 2	0.51	3.20	6.23	16.27	6.39
H2 LIGHTDIP 04 PERCENT	2 2	1.75	6.69	3.81	4.39	3.78
L1 LIGHTDIP 04 PERCENT	2 2	2.04	11.34	5.56	23.99	5.41
H1 DARM 09 11 dHz LOWTHRESH	0 0	2.77	6.62	2.39	44.59	2.04
H1 DARM 11 13 dHz LOWTHRESH	0 0	2.58	6.19	2.39	47.17	2.16
H1 DARM 18 24 dHz LOWTHRESH	0 0	0.75	2.15	2.86	37.89	1.74
H1 DARM 50 70 dHz LOWTHRESH	0 0	0.23	3.25	14.14	88.11	4.03
H1 SEIS DARMERR 5 7HZ	0 0	0.06	1.36	23.09	93.61	4.29
H2 MASTER OVERFLOW IOO	8 8	0.00	NA	NA	NA	NA
L1 MASTER OVERFLOW IOO	8 8	0.00	0.01	18.98	100.00	9.49
H1 PRE LOCKLOSS 120 SEC	0 0	0.19	0.31	1.60	13.66	0.67
H2 PRE LOCKLOSS 120 SEC	0 0	0.26	0.56	2.17	8.19	0.88
L1 PRE LOCKLOSS 120 SEC	0 0	0.32	0.56	1.76	22.61	0.73

Some specific sources of ground motion were targeted as shown in table 4.9, such as freight trains that pass LIGO Livingston daily (described in Section 2.2), and airplanes that sporadically pass both sites. The H1 TIDAL SERVO PRESATURATION flag contains the times when the tidal servo runs out of dynamic range and saturates. The H2 FM ROLLMODE EXCITED flags times when an air compressor on the Hanford site was vibrating in the frequency range of roll modes of the mirrors that direct the light from H2 into the long arms

shared with H1. The TRAIN LIKELY flag was created as described in Chapter 2.2. The DEWAR GLITCH flags mark times when the LN2 dewars on site glitched significantly. The Wind Over 30MPH flags contain times when the wind was over 30 Mph on the Hanford site as measured by local weather stations. The POWERMAINS flags mark power glitches and disruptions in the power station serving the Hanford site. The H1 SEISMIC EY 3 10 99PCTL flag marks times where the seismic motion at the Hanford Y end in the 3 to 10 Hz BLRMS minute trends was in the 99th percentile for different epochs across S5. The SEISMIC 30 100 mHz flags were made from the 0.03 to 0.1 Hz BLRMS minute trends at the end stations at the two sites, setting three thresholds for each, from which a set was chosen based on the veto metrics.

The tidal servo, rollmode, high wind, H1 dewar, and various seismic flags had ratios from 3 to 5. The H2 dewar glitch, on the other hand was very significant with ratios of 27, indicating that this was more of a problem for H2. The train flag was only marginally effective, even after the windows were narrowed using negative paddings. The powermains flags were included based on additional knowledge from coincident burst KleineWelle triggers, indicating that they were efficient for lower ρ triggers that were found in coincidence at the Hanford site.

Table 4.9: Category 3 vetoes from ground motion, suspension noise, and powerlines. In addition to the data quality veto name and padding (P) (P) added before and after the data quality flags, the deadtime (D), efficiency (E), ratio of efficiency to deadtime (R_{ED}), percent of veto intervals used to veto at least one triggers (U), and ratio of U to the expected value from the clustered trigger rate R_U are listed.

Name	P(s)	D(%)	E(%)	R_{ED}	U(%)	R_U
H1 TIDAL SERVO PRESATURATION	0 0	0.01	0.04	4.80	80.00	0.23
H2 FM ROLLMODE EXCITED	0 0	0.78	5.35	6.86	32.76	3.95
L1 TRAIN LIKELY	-360 -360	1.05	1.82	1.73	51.20	0.39
H1 DEWAR GLITCH	0 0	0.00	0.00	2.29	3.33	2.29
H2 DEWAR GLITCH	0 0	0.00	0.02	27.60	18.31	27.60
H1 Wind Over 30MPH	8 8	0.22	1.31	6.05	31.69	4.15
H2 Wind Over 30MPH	8 8	0.17	0.78	4.60	13.08	3.58
H1 POWERMAINS DISRUPTION	0 0	0.49	0.66	1.34	36.54	0.55
H2 POWERMAINS DISRUPTION	0 0	0.48	0.62	1.28	17.60	0.59
H1 POWERMAINS GLITCH	0 0	0.01	0.02	2.35	3.42	2.35
H2 POWERMAINS GLITCH	0 0	0.01	0.02	2.86	1.90	2.86
H1 SEISMIC EY 99PCTL 3 10HZ	10 10	1.24	5.12	4.14	40.76	1.40
H1 SEISMIC X 30 100 mHz HIGHTHRESH	0 0	0.21	1.06	4.97	32.50	1.49
H1 SEISMIC Y 30 100 mHz HIGHTHRESH	0 0	0.50	1.75	3.51	32.31	1.48
L1 SEISMIC X 30 100 mHz MEDTHRESH	0 0	0.80	4.00	5.03	55.87	1.68
L1 SEISMIC Y 30 100 mHz MEDTHRESH	0 0	1.04	3.93	3.78	49.70	1.49
L1 SEISMIC X 30 100 mHz HIGHTHRESH	0 0	0.40	2.64	6.67	64.75	1.95
L1 SEISMIC Y 30 100 mHz HIGHTHRESH	0 0	0.51	2.44	4.77	55.89	1.68

Shown in table 4.10 are various one-off flags, marking times of known external effects, labeled by operators and science monitors on site in the detectors electronic notebook, which

were later turned into data quality flags. Many of these flags, particularly those that end with the word "glitchiness", describe their motivation in their names, such as earthquakes, poor sensitivity to BNS measured by lower range, increased rate of observed glitches, nearby road traffic, tumbleweed bailing, and a hurricane. Others, such as the CONCRETE WORK and ISCT10 TROUBLE flags contain the times initially identified as containing problems for which more precise flags were later derived, such as SLEDGEHAMMER and ISCT10 TABLE GLITCH, respectively. The H2 SICK flag contains a variety of truly terrible behavior that was likely largely covered by a variety of lightdip and overflow flags, but that the searches are better off just skipping in their entirety. The TCS and ASC TROUBLE flags similarly include segments containing an abnormally large number of TCS glitches and ASC overflows contributing to reduction in range. The L1 BS OPTLEVER flags mark times when the beam splitter optical lever was malfunctioning.

Most of these vetoes were of similar significance to the flags derived from the interferometer response mentioned above, were generated for short epoch containing known increased glitchiness rather than labeling individual glitches, and so were placed in category 3. Since most of these vetoes were for a single interval marking many minutes, or a small set of such intervals, they had used percentages at or near 100 %. Since an interval with multiple clusters within it counts as being "used" only once, this results in values for R_U below unity. The metric R_{ED} tells us of the significance of these vetoes more clearly, with values from 2 to 50.

Table 4.11 contains flags described in category 2, but which flagged transients loud enough that they incurred the severe issues described in Chapter 1.5.4 and shown in Figure 1.8, namely the biasing of the inverse power spectral density calculation. For this reason, the ± 8 second window paddings were added. Additionally, the positive padding was expanded to 25 seconds for the triggers occurring just over one template duration after the impulsive glitch itself, as shown in Figure 3.1.

4.5 Category 4

The fourth veto category served as a catch-all repository for science mode segments during which there is plausible reason to believe noise transients may be being introduced into the data, producing false alarm triggers, yet there is insufficient direct evidence or correlation with clustered triggers to place the vetoes in a lower category. This category is plausibly useful for the purpose of performing a search on only the cleanest, most stationary data, but the cost is high. For all three interferometers, the deadtime accrued by using all four veto categories is roughly 20 %, over half of which is from category 4 alone (this is discussed further in the next section). The searches for CBC's in S5 did not use category 4 when calculating their upper limit, though the loudest candidates remaining after category 4 were followed up as for the other categories.

Table 4.12 lists the category 4 vetoes for activity local to the detector site due to human activity. The AIRCRAFT LIKELY and AIRCRAFT VERY LIKELY flags identify minutes when multiple microphones across the site register Doppler shifted acoustic noise, indicating the presence of airplanes. The flags that end in ACTIVITY were manually activated by the operators at Hanford when the described activity was present sufficiently to couple into the interferometers in their opinion. The flags that end in ELOG, like the flags that end in GLITCHINESS, are derived from manual investigation of the electronic detector log and figures of merit searching for segments containing excess transient noises. The L1 EX LOGGING flag contains times near the end of S5 when logging activity was present near the X end station, as visible in seismic BLRMS figures of merit. The performance of the category 4 flags was, by definition, weak. The metric ratios were rarely above 2, and the deadtimes

Table 4.10: Category 3 "one time issue" vetoes. In addition to the data quality veto name and padding (P) added before and after the data quality flags, the deadtime (D), efficiency (E), ratio of efficiency to deadtime (R_{ED}), percent of veto intervals used to veto at least one triggers (U), and ratio of U to the expected value from the clustered trigger rate R_U are listed.

Name	P(s)	D(%)	E(%)	R_{ED}	U(%)	R_U
H1 BN GLITCHINESS	0 0	0.00	0.02	29.88	100.00	0.83
H1 CONCRETE WORK	0 0	0.01	0.04	3.93	50.00	0.05
H2 CONCRETE WORK	0 0	0.01	0.01	0.53	50.00	0.11
H2 SICK	0 0	0.88	11.81	13.38	76.00	0.16
H2 ROUTE10 TRAFFIC	0 0	0.00	0.03	10.05	100.00	0.40
H2 SENSEMON RANGE STEP	0 0	0.02	0.08	4.24	100.00	0.15
H2 ASC TROUBLE	0 0	0.01	0.06	4.81	100.00	0.10
H2 BALING ACTIVITY	0 0	0.02	0.23	12.85	100.00	0.15
H2 ISCT10 TROUBLE	0 0	0.01	0.27	24.08	100.00	0.12
H2 STACK RESONANCE	0 0	0.00	0.10	52.26	100.00	0.67
H2 TCS TROUBLE	0 0	0.03	0.15	5.70	100.00	0.05
H2 BADMONTH**	0 0	–	–	–	–	–
H2 EARTHQUAKE GLITCHINESS	0 0	0.00	0.00	0.00	0.00	0.00
L1 EARTHQUAKE GLITCHINESS	0 0	0.24	0.79	3.26	97.06	0.08
L1 BADRANGE GLITCHINESS	0 0	0.02	0.17	10.53	100.00	0.16
L1 ELEVATED GLITCHINESS	0 0	0.51	1.03	2.01	47.67	0.06
L1 SEVERE GLITCHINESS	0 0	0.36	0.86	2.41	68.18	0.05
L1 HURRICANE GLITCHINESS	0 0	0.12	0.56	4.66	62.50	0.03
L1 BAD SERVO	0 0	0.00	0.00	0.00	0.00	0.00
L1 BS OPTLEVER HIGHRMS	0 0	0.14	0.35	2.58	37.46	0.56
L1 BS OPTLEVER	0 0	0.33	0.62	1.87	42.31	0.64
L1 BS OPTLEVER GAINPEAKING	0 0	0.21	0.32	1.57	49.13	0.43
L1 LVEA NOISY	0 0	0.04	0.09	1.97	66.67	0.05

Table 4.11: Category 3 expanded padding of category 2 vetoes. In addition to the data quality veto name and padding (P) added before and after the data quality flags, the deadtime (D), efficiency (E), ratio of efficiency to deadtime (R_{ED}), percent of veto intervals used to veto at least one triggers (U), and ratio of U to the expected value from the clustered trigger rate R_U are listed.

Name	P(s)	D(%)	E(%)	R_{ED}	U(%)	R_U
H1 ASI CORR OVERFLOW	25 8	0.00	NA	NA	NA	NA
H2 ASI CORR OVERFLOW	25 8	0.06	1.50	26.69	61.83	10.97
L1 ASI CORR OVERFLOW	25 8	2.15	8.58	3.99	42.10	2.23
H1 ASC Overflow	25 8	0.09	1.23	13.22	75.68	5.94
H2 ASC Overflow	25 8	0.06	1.88	31.77	83.77	12.63
L1 ASC Overflow	25 8	0.46	0.86	1.85	24.49	1.26
H1 MASTER OVERFLOW ASC	25 8	0.10	1.28	13.06	75.83	5.79
H2 MASTER OVERFLOW ASC	25 8	0.07	2.01	29.99	75.05	11.60
L1 MASTER OVERFLOW ASC	25 8	0.99	2.00	2.01	31.41	1.57
H1 PD Overflow	25 8	1.36	2.37	1.74	24.16	1.79
H2 PD Overflow	25 8	0.04	1.63	40.21	76.11	13.11
L1 PD Overflow	25 8	0.35	2.37	6.82	54.99	2.83
H1 SEVERE LSC OVERFLOW	25 8	0.03	0.91	26.51	85.01	6.67
H2 SEVERE LSC OVERFLOW	25 8	0.04	1.63	40.53	76.42	13.17
L1 SEVERE LSC OVERFLOW	25 8	0.34	2.29	6.71	55.77	2.87
H2 OSEM GLITCH	25 8	0.01	0.15	17.62	84.55	15.00

were often in the several percent range. For the aircraft, it is likely that the acoustic damping, improved partially in response to the burst search candidate for S2 (32) that motivated the AIRCRAFT flags in the first place, was responsible for the lack of significant coupling. The ACTIVITY flags had no consistent criteria amongst the tens of operators, and the ELOG and L1 EX LOGGING flags marked long epochs for effects that often were caught by more specific or automated flags.

Table 4.12: Category 4 vetoes for plausible environmental noise sources with poor veto metrics. In addition to the data quality veto name and padding (P) added before and after the data quality flags, the deadtime (D), efficiency (E), ratio of efficiency to deadtime (R_{ED}), percent of veto intervals used to veto at least one triggers (U), and ratio of U to the expected value from the clustered trigger rate R_U are listed.

Name	P(s)	D(%)	E(%)	R_{ED}	U(%)	R_U
H1 AIRCRAFT VERY LIKELY	0 0	3.88	4.41	1.14	26.32	0.60
H1 AIRCRAFT LIKELY	0 0	4.00	4.62	1.16	26.74	0.61
H2 AIRCRAFT VERY LIKELY	0 0	3.84	4.26	1.11	10.82	0.54
H2 AIRCRAFT LIKELY	0 0	3.96	4.43	1.12	11.00	0.55
L1 AIRCRAFT VERY LIKELY	0 0	1.34	1.46	1.09	31.41	0.47
L1 AIRCRAFT LIKELY	0 0	1.43	1.54	1.08	32.16	0.48
H1 HUMAN ACTIVITY	0 0	0.00	0.00	4.30	33.33	1.06
H2 HUMAN ACTIVITY	0 0	0.00	0.00	1.34	50.00	1.34
H1 LAB ACTIVITY	0 0	0.00	0.00	0.00	0.00	0.00
H1 MACHINE ACTIVITY	0 0	0.55	1.50	2.73	65.15	0.07
H2 MACHINE ACTIVITY	0 0	0.55	1.20	2.20	57.14	0.15
H1 VEHICULAR ACTIVITY	0 0	0.71	1.26	1.77	60.00	0.18
H2 VEHICULAR ACTIVITY	0 0	0.81	1.04	1.28	60.19	0.38
H1 OTHER ACTIVITY	0 0	0.95	0.60	0.63	72.04	0.07
H2 OTHER ACTIVITY	0 0	0.65	1.29	1.97	50.00	0.17
H1 COMMISSIONING ELOG	0 0	0.01	0.04	5.13	50.00	0.07
H2 COMMISSIONING ELOG	0 0	0.04	0.05	1.53	100.00	0.04
H1 EARTHQUAKE ELOG	0 0	0.04	0.10	2.48	100.00	0.05
H2 EARTHQUAKE ELOG	0 0	0.02	0.00	0.24	33.33	0.14
L1 EX LOGGING	0 0	1.52	0.89	0.59	58.00	0.04

Table 4.13 lists the category 4 vetoes for non-astrophysical noise transients due to detector malfunctions. The NO CALIB LINE flags were a late addition marking entire segments when no calibration line was injected. These flags are degenerate with the CALIB DROPOUT 1SEC flags. The CHECKSUM MISMATCH flags contains times in the beginning of S5 when the two framebuilder computers that write the archived data at each site wrote inconsistent frames due to one or both becoming computationally overloaded. The L1 BAD CALIBRATION NEAR 7KHZ flag contained times when the suspension actuation was mistuned for the extremely high frequency range near 7KHz. The H1 COIL UPCONVERSION flag was constructed by observing that high coil currents at low frequency bands were correlated with excess noise in the sensitive 70-110 Hz band. The flags ending with COIL OVERFLOW were

created to automatically monitor coil currents at the end test masses of H1 and H2. The COSMIC RAY flags were produced by a cosmic ray shower scintillator based detector placed at the Hanford corner station, in order to investigate possible couplings. The L1 PHOTODIODE OFF flag marks an interval late in S5 when one of the four output photodiodes was accidentally left disconnected, reducing overall sensitivity of L1 by 25%. The L1 BSOPLEV 3p6HZOSCILLATIONS flag was the first to mark segments corresponding to the L1 beam splitter optical lever gainpeaking. The L1 MOVED LVEA SEIS flag marked times when a seismometer in the LVEA was out of its normal position. The L1 TCS ITMX LIGHTDIP PERCENT flags marked times when the TCS laser directed at the L1 X arm intermediate test mass had drops of 10 and 20 percent in second trends of the power output. The PROCESSOR TROUBLE ELOG flag was created by inspection of the electronic log book as the other flags with the ELOG suffix, as were the H2 MMT3 YAW SATURATION and L1 SPOB GLITCHINESS flags. The H2 MMT3 GLITCHINESS flag was a earlier version of the MMT3 OPLEVER made from minute trends.

The NO CALIB LINE flags did not flag a phenomenon that would obviously lead to transients. The CHECKSUM MISMATCH flags were not statistically significant. The L1 BAD CALIBRATION NEAR 7HZ flag was only relevant far above the sensitive frequencies of the detector to gravitational waves from CBCs. The H1 COIL UPCONVERSION flags were late to S5, and provided little benefit after the rest of category 3 was applied, though arguably should have been included anyway. The Hanford ETM COIL OVERFLOW flags were not satisfactory to their creator, and were explicitly not recommended for use, and though H2 ETMX COIL OVERFLOW seems an outlier with high ratios, this is a matter of small number statistics, as the flag marks less than five thousandths of one percent of science time. The COSMIC RAY flags had no perceptible effect. The L1 PHOTODIODE OFF flag marked reduced sensitivity, but there was no increase in transient noise. The L1 BSOPLEV 3p6HXOSCILLATIONS marked entire segments, while flags created later were more finely tuned to the glitches from beam splitter gainpeaking, maintaining efficiency while significantly reducing the deadtime. The disposition of a seismometer has no effect on the data, so L1 MOVED LVEA SEIS was not relevant. The L1 TCS ITMX LIGHTDIP flags had weak correlations as viewed by the ratios, as did the PROCESSOR TROUBLE ELOG, H2 MMT3 YAW SATURATION, and L1 SPOB GLITCHINESS flags. The H2 MMT3 GLITCHINESS flag was superseded by the more refined H2 MMT3 OPLEVER flag.

The flags in table 4.14 are more aggressive versions of flags included in category 3. The MASTER OVERFLOW LSC and H1 LIGHTDIP 04 PERCENT flags have the ± 8 second paddings due to the loud glitches they sometimes contain. The MASTER OVERFLOW SUS flags are included as they generally have small statistics, with varying effectiveness, and were difficult to classify for most of the science run. The exception is L1 MASTER OVERFLOW SUS MC2, which has very large deadtime of 3.5%, and a modest R_{ED} of 2.4. H2 LIGHTDIP 04 PERCENT and L1 TRAIN LIKELY likewise have larger paddings than the category 3 versions, and poor veto metric values. The Not Locked flags contain all times when one Hanford interferometer was locked, and the other was not, inducing large deadtimes and including times when crosstalk might not have been a factor. The flags in table 4.4 veto the same events with less deadtime, removing the need for these flags in category 3. The Hanford SEISMIC 30 100 mHz LOWTHRESH flags are the lowest threshold versions of flags that were applied in category 3, and have ratios of order one to a few.

Table 4.13: Category 4 vetoes for plausible instrumental noise sources with poor veto metrics. In addition to the data quality veto name and padding (P) added before and after the data quality flags, the deadtime (D), efficiency (E), ratio of efficiency to deadtime (R_{ED}), percent of veto intervals used to veto at least one triggers (U), and ratio of U to the expected value from the clustered trigger rate R_U are listed.

Name	P(s)	D(%)	E(%)	R_{ED}	U(%)	R_U
H1 NO CALIB LINE	0 0	0.02	0.13	5.39	100.00	0.09
H2 NO CALIB LINE	0 0	0.04	0.14	3.84	100.00	0.07
L1 NO CALIB LINE	0 0	0.00	0.00	0.00	0.00	0.00
H1 CHECKSUM MISMATCH	0 0	0.48	0.44	0.93	18.14	1.56
H2 CHECKSUM MISMATCH	0 0	0.56	0.58	1.03	14.27	2.69
L1 BAD CALIBRATION NEAR 7KHZ	0 0	0.15	0.04	0.28	55.56	0.03
H1 COIL UPCONVERSION	0 0	0.57	3.30	5.81	54.62	3.75
H1 ETMX COIL OVERFLOW	0 0	0.21	0.32	1.49	1.07	2.93
H1 ETMY COIL OVERFLOW	0 0	0.93	0.92	0.99	0.72	1.99
H2 ETMX COIL OVERFLOW	0 0	0.00	0.01	25.03	7.14	43.07
H2 ETMY COIL OVERFLOW	0 0	2.10	0.79	0.38	88.10	0.05
H1 COSMIC RAY	0 0	0.00	0.00	0.00	0.00	0.00
H2 COSMIC RAY	0 0	0.00	0.00	0.00	0.00	0.00
L1 PHOTODIODE OFF	0 0	0.07	0.04	0.60	66.67	0.05
L1 BSOPLEV 3p6HZOSCILLATIONS	0 0	0.15	0.20	1.36	72.73	0.04
L1 MOVED LVEA SEIS	0 0	0.22	0.33	1.48	33.33	0.04
L1 TCS ITMX LIGHTDIP 10 PERCENT	4 0	0.00	0.00	2.62	29.41	2.65
L1 TCS ITMX LIGHTDIP 20 PERCENT	4 0	0.00	0.00	1.24	11.11	1.25
H1 PROCESSOR TROUBLE ELOG	0 0	0.24	0.72	3.04	71.43	0.02
H2 PROCESSOR TROUBLE ELOG	0 0	0.27	0.18	0.67	75.00	0.04
H2 MMT3 YAW SATURATION	0 0	0.10	0.04	0.42	100.00	0.03
H2 MMT3 GLITCHINESS	0 0	0.37	0.87	2.36	81.82	0.04
L1 SPOB GLITCHINESS	0 0	0.91	0.45	0.50	49.09	0.04

Table 4.14: Category 4 vetoes that expand on category 3 vetoes with lower threshold or larger padding. In addition to the data quality veto name and padding (P) added before and after the data quality flags, the deadtime (D), efficiency (E), ratio of efficiency to deadtime (R_{ED}), percent of veto intervals used to veto at least one triggers (U), and ratio of U to the expected value from the clustered trigger rate R_U are listed.

Name	P(s)	D(%)	E(%)	R_{ED}	U(%)	R_U
H1 MASTER OVERFLOW SUS MC2	0 0	0.00	0.00	13.88	15.62	14.31
H2 MASTER OVERFLOW SUS MC2	0 0	0.01	0.04	3.28	37.50	56.54
L1 MASTER OVERFLOW SUS MC2	2 2	3.54	8.46	2.39	13.53	2.44
H1 MASTER OVERFLOW LSC	25 8	1.39	2.51	1.81	25.49	1.84
H2 MASTER OVERFLOW LSC	25 8	0.04	1.74	39.31	74.62	12.50
L1 MASTER OVERFLOW LSC	25 8	0.36	2.44	6.72	55.48	2.78
H1 MASTER OVERFLOW SUS RM	25 8	0.00	0.02	25.44	88.89	6.78
L1 MASTER OVERFLOW SUS RM	2 0	0.00	0.01	23.26	58.06	20.93
H2 LIGHTDIP 04 PERCENT	8 8	4.01	10.59	2.64	6.63	2.10
L1 TRAIN LIKELY	-60 -60	2.65	3.70	1.39	58.54	0.24
H1 H2 Not Locked	0 15	3.39	6.05	1.78	68.70	0.78
H2 H1 Not Locked	0 15	2.91	6.67	2.29	43.71	1.03
H1 SEISMIC X 30 100 mHz LOWTHRESH	0 0	1.01	1.99	1.98	20.52	0.94
H1 SEISMIC Y 30 100 mHz LOWTHRESH	0 0	2.63	3.38	1.29	15.87	0.73
H2 SEISMIC X 30 100 mHz LOWTHRESH	0 0	0.84	1.22	1.46	9.77	0.98
H2 SEISMIC Y 30 100 mHz LOWTHRESH	0 0	2.11	2.71	1.28	9.23	0.93
L1 SEISMIC X 30 100 mHz LOWTHRESH	0 0	2.78	8.36	3.00	45.42	1.36
L1 SEISMIC Y 30 100 mHz LOWTHRESH	0 0	3.67	9.35	2.55	43.12	1.30

4.6 Effects of Category Vetoes on Single Interferometer Triggers

This section describes the overall effect of the veto categories on each interferometer. Plotted for each interferometer are the clusters with $\rho \geq 12$ per day over the course of the S5 science run, and a log-log histogram of all clusters by ρ. For each of these two plots, the clusters remaining after categories 1, 2, 3, and 4 are plotted in red, yellow, green and blue, respectively. The set of clusters for each interferometer have different phenomenologies, and the veto categories have different efficiencies for different ρ ranges, and different deadtimes.

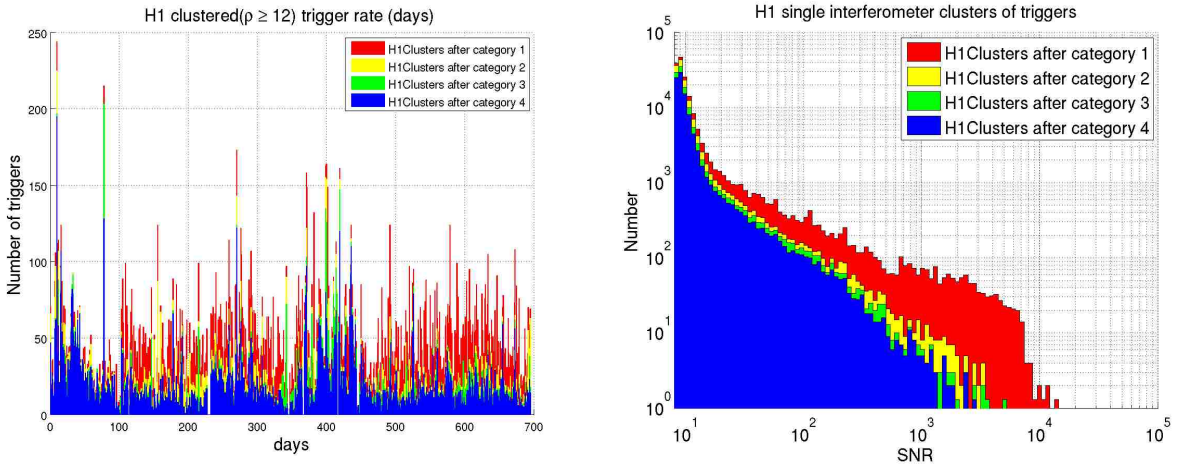

Figure 4.2: Histograms of single interferometer triggers by time and by ρ remaining after Categories 1, 2, 3, and 4 are applied.

The histogram and time series of the rate of the H1 clustered triggers is shown in Figure 4.2. The median number of clusters per day was 40 after category 1 vetoes, and reduced to 22, 17, and 14 after categories 2, 3, and 4 are applied, respectively. The vetoes have more limited effectiveness in the first epoch, which corresponds to the time from mid-November 2005 through January 2006.

The ρ histogram for H1 illustrates that the largest impact on the number of triggers with $\rho \geq 12$, and on the ρ value of the loudest single interferometer triggers, was obtained by the category 2 vetoes. The category 3 vetoes are primarily effective on clusters with $\rho \geq 200$, having little effect at lower ρ. The category 4 vetoes do not have a strong effect in this interferometer. The deadtimes for each category by itself are 0.83% for category 1, 4.11 % for category 2, 8.31 % for category 3, and 14.77 % for category 4. Combining categories 1 and 2 vetoes 4.92 % science time, combining categories 1, 2, and 3 vetoes 11.40 % science time, and combining all categories vetoes 21.92 % science time.

The histogram and time series of the rate of the H2 clustered triggers is shown in Figure 4.3. The median number of clusters per day was 20 after category 1 vetoes, and 11, 8, and 7 after categories 2, 3, and 4 were applied, respectively. There is a two week long period starting at day 120 of extremely high trigger rate. While it was thought to be correlated with alignment, or possibly the laser intensity stabilization servo, the precise cause of the instability was never diagnosed. Category 3 vetoes make a significant impact on the loudest of these periods, on March 8th and 9th, and the median rate reduces from its peak of 159

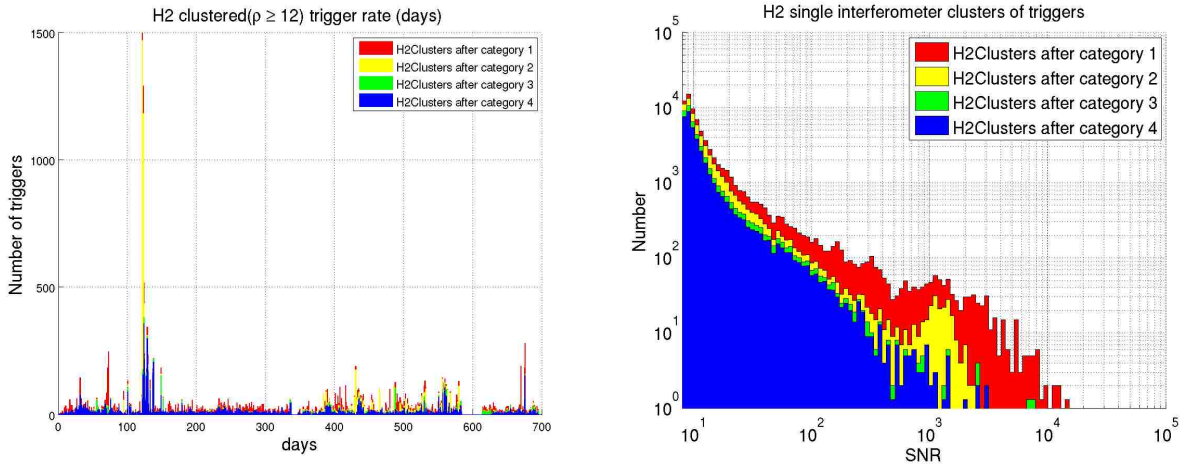

Figure 4.3: Histograms of single interferometer triggers by days and ρ remaining after Categories 1, 2, 3, and 4 are applied.

to 96 for this period. Another obvious interval of interest was from days 584 to 613, where there is a gap containing no triggers. This was the so called "bad month" of H2 data, during which extreme detector instability and lack of range made analysis of the data unproductive.

The deadtimes for each category individually are 0.02 % for category 1, 3.54 % for category 2, 4.40 % for category 3, and 16.5303 % for category 4. Combining categories 1 and 2 vetoes 3.56 % science time, combining categories 1, 2, and 3 vetoes 7.50 % science time, and combining all categories vetoes 20.06 % science time.

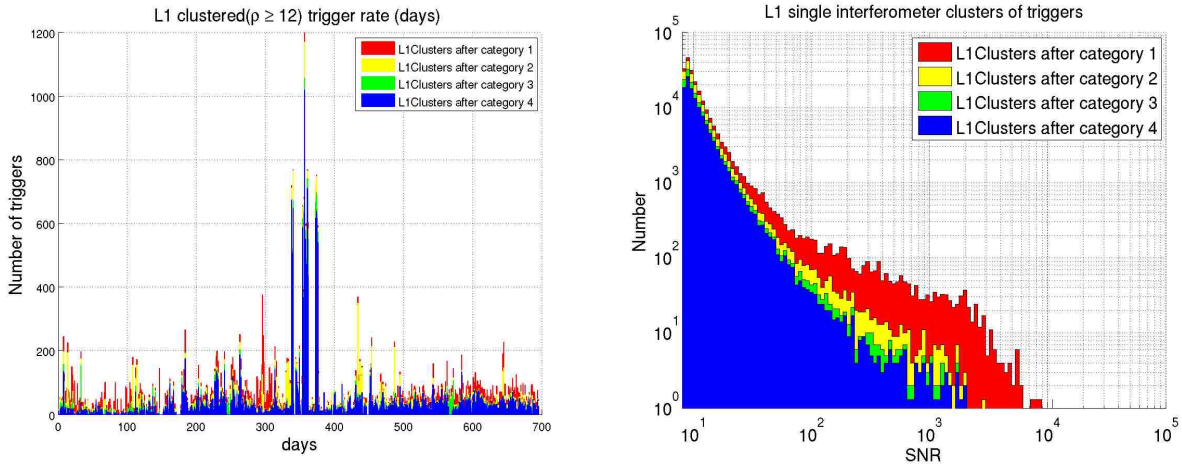

Figure 4.4: Histograms of single interferometer triggers by days and ρ remaining after Categories 1, 2, 3, and 4 are applied.

The histogram and time series of the rate of the L1 clustered triggers is shown in Figure 4.4. The median number of clusters per day was 53 after category 1 vetoes, and reduced to 36,

27, and 22 after categories 2, 3, and 4 are applied, respectively. By far the dominant features are the spikes up to above 600 triggers per day that occur between days 350 through 450. This actually is due to multiple effects, including computer overloading and large motion in the "microseismic" back from 0.10 to 0.35 Hz. This is the same time period that H1 experience elevated trigger rate.

The deatimes for each category individually are 0.26 % for category 1, 2.89 % for category 2, 8.82 % for category 3, and 14.01 % for category 4. Combining categories 1 and 2 vetoes 3.14 % science time, combining categories 1, 2, and 3 vetoes 9.72 % science time, and combining all categories vetoes 19.68 % science time.

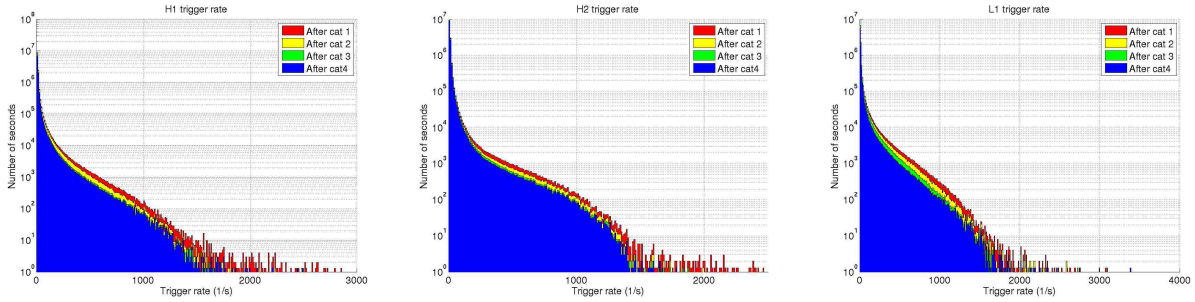

Figure 4.5: Histograms of raw single interferometer trigger rate remaining after Categories 1, 2, 3, and 4 are applied.

4.7 Effects of Category Vetoes on Coincident Analysis

As discussed in Chapter 1.5.3, the final product of the CBC search is not single interferometer triggers, but coincident candidates between multiple interferometers. A given false alarm trigger due to a transient of non-astrophysical origin in a single detector has little chance of being found in coincidence in one, let alone two, other detectors, but as seen in Figure 4.5, there can be thousands of such triggers in a given second. The chances that at least one of these triggers will be found in coincidence are non-negligible.

The effectiveness of veto categories will be illustrated with results from the search of the first year of S5 data for CBC's with component masses between 1 and 34 solar masses, and total mass less than 35 solar masses. The vetoes reduce the background from false alarms by removing the times that contain the highest rate of triggers and the highest ρ triggers in each single interferometer. This in turn reduces the rate of coincident triggers found in the time-slides, making the surviving un-shifted coincident triggers stand out more above background. The remainder of this Chapter will work in terms of combined $\rho^2_{\rm eff}$, defined from equation 1.16, which is a more comprehensive description of coincident triggers.

The three interferometers were not always in science mode, and even when they were, the veto categories impose further deadtime on the searches. Therefore, the searches can be divided by the set of interferometers being searched over. No times with only one interferometer were searched, but for times when all three pairwise combinations (H1H2, H1L1, H2L1), as well as triple-coincident time (H1H2L1) the loudest events were followed up to determine whether they might be detections of gravitational waves. There were no detections in this search. Additionally, the loudest events from H1L1, H2L1, and H1H2L1 were used to set

upper limits. H1H2 was not used due to the correlated transients from non-astrophysical disturbances in Hanford, which vetoes alone were not able to remove. This correlation of noise meant that calculating the background by sliding H1 with respect to H2 underestimated the false alarm rate, as the local disturbances did not appear coherently in the background as they did in the un-slid search. For this reason, H1 and H2 are slid together to estimate the H1H2L1 background, and H1H2 triggers are not used to calculate the upper limit.

Looking at the H1H2L1 triggers in Figure 4.6, there are ten coincident triggers in the first year of S5. They are plotted versus the time-slide background averaged over the number of time-slides, with error bars calculated for one standard deviation assuming Poissonian statistics (the square root of the number in each bin). None of the ten are vetoed by category 2 vetoes, and the background only decreases slightly. Category 3 vetoes remove two foreground triggers between 75 and 90 $\rho^2_{\rm eff}$ combined, and reduces the background such that the loudest candidate is no longer within the error bars, though it is still not statistically significant. Category 4 vetoes the loudest coincident trigger, as well as two more with lower statistic values, leaving the new loudest trigger less significantly above background than the loudest after category 3 was. A strong detection, were it present, would be obvious as a trigger with combined $\rho^2_{\rm eff}$ well above 100, and therefore extending off of the right edge of Figure 4.6, and of course not be vetoed by any category. A weaker detection might be at or somewhat above 100, which is above background less significantly.

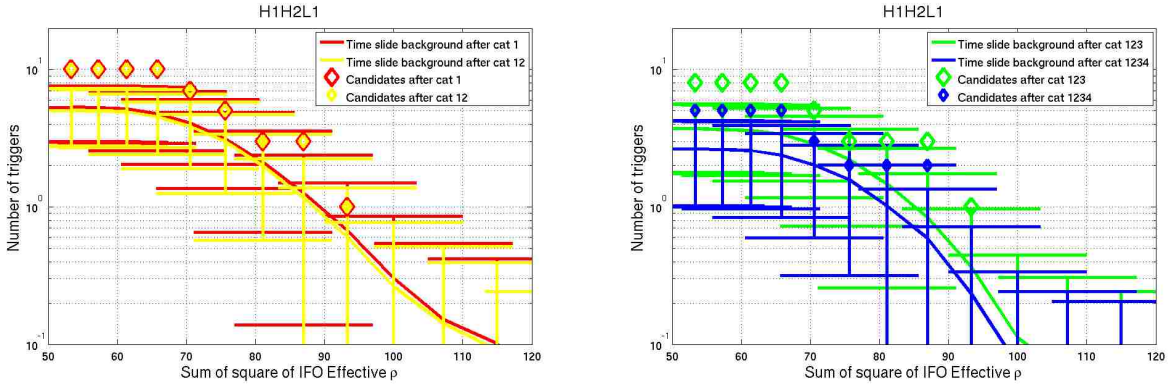

Figure 4.6: Cummulative histogram of the sum of the squares of the $\rho_{\rm eff}$ of the triggers found in coincidence in H1H2L1, and the expected background from 100 time-slides. Number in zero-lag and background number found per time-slide are plotted in red after category 1 vetoes, yellow after category 2 vetoes, green after category 3 vetoes, and green after category 4 vetoes. Error bars are one standard deviation assuming Poissonian statistics.

We desire to define the probability that a given candidate event is a random false alarm from statistical fluctuations of detector noise. The background estimation from time-slides can be used to calculate this false alarm probability (FAP). One can rank coincident triggers by using the background from time-slides to calculate the number of false alarms expected (FAN), which is the number of time-slide triggers that are of equal or louder combined $\rho^2_{\rm eff}$, normalized by the ratio of zero-lag to time-slide analysis time. Translating the triggers into FAN has the advantage that they can be compared against the same background, rather than for each set of post-veto times.

To calculate a false alarm probability (FAP), we simply assume that candidates are independent events that occur at some rate, and apply Poisson statistics. The probability

of seeing N triggers with some significance during time T, given a rate R, is

$$\mathrm{P} = \frac{(R \cdot T)^N \cdot \left(e^{-R \cdot T}\right)}{N!}. \tag{4.1}$$

Specifically, the probability of seeing $N = 0$ events is simply

$$\mathrm{P}(0) = e^{-R \cdot T}, \tag{4.2}$$

and the FAP is the probability of seeing one or more triggers, or

$$\mathrm{FAP} = 1 - e^{-R \cdot T}. \tag{4.3}$$

The rate R is the number of triggers in the time-slides (N_S) with equal or higher combined ρ_{eff}, divided by the time-slide total duration T_S. The analyzed time T for the first year of S5 was 0.42 years of science time after category 1, 0.41 years after category 2, 0.37 years after category 3, and 0.31 years after category 4. We can recast FAP as

$$\mathrm{FAP} = 1 - e^{-N_S \cdot \frac{T}{T_S}}, \tag{4.4}$$

Figure 4.7 shows the cumulative number of triggers versus the inverse FAN (IFAN)(12). Since the triggers are plotted in terms of expected number of zero-lag candidates as calculated from time-slides, the expected background is by definition $1/x$. With 100 time-slides, and with the 1 as the minimum sensible value for FAN, the largest sensible value for the IFAN is 100.

It can be observed that the IFAN of each candidate increases with veto categories consecutively applied until category 4, which vetoes a third of the triple coincident triggers, and a quarter of the science time, lowering the IFAN for the remaining triggers and removing the triggers with the highest ρ^2_{eff}. This is not unexpected, given the veto metrics for the component category 4 vetoes. The loudest candidates after each category of vetoes were followed up intensively, and were considered to be unlikely to be detections, consistent with their low statistical significance.

In particular, the loudest event surviving the first three categories was vetoed by the "H1H2 SCATTERING" flags, as well as the "DARM 11 13 dHz MEDTHRESH" and "DARM 09 11 dHz LOWTHRESH" flags, at category 4, indicating upconversion of seismic noise and scattered light between the interferometers were possible. These mechanisms were then verified by members of the LIGO CBC group, who found motion in the seismic channels tracked with disturbances in the H1 gravitational wave channel at low frequencies, which in turn occurred at the same times as significant noise transients in the sensitive band from ~ 60 to 100Hz.

Superimposed upon Figure 4.7 is a set of colored circles. These correspond to the simulated IFAR that would have been found for a H1H2L1 detection candidate with combined $\rho^2_{\mathrm{eff}} = 100$. This value is just more than the highest combined ρ^2_{eff} of the coincident triggers of 100. The initial inverse false alarm number for the simulated trigger is 3.3 after category 1 vetoes are applied, indicating that we would expect 0.30 such triggers per analysis. After categories 2, 3 and 4 the trigger IFAN rises to 3.8, 9.1, and 14, respectively. From Eqn. 4.4, we obtain FAP values of 26%, 23%, 11 %, and 6.8% evaluated after veto categories 1, 2, 3, and 4. The application of veto categories therefore reduces the false alarm probability by over 50% after categories 1 through 3 are applied. This shows us that the categories 1 through 3 are enough to make a trigger consistent with background into a still marginal but curious candidate.

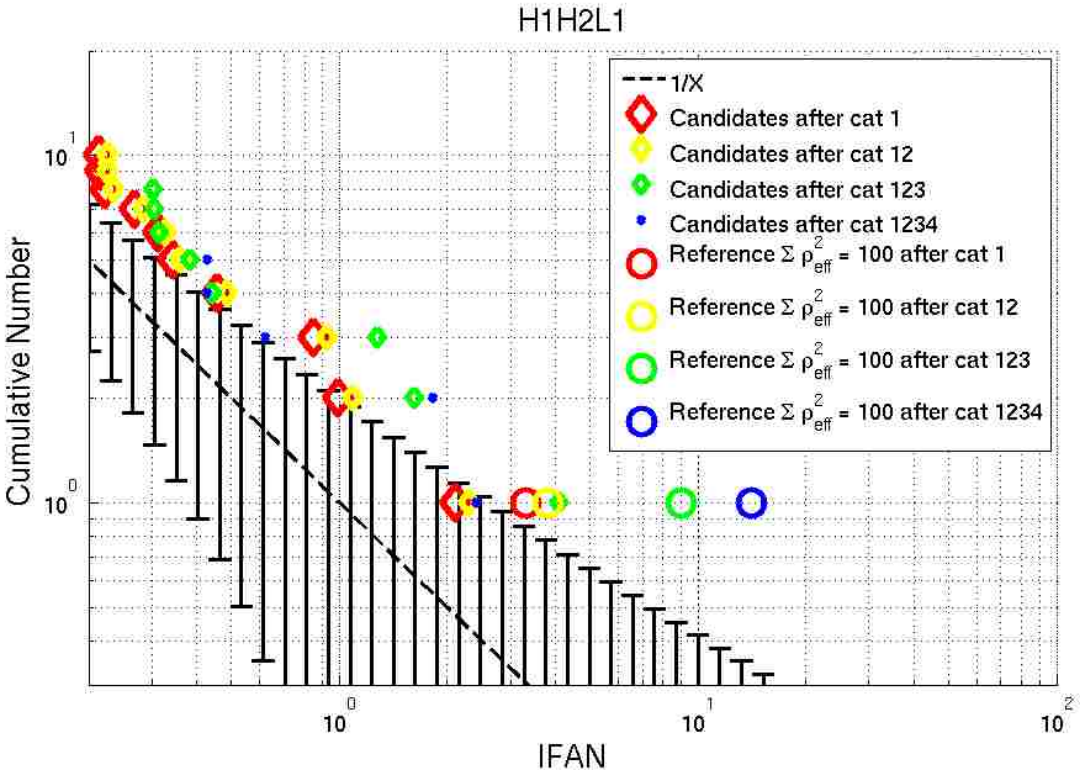

Figure 4.7: Cumulative histogram of the inverse false alarm number (IFAN) of the H1H2L1 coincident triggers, with a hypothetical reference candidate (circles) with combined $\rho^2_{\rm eff} = 100$ added to illustrate the effect of category vetoes on the IFAN of a candidate which survives vetoes. The diamonds are the coincident triggers colored in the usual manner; after category 1 is red, 2 yellow, 3 green, 4 blue. Also plotted as a dashed black line is the expected number of false alarms, which is by definition $1/x$. Poisson error bars are included.

Additionally, in H1H2L1 time, it is possible to detect triggers only in two of the detectors, in particular H1L1 detections are plausible due to H2 having half the sensitivity of the longer detectors. Figure 4.8 shows the IFAN for these coincident triggers. The most obvious is the single trigger after category 2 that is louder than any time-slide coincident triggers in category 2 times. This trigger was not a gravitational wave detection, as the follow-up revealed that the L1 component was in a science segment that had been marked in the detector notebook as not fit for searching, but that had not been added to the category 1 veto lists. The segment was so designated due the the presence of number loud noise transients, one of which is coincident with the un-shifted trigger, yielding a single interferometer ρ of 79.3, and a χ^2 value of 1560. This yielded a similar $\rho_{\rm eff}$ to the H1 trigger with a single interferometer ρ of 7.35, and a χ^2 value of 47.4. After category 3 vetoes, there are no remaining significant triggers. This event is discussed in Appendix B of (12).

As in the H1H2L1 case, a simulated injection has been included. The color scheme for circle representing the IFAN after category two vetoes were applied has been modified for visibility. The IFAN values after categories 1, 2, 3 and 4 are applied are 2.6, 5.6, 17, and 25,

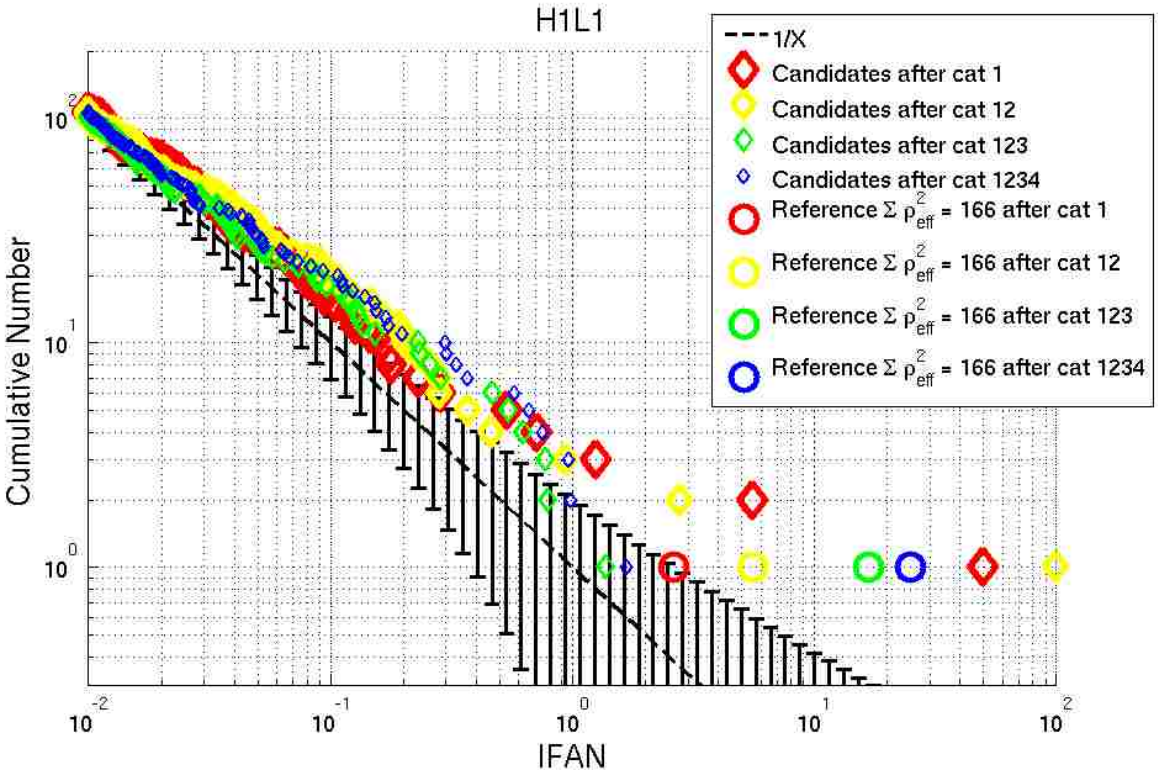

Figure 4.8: Cumulative histogram of the inverse false alarm number (IFAN) of the H1L1 coincident triggers, with a hypothetical reference candidate (circles) with combined $\rho^2_{\text{eff}} = 166$ added to illustrate the effect of category vetoes on the IFAN of a candidate which survives vetoes. The diamonds are the coincident triggers colored in the usual manner; after category 1 is red, 2 yellow, 3 green, 4 blue. Also plotted as a dashed black line is the expected inverse false alarm rate, which is by definition $1/x$. Poisson error bars are included.

corresponding to FAPs of 32%, 17%, 5.9%, 4.0% evaluated after veto categories 1, 2, 3, and 4. The increase from a statistically insignificant event, at roughly one standard deviation, to a interesting candidate shows the effect that reducing the background false alarm rate can have on a detection candidate.

Figure 4.9 shows the FAP values for the full range of relevant combined ρ^2_{eff} values for H1L1 coincident triggers. Combined statistic values below 110 are all buried in the background such that the FAP is essential 1. Values above 210 are similarly so large that they exceed the background, yielding the minimum possible FAP of 0.01, given 100 time-slides. In between, categories 2 and 3 reduce the FAP for a given candidate significantly, while category 4 does very little, as we expected from the veto metrics. The greatest reductions in FAP occur near statistic of 140, though the final FAPs here are not significant from a detection standpoint. For candidates with combined statistic from 180 to 200, the application of veto categories 1, 2 and 3 makes candidates that are mild outliers with FAPs of a few percent to interesting candidates with FAPs of order one percent or less.

The application of vetoes to reduce the background of as measured form time-slides is vital to finding interesting candidates for detection. The veto categories achieve significant reductions in background, revealing the significance of the loudest candidates above the background.

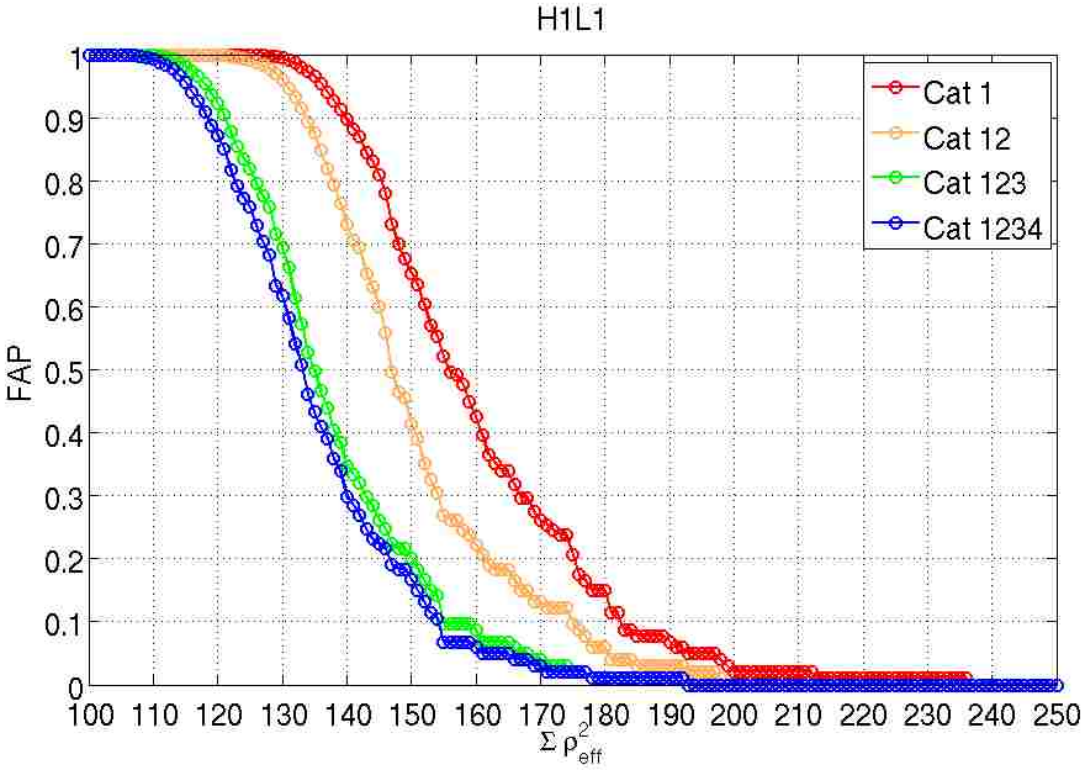

Figure 4.9: False alarm probabilities versus combined ρ^2_{eff} for H1L1 coincident triggers. Each plot has one line for each of the four veto categories.

5. Astrowatch

5.1 Introduction

The fifth Astrowatch run, or A5, took place following the end of S5. During A5, a group of graduate students maintained and operated the H2 interferometer on a best effort basis, while the Observatories' staffs focused on upgrading H1 and L1. The commissioning of the 4k interferometers meant that during A5, H2 was the most sensitive gravitational wave detector operating in the world, with a median range of ~ 7 Mpc. Astrowatch 5 officially began on March 1st, 2008, and was highlighted in APS news (34).

I was a member of the first crew of Astrowatchers, all graduate students within the LSC, arriving in January of 2008, and staying for six months. The six of us were myself, Evan Goetz (University of Michigan), Pinkesh Patel(California Institute of Technology), Phillip Roberts (Andrews University), Berit Behnke(Albert Einstein Institute, Hannover), and Junyi Zang (University of Michigan). During my stay, Matt West (Syracuse University), Szymone Steplewiski (Washington State University), Satya Mohapatra (Amherst University), and Adam Mullavy (The Australian National University) also took shifts. The shifts originally occurred from 10 PM to 6 Am the following day, with two astrowatchers on each shift. Later on in A5, these shifts were moved to start 6 PM and end at 2 AM, with the reasoning that this change made them more easily covered with the small number of students available, and avoided significant loss of livetime as the interferometer requires the least operator effort during the quiet pre-morning hours. This did turn out to have some consequences, as will be discussed in Chapter 5.2.

The GEO detector was also operational during these months with a percentage of time in science mode, or duty factor, of 80%. Despite this impressive robustness, GEO's sensitivity was significantly lower than H2. Searches for sources at large distances were unlikely to make any detections, as none were made in S5 with two interferometers that were twice as sensitive, and event rate is roughly proportional to volume, which therefore varies as the cube of the horizon range. Instead, A5 operated with the mission of providing sky coverage for nearby, rare events, such as supernovae and other high energy events that occur more often than coalescences, but are intrinsically weaker. No supernovae went off in the local group of galaxies during A5, but there was a particularly loud Soft Gamme Repeater dubbed SGR 0501+4516, which occurred in August of 2008. The data selection for this event was performed by myself and fellow graduate student Pinkesh Patel, and is detailed in Chapter 5.3.

Maintenance was performed weekly, with a set of regular tasks, so long as the interferometer was behaving normally. When there were malfunctions and other atypical behaviors, it was the responsibility of the "astrowatchers" to characterize it, to hopefully diagnose it, and if possible to correct it. Much assistance was given by the site staff at Hanford, but the ultimate responsibility was ours.

In this chapter, I will discuss the performance of H2, including the efforts required to maintain detector robustness and sensitivity. I will then describe the overall data quality system present during astrowatch. Finally, I will detail the specific investigations done to maximize available science data for analysis around the SGR.

For the purposes of this chapter, I will treat science mode and the SCIENCE data quality flag interchangeably (there were no category 1 vetoes). Additionally, as the UP state for a LIGO interferometer indicates that the detector had been put into low noise mode, the UP

state technically includes all SCIENCE times as well. Of interest in the remainder of this chapter is the utility of UP times not marked as science quality data, and so for convenience I will use the term "UP time" to refer to such times not included in the SCIENCE flag.

5.2 H2 Performance and Data Quality in A5

Figure 5.1 displays the sensitivity to binary neutron star systems in each minute, in units of Mpc at which such a binary with an average inclination and orientation would be detectable with a ρ of 8. This quantity is referred to within LIGO as the "sensemon" range, after the name of the software that calculates it online. Binary systems with more favorable position in the sky and orbit orientations can be detected with the same ρ up to larger distances; the maximum detectable distance with $\rho = 8$ is sometimes called the "horizon" distance and is 2.2 times larger than the average distance plotted here. Only the minutes that were entirely within science mode are shown. Between the end of S5 in October of 2007 and the start of A5 in January 2008, there was significant commissioning work performed on H1, which took the vast majority of the efforts of the on-site staff, and multiple months. In order to begin A5, H2 needed to be returned to its former sensitivity during S5, which was achieved in late February. Obvious from Figure 5.1 is a decrease in average range with time. Most of this was found to be due to an increase in the baseline ground motion in the 1 to 3 Hz band, caused by the spring runoff from thawing ice on the mountains gushing through a nearby dam.

There is also a gap starting on day 110 through 120, with only one science segment within it. H2 was mysteriously unstable during this time, and it was over month after H2 became operational again that I discovered elevated seismic motion in the 1-3 Hz BLRMS, primarily in the Z direction, and only in the LVEA. Figure 5.2 shows this, with the Z direction measured at the Hanford Y mid-station, the location of H2 ETMY, plotted for comparison. A significant increase in the seismic baseline starting at day 140 (again, the dam runoff, which fluctuated over the summer) is shown coincident at the end of the Y arm and the corner station, and has an deleterious effect on the sensemon range. The increase during the days 110 to 120 had even higher motion in the corner station, but no elevation elsewhere. Because the raw seismometer data, and indeed all raw data in A5, was only saved around UP or SCIENCE times, and days 110 to 120 were so very bad, there was insufficient information archived to follow up more on the possible cause of this loud and local motion.

The lack of science mode data starting in July (day 210 in Figure 5.1) was due to a major venting of the vacuum systems at the corner station, necessitating among other things the sealing of the steel gate valves to maintain the 4 km are vacuum while the corner was open to air. Overall, in the first six months of A5, there were about 330 segments containing ~ 44 days of SCIENCE, and 768 segments containing ~ 37 days of detector ready times (UP). Some of this UP time was being used for detector commissioning, calibration, or contained transients from environmental effects that make the data unsuited to search for gravitational wave detections. Not all of the UP time was unsuitable, however. Due to staffing constraints for A5, the detector was often in science mode at 2 to 4 AM Pacific time, and the departing astrowatcher would note the instrument was being locked in "unattended science mode". Often H2 would lose lock due to some short lived issue such as a small local earthquake, and the detector would automatically recover on its own to the UP state, and be operating normally, but no human was present to activate science mode.

Figure 5.3 shows both the percentages in UP and SCIENCE and a histogram of the sensitivity to BNS coalescences. We see that H2 is in science mode only 29% of the time, and but is UP an additional 24%. Additionally, from the histogram we see that most of the

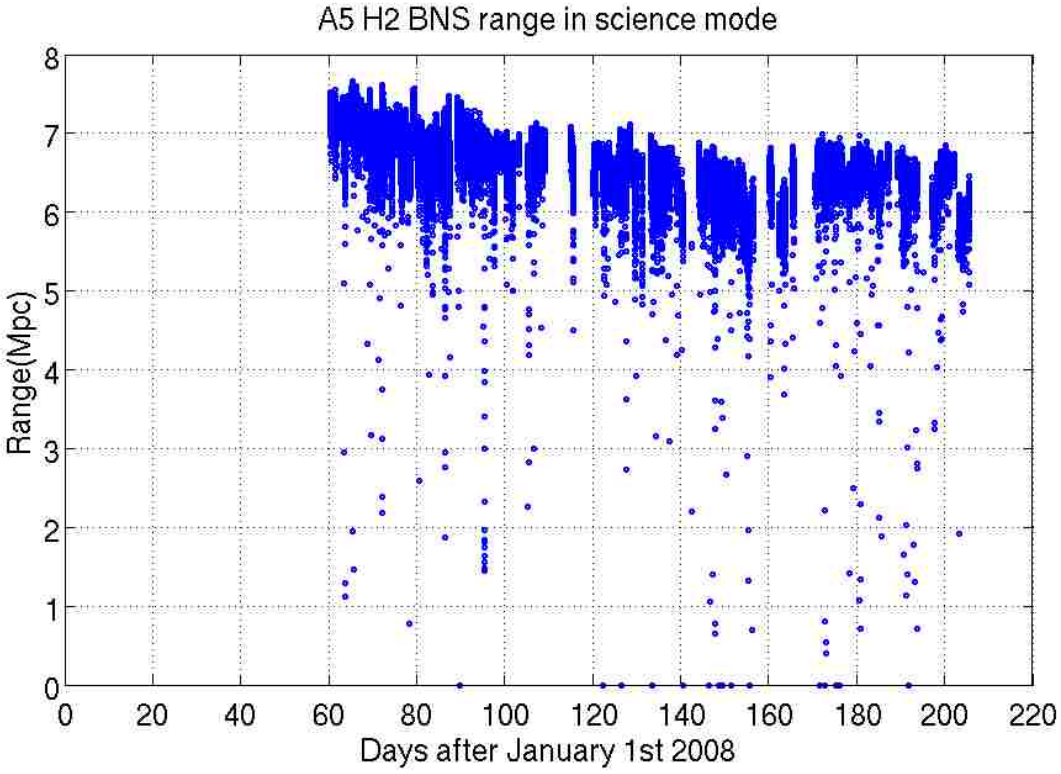

Figure 5.1: For the noise spectrum in each minute of SCIENCE data in the first 6 months of A5, the distance in Mpc at which a BNS system of average orientation and inclination would be detected with a ρ of 8 is plotted versus time in days. Median range of 6.6 Mpc, maximum of 7.6 Mpc.

time these UP time segments have sensitivity commiserate with the science mode segments, though the tail to lower sensemon values is a factor of 10 more populated.

5.3 Data Quality Vetoes for the Search for SGR 0501+4516

The first soft gamma repeaters (SGRs) were classified as short duration gamma ray bursts (GRBs) with soft (low frequency) spectra (35). It was not until the first time such an object was observed to re-activate that it became apparent they were a different type of object. SGRs were found to sporadically emit bursts of radiation, or flares, followed by minutes of pulsating soft gamma ray emission. It has been determined that the source objects are likely magnetars, neutron stars with extremely high magnetic fields. The flares, separated by days, weeks, or even years, are reorganization of structures on the magnetar surface as frozen in magnetic field lines unwind, and the oscillatory period of the soft gamma ray emission that follows is the same as the rotational period of the star.

Even though S5 was a science run with more sensitive detectors, for sufficiently loud astrophysical events, A5 could be used to make stronger statements. At 0.8 ± 0.4Kpc further from the galactic center than the Earth, SGR 0501+4516 was more than an order of

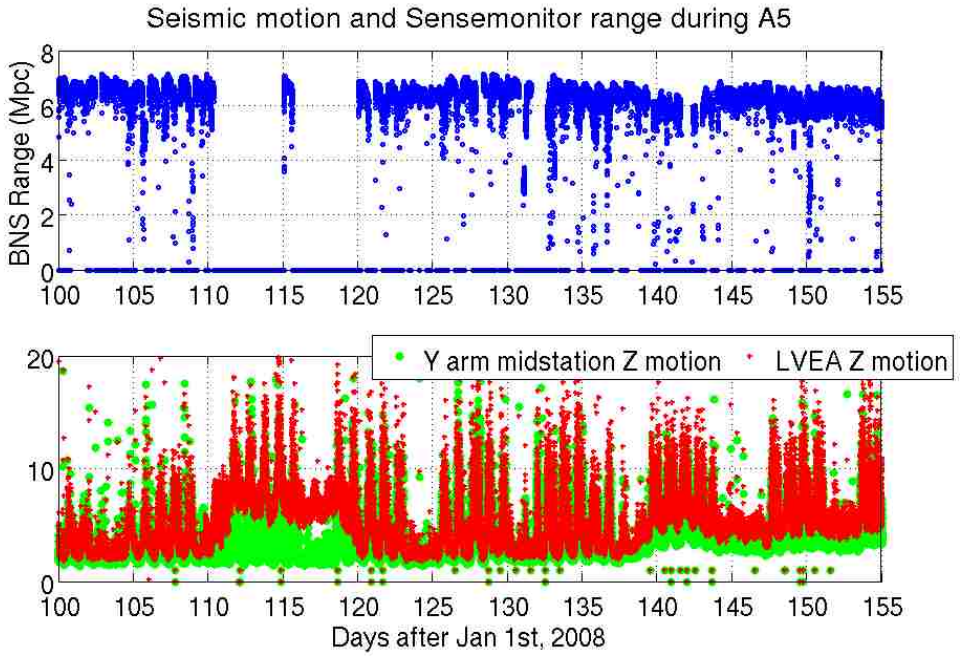

Figure 5.2: 1 to 3 Hz BLRMS in the Z direction measured at the Y and corner station plotted on the same timescale as the sensemon range.

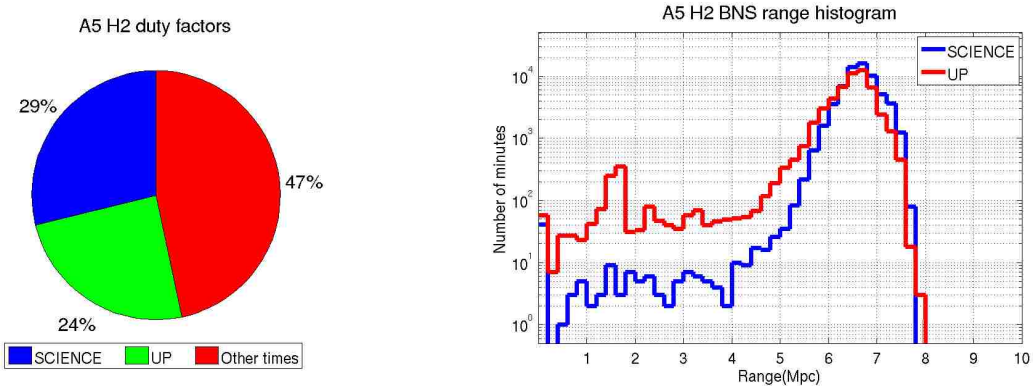

Figure 5.3: At left, percent of A5 spend in SCIENCE time, in ready for science time (UP), and not ready. At right, calculated for the noise spectrum in each minute of SCIENCE and UP data in the first 6 months of A5, the distance in Mpc at which a BNS system of average orientation and inclination would be detected with a ρ of 8.

magnitude closer than the nearest SGR that occurred during S5 (36). The final analysis of this event is being carried on by the LSC, led by Peter Kalmus at Columbia University, and is not yet published.

In collaboration with Pinkesh Patel, I examined data segments between August 21st, 2008 at 00:00 UTC and September 5th, 2008 at 00:00 UTC for suitability for searches for gravitational waves. Astrowatch was performed on a best-effort basis, but still we require that any search making scientific claims meet a minimum baseline of data quality standards.

As Figure 5.4 shows, H2 was in the UP state for almost as long as it was in science data. Of the more than 100 outburst times provided us, 37 were in science mode, and 31 were contained in UP time. As discussed in the previous section, we expected that many of these outburst are in data of searchable quality, but this needed to be verified. The final set of time searched was constructed by taking the union of the science time with the UP times that passed inspection, removing times vetoed by data quality flags and keeping only data segments longer than 120 seconds.

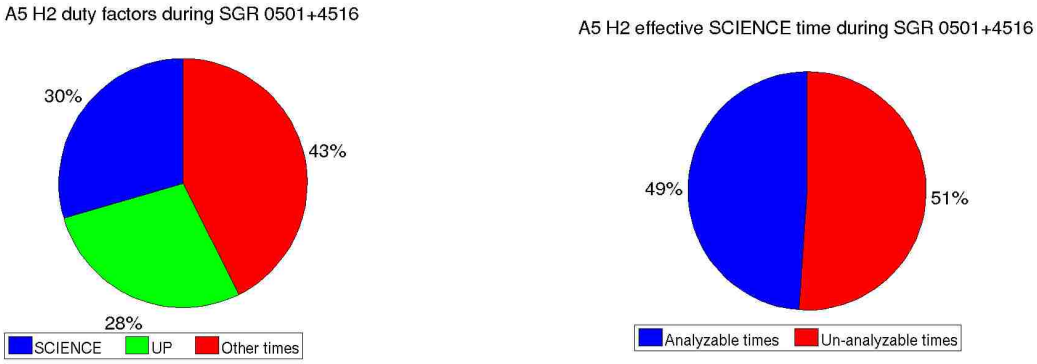

Figure 5.4: At left, percent of A5 spend in SCIENCE time in blue, in ready for science time (UP) in green, and all other times in red. At right, percent of the first 6 months of A5 SCIENCE and UP data that is analyzable in blue, and the rest of A5 time in red.

There were very few data quality flags produced for A5, as it was not a true science run, but a opportunistic safeguard against missing unique nearby events. While automating production of data quality flags found to be useful in S5 was a priority of the LSC detector characterization group, only those flags that were online at the end of S5 were available for the SGR outburst times.

We imposed a cut on the data for any significant data quality flags that were active, and these times were not searched. Not all of the data quality monitors we had at our disposal during S5 were present during A5 as they were at that time generated manually, however the monitors we did have automated were among the most significant in terms of data quality in H2 in S5. The available data quality flags we used are listed, along with their deadtime, in table 5.1. We applied these vetoes by simply removing times in UP and SCIENCE that were flagged. Also defined, though not obviously useful, were flags that included times when H2 was locked, and H1 was not. No window padding was applied, as the presence of impulsive transient noises does not impede making detections seconds away from SGR search as it does in the CBC search. These flags were a minor factor in the search, as only 0.14% of the searched time was vetoed.

In order to evaluate the UP times for science worthiness, our primary tool was the detector elogs and the automated Figures of Merit. We then examined the elog, sensemon range, and the seismic BLRMS trends, and annotated the list of UP segments. Data quality concerns either led to discarding some portion of the UP segments outright, or further

Table 5.1: Data quality flags both relevant and automatically generated for H2 during A5. No window paddings were requested.

Name	Deadtime(seconds)
H2 ASC Overflow	82
H2 ASI CORR OVERFLOW	471
H2 LSC OVERFLOW	0
H2 PD Overflow	160
H2 SEVERE LSC OVERFLOW	149
H2 Wind Over 30MPH	339
Combined flags	863

followup investigation. We divided the 15 days into epochs described by the continual presence of data quality concerns, or lack thereof. Tables 5.2 and 5.3 are the notes taken by us for epochs in the first and second week, respectively. These tables list the start and stop time of each epoch, any concerns present, and the resulting decisions on including UP segments in the analysis.

Table 5.2 lists 8 epochs over 5 days. There were two instances of site staff being present in the LVEA during UP times, but neither case gave cause for concern, as they were not in the vicinity of sensitive H2 components, but rather sensitive H1 components, and were not generating significant ground motion through use of machinery. There was one (controlled) detonation at a nearby site in Hanford, and the 20 minutes surrounding this event were excised. The rest of the UP time was sufficiently quiet to be used.

Table 5.3 lists 9 epochs in as many days. The first of these contained times when the damping loop gains for MICH and PRC, as well as the power settings for TCS, were being tuned. These were removed from the UP time lists, and the rest of the time was stable. There were two additional epochs during which site staff were working in the LVEA, one of which was problematic enough to warrant removal of some times. There were two other segments of concern, and of less than one hour each. One contained scattering from H1, and in the other the H2 main laser power was being modified every 10 minutes.

All told, we were able to validate the majority of the UP time for use in the search. Figure 5.4 shows the effective science duty factor increase from 30% to 49%. Figure 5.5 shows the BNS range for science and up time in blue and green, and the times used to search are highlighted in magenta. We recovered all of the UP segment outbursts, increasing the analyzed outbursts from 37 in Science, to 68 in final segments. It should be noted that this type of validation, while always possible for interesting astrophysical events that occur during times when one or more detectors was in low noise mode but not science mode, is unlikely to be as necessary during a science run, when far less searchable data is marked only as UP time.

5.4 Conclusions from Astrowatch 5

Unlike in a science run, the attention of the Observatory staff and LSC, and in particular the detector characterization group, was not focused on A5. Due to this, many resources normally available were absent, in particular the automated data monitoring tools (DMT)

Table 5.2: First week, from August 21st to 27th, for which we characterized the data quality, primarily of the UP segments, for suitability for the search for gravitational waves from SGR 0501+4516. Each row is a sub-epoch of this week, where the columns include the start and stop times of the epoch, the initial concerns worth investigating, and the final outcome from the examination.

UTC Start time - UTC end time	comments	decision
Aug 20 16:00:00 UTC - Aug 21 16:00:01 UTC	People in the LVEA working on TCS. Need to verify they did not disturb H2	No use of heavy machinery, nor proximity to H2 optics. Use UP segments in this interval.
Aug 22 09:14:45 UTC - Aug 22 14:22:15 UTC	No one on site, should be good data.	Use UP segments in this interval.
Aug 22 14:22:15 UTC - Aug 23 08:42:20 UTC	People in LVEA near HAM6 and TCSX for H2. Data should still be good, subject to seismic noise.	No use of heavy machinery, nor proximity to H2 optics. Use UP segments in this interval.
Aug 23 16:26:27 UTC - Aug 23 21:06:57 UTC	Segments 289 and 290 are the same with 50 seconds of UP separating them, and should be used in their entirety.	Use UP segments in this interval.
Aug 23 21:50:00 UTC - Aug 23 22:10:00 UTC	Detonation at Hanford, don't use the data in 10 minutes surrounding this time stamp.	Removed appropriate segment from UP list.
Aug 23 22:05:00 UTC - Aug 24 16:20:00 UTC	Very good data, use all.	Use UP segments in this interval.
Aug 24 16:20:00 UTC - Aug 24 23:12:00 UTC	Many computer problems and reboots, don't use any data during this time. Its not trustworthy.	No segments present to remove.
Aug 24 23:12:00 UTC - Aug 25 14:08:00 UTC	No one was around, but not many lock stretches in any case. DAQ issues existed with H1 OMC computers. H2 data should be usable though.	Use UP segments in this interval.

Table 5.3: Second week, from August 27th to September 3rd, for which we characterized the data quality, primarily of the UP segments, for suitability for the search for gravitational waves from SGR 0501+4516. Each row is a sub-epoch of this week, where the columns include the start and stop times of the epoch, the initial concerns worth investigating, and the final outcome from the examination.

UTC Start time - UTC end time	comments	decision
Aug 25 14:08:00 UTC - Aug 26 08:45:30 UTC	TCS tuning + MichDamp and PRCDamp tuning during part of UP time. We can use TCS power and MICH/PRC Damp Gains to identify these intervals. TCS tuning times are usable, except during the power setting changes themselves. Some broadband noise between 100-300 Hz, below interesting frequencies for the SGR search.	Removed times when the loop damping gains were being tuned.
Aug 26 08:45:30 UTC - Aug 27 08:45:30 UTC	Data should be ok. Seismic was elevated especially around 1-3 Hz.	Seismic spikes broke lock, no UP data contained them. Use UP segments in this interval.
Aug 27 08:45:30 UTC - Aug 28 08:32:30 UTC	H1 was probably glitching us again. Usable data otherwise.	One brief segment of science data stepped down in range, due to scattering. Other segments fine.
Aug 28 08:32:30 UTC - Aug 29 00:35:30 UTC	Usable data.	Use UP segments in this interval.
Aug 29 00:35:30 UTC - Aug 29 01:25:30 UTC	Power was varying, would not use.	Removed appropriate segment from UP list.
Aug 29 01:25:30 UTC - Aug 29 15:46:19 UTC	Good data.	Use UP segments in this interval.
Aug 29 15:46:19 UTC - Aug 29 17:46:19 UTC	Work around HAM6.	No use of heavy machinery, nor proximity to H2 optics. Use UP segments in this interval.
Aug 29 17:46:19 UTC - Aug 30 08:24:19 UTC	People in LVEA. Might not be great data. Science mode should be trusted of course.	Removed appropriate segment from UP list.
Aug 30 08:24:19 UTC - Sep 03 00:00:00 UTC	Good data, and then not much data to evaluate.	Use UP segments in this interval.

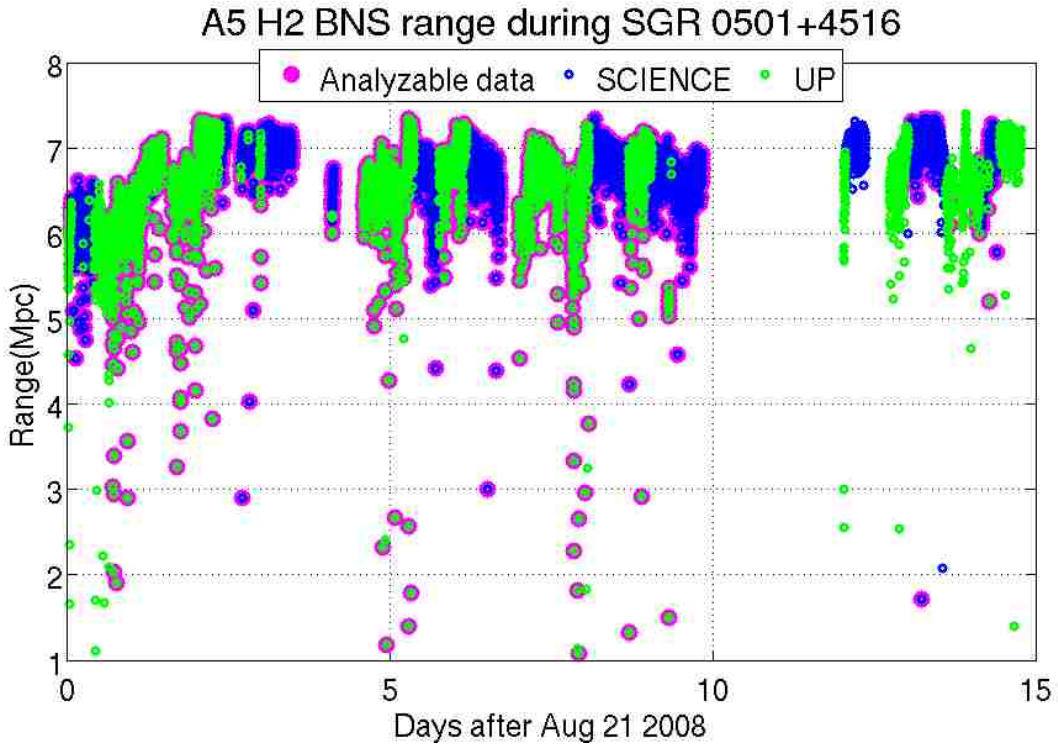

Figure 5.5: Sensemon range for two weeks of A5, during which SGR 0501+4516 emitted gamma ray flares. Minutes during science mode are plotted in blue, minutes during UP times are plotted in green, and times in science and UP with sufficient data quality to be analyzed are highlighted in magenta.

that produce data quality flags were often malfunctioning, and control room monitoring of data was occurred for half the day or less. Searches performed on this data require vastly more manual inspection of data, and therefore only astrophysical events of rare and significant intensity provide the motivation necessary for this labor. This situation is less than ideal, yet infinitely better than completely lacking sky coverage with modern interferometric gravitational wave detectors for years at a time, potentially during once in a lifetime events.

When Advanced LIGO begins operation, the LSC will have to characterize these fundamentally new detectors. Successful operation will require robust automated data quality, and staff on-site to maintain this infrastructure. During the S6 run, significant progress has been made in such automation, with all of the algorithms from S5 that marked frequent transients transitioned to online running. While Advanced LIGO will certainly have new and previously unimagined problems in its first years of operation, those problems that cannot simply be solved will be marked by new automated algorithms, in the same way that the previously discovered algorithms for finding data quality issues have been automated with data monitoring software.

In the future regime of regular detections with Advanced LIGO, it is conceivable that the current focus by hundreds of scientists on close inspection of LIGO data transients of non-astrophysical origin will not be sustained. It will be critical that some evaluation be performed of the data in an ongoing, low latency manner, to determine what data segments

will be science worthy, and what intervals with these segments may be suspect. This data validation, was necessary for A5, as much as half of the searchable data was not marked as science mode, but far less should be required given the round the clock presence of Observatory staff to ensure that the all worthy UP times are marked as science, and all the data monitoring software is functioning nominally.

6. Conclusion

Gravitational radiation, the extremely weak perturbation of space-time caused by a the time-variation of the quadrapole moment of a mass distribution, promises to be a new frontier in astrophysics when it can be reliably detected. Significant challenges remain before this can be a reality. For the Laser Interferometer Gravitational-wave Observatory (LIGO), a US national lab funded by the National Science Foundation, to make the first direct measurements of gravitational waves the detectors will need to increase their sensitivity over that of initial LIGO (1) by an order of magnitude (15). Even this improvement will not be sufficient if the data collected is contaminated with large numbers of transient noises of non-astrophysical origin, which is why the proper cataloging and vetoing of these transient glitches is vital.

Chapter 2 discusses the control system and equipment malfunctions, as well as coupling from ground motions and electromagnetic fields, which are the most common noises that detract from the LIGO data quality. An example of one such investigation, that I performed, to flag the coupling of ground motion from trains passing Livingston, Louisiana into the gravitational wave channel shows the connection between data quality and increased rate of false alarms in the detector.

In Chapter 3, I discuss converting this data quality information into vetoes for the Compact Binary Coalescence (CBC) search. Vetoing data is not without cost, as the less time available to search for gravitational waves, the time there is in which a gravitational wave can be discovered. Because of this fact, and because not all useful data quality information was equally effective, I had to determine how to classify these flags into categories to be applied sequentially.

In Chapter 4 I show the results of employing these methods in practice, on the search for CBC's with total binary system mass below 35 solar masses in the LIGO's 5th, and longest, science run (S5). The best chance for gravitational wave detection to date lie in searching this data, and the most well understood and promising source candidate were CBCs. While no detections were made, vetoes made a significant impact, namely that binary neutron star and black hole sources that would have been marginal without vetoes applied would have become significant and perhaps detectable.

Data quality is not only important for the flagship searches of the best science runs. In fact, such efforts are required as much, if not more, for runs such as A5, which took place after S5. The astrowatch program that began after S5, called A5, was conducted by graduate students on a best effort basis, tasked with maintaining and operating the 2km Hanford detector (H2) interferometer, while the Observatory staff focused on upgrading the 4km H1 and L1 detectors. During A5, H2 was the most sensitive gravitational wave detector operating in the world, providing the ability to detect gravitational waves from exceptionally rare and powerful astrophysical events, such a nearby galactic supernovae, should they occur while the larger detectors were not operational. While there were no such supernovae during A5, one interesting and somewhat rare event did occur during A5, namely the appearance of and outbursts from a soft gamma-repeater (SGR) occurred at a distance of less than 5 Kpc, with multiple outbursts occurring in a two week interval from August 21st to September 3rd of 2008. Unfortunately, nearly half of this data was not initially validated as science mode, and little in the way of data quality flag information was available. The investigations performed and recommendations made for data quality vetoes for this fortnight of A5 were described in detail in Chapter 5, which resulted in nearly twice as many outbursts being analyzable as would have been otherwise.

Throughout the years of LIGO's operation, the LIGO scientific collaboration (LSC) has developed powerful and complex search algorithms to detect different types of gravitational wave signals in the data. Despite this sophistication, it often happens that the loudest events surviving these pipelines are transients of non-astrophysical origin that have been, or should have been removed by data quality checks. From the "airplane" event in the 2nd science run burst search (32), to the glitchy L1 time in the S5 first year low mass CBC search, it is clear that signal consistency checks and background analysis alone cannot make the searches behave as if the data were effectively Gaussian and stationary. I have shown that the application of categories of vetoes, derived from data quality flags, increases the ability to detect a candidate gravitational wave signal significantly, though no such signal has yet been detected.

Bibliography

[1] A. Abramovici, W.E. Althouse, R. Drever, Y. Gursel, S. Kawamura, F. Raab, D. Shoemaker, L. Sievers, R. Spero, K. Thorne, R. Vogt, R. Weiss, S. Whitcomb, M. Zucker, *Science* **256** (1992) 325.

[2] URL `http://www.ligo.org`

[3] Peter R. Saulson, *Fundamentals of Interferometric Gravitational Wave Detectors*, World Scientific, Singapore, 1994

[4] J. P. Krisch, *Physics 435 Lecture 23-24* , (December 2003).

[5] J. B. Hartle, *Gravity: An Introduction to Einstein's General Relativity*, Addison-Wesley, San Francisco, CA, (2003).

[6] E. Cappellaro, R. Evans, M. Turatto, Astron.Astrophys.351:459,1999

[7] R. A. Hulse, J. H. Taylor, *ApJ* **195** (1975) L51.

[8] Abbott B *et al.* (LIGO Scientific Collaboration) 2009 *Rept. Prog. Phys.* **72** 076901 (*Preprint* `arXiv:0711.3041`)

[9] H Grote (for the LIGO Scientific Collaboration) 2008 Class. Quantum Grav. 25 114043

[10] F Acernese et al 2008 Class. Quantum Grav. 25 114045

[11] Rana Adhikari, 2004 *Sensitivity and Noise Analysis of 4km Laser Interferometric Gravitational Wave Antennae*, Ph.D. thesis Massachusetts Institute of Technology

[12] Abbott B *et al.* (LIGO Scientific Collaboration) 2009 *Phys. Rev. D* **79** 122001 (*Preprint* `arXiv:0901.0302`)

[13] Abbott B *et al.* (LIGO Scientific Collaboration) 2009 *Phys. Rev. D* **80** 047101 (*Preprint* `arXiv:0905.3710`)

[14] J. R. Smith for the LSC, *The path to the enhanced and advanced LIGO gravitational-wave detectors*,Class.Quant.Grav.26:114013,2009

[15] *Advanced LIGO Reference Design*, LIGO Tech. Rep. M060056, 2007. URL `http://www.ligo.caltech.edu/docs/M/M060056-08/M060056-08.pdf`

[16] Wainstein L A and Zubakov V D 1962 *Extraction of signals from noise* (Englewood Cliffs, NJ: Prentice-Hall)

[17] Allen B, Anderson W G, Brady P R, Brown D A and Creighton J D E 2005 FINDCHIRP: An algorithm for detection of gravitational waves from inspiraling compact binaries (*Preprint* `arXiv:gr-qc/0509116`)

[18] Owen B J and Sathyaprakash B S 1999 *Phys. Rev. D* **60** 022002

[19] Abbott B *et al.* (LIGO Scientific Collaboration) 2007 Tuning matched filter searches for compact binary coalescence Tech. Rep. LIGO-T070109-01 URL `http://www.ligo.caltech.edu/docs/T/T070109-01.pdf`

[20] Abbott B *et al.* (LIGO Scientific Collaboration) 2008 *Phys. Rev. D* **77** 062002 (*Preprint* `arXiv:0704.3368`)

[21] Allen B 2005 *Phys. Rev. D* **71** 062001

[22] Brown D A 2004 *Search for gravitational radiation from black hole MACHOs in the Galactic halo* Ph.D. thesis University of Wisconsin–Milwaukee

[23] Blackburn L *et al.* 2008 *Class. Quant. Grav.* **25** 184004 (*Preprint* `arXiv:0804.0800`)

[24] E. J. Daw, J. A. Giaime, D. Lormand, M. Lubinski and J. Zweizig *Long term study of the seismic environment at LIGO* Class.Quant.Grav. 21 (2004) 2255-2273

[25] C. M. R. Fowler *The solid earth: an introduction to global geophysics* 1974

[26] Philip R. Bevington, D. Keith Robinson *Data Reduction and Error Analysis for the Physical Sciences*, Mcgraw-Hill, New York, 2003

[27] Chatterji S, Blackburn L, Martin G and Katsavounidis E 2004 *Class. Quant. Grav.* **21** S1809–S1818 (*Preprint* `arXiv:gr-qc/0412119`)

[28] Christensen N *et al.* (LIGO Scientific Collaboration) 2005 *Class. Quant. Grav.* **22** S1059–S1068

[29] Christensen N, Shawhan P and González G 2004 *Class. Quant. Grav.* **21** S1747–S1755

[30] Abbott B P *et al.* (LIGO Scientific) 2009 *Phys. Rev.* **D80** 102001 (*Preprint* `0905.0020`)

[31] Slutsky J *et al.* 2010 *Class. Quant. Grav.*, to be published in July 2010.

[32] Abbott B *et al.* (LIGO Scientific Collaboration) 2005 *Phys. Rev. D* **72** 062001

[33] Abbott B *et al.* (LIGO Scientific Collaboration) 2010 Data quality and veto choices of S5 lowmass CBC searches Tech. Rep. LIGO-T1000056-v2 URL `https://dcc.ligo.org/cgi-bin/DocDB/ShowDocument?docid=8982`

[34] Calla Cofield, Astrowatch Keeps LIGO's Eyes on the Sky URL `http://www.aps.org/publications/apsnews/200808/ligo.cfm`

[35] Woods, P. M., & Thompson, C. 2004, in *Compact Stellar X-Ray Sources*, ed. W. G. H. Lewin & M. van der Klis (Cambridge:Cambridge Univ. Press)

[36] Abbott B *et al.* (LIGO Scientific Collaboration), Astrophys. J. 701 (2009) L68-L74

[37] Jerry B. Marion, *Classical Dynamics of Particles and Systems*, 2nd Ed. (1970).

[38] David Shoemaker, 2009, LIGO-M080375-v7 URL `https://dcc.ligo.org/public/0002/M080375/007/LIGO-M080375-V7%20%28Abbreviations%20And%20Acronyms%29.pdf`

Appendix A: Copyright Permissions

Copyright permission for (31) that contains most of the content in Chapter 3, and some content spread between chapters 1, 2, and 4:

Ref: : CQG/363501/PAP/249871

ASSIGNMENT OF COPYRIGHT and DECLARATION OF RESPONSIBILITY

1. IOP Publishing Ltd ("the Publisher") agrees to publish

Manuscript title: Methods for reducing false alarms in searches for compact binary coalescences in LIGO data ("**The Article**") written by

Names of all Authors: J Slutsky, Lindy Blackburn, Duncan A Brown, L Cadonati, J Cain, Marco Cavaglia, Shourov Chatterji, Nelson Christensen, M Coughlin, Shantanu Desai ("**the Named Authors**")

in the following journal: Classical and Quantum Gravity ("**the Journal**")

2. Transfer of Copyright Agreement

2.1 On acceptance for publication the undersigned author(s) ("Author") of the Article assigns exclusively to IOP worldwide copyright in the Article for the full term and for all media and formats in all material published as part of the Article, which expression includes but is not limited to the text, abstract, tables, figures and graphs, but excludes any supplementary material.

2.2 If any of the Named Authors are Government employees, on acceptance for publication the Author shall grant IOP a royalty free exclusive licence for the full term of copyright for all media and formats to do in relation to the Article all acts restricted by copyright worldwide.

2.3 On acceptance for publication the Author shall grant IOP a royalty free non-exclusive licence for the full term of copyright for all media and formats to do in relation to any supplementary material deemed to be part of the Article all acts restricted by copyright worldwide.

3. Author Rights

3.1 IOP grants the Named Authors the rights specified in 3.2 and 3.3. All such rights must be exercised for non-commercial purposes. If possible should display citation information and IOP's copyright notice, and for electronic use best efforts must be made to include a link to the on-line abstract in the Journal. Exercise of the rights in 3.3 additionally must not use the final published IOP format but the Named Author's own format (which may include amendments made following peer review).

3.2 The rights are:

3.2.1 To make copies of the Article (all or part) for teaching purposes;

3.2.2 To include the Article (all or part) in a research thesis or dissertation;

3.2.3 To make oral presentation of the Article (all or part) and to include a summary and/or highlights of it in papers distributed at such presentations or in conference proceedings; and

3.2.4 All proprietary rights other than copyright.

3.3 The additional rights are to:

3.3.1 Use the Article (all or part) without modification in personal compilations or publications of a Named Author's own works (provided not created by third party publisher);

3.3.2 Include the Article (all or part) on a Named Author's own personal web site;

3.3.3 Include the Article (all or part) on web sites of the institution (including its repository) where a Named Author worked when research for the Article was carried out; and

3.3.4 Include the Article (all or part) on third party web sites including e-print servers, but not on other publisher's web sites.

Signature

In signing this Agreement the Author represents and warrants that the Article is the original work of the Named Authors, it has not been published previously in any form (other than as permitted under clause 3.2.2 which fact has been notified to IOP in writing), all Named Authors have participated sufficiently in the conception and writing of the Article, have received the final version of the Article, agree to its submission and take responsibility for it, and submission has been approved as necessary by the authorities at the establishment where the research was carried out.

The Author warrants that he/she signs this Agreement as authorised agent for all Named Authors and has the full power to enter into this Agreement and to make the grants it contains, that the Article has not been and will not be submitted to another publisher prior to withdrawal or rejection, it does not infringe any third party rights, it contains nothing libellous or unlawful, all factual statements are to the best of the Author's knowledge true or based on valid research conducted according to accepted norms, and all required permissions have been obtained in writing.

All Named Authors assert their moral rights.

Author's signature ..... Date 6/10/2010

Signature on behalf of Institution ..... Date .....

Note that if the Article was prepared as part of a Named Author's duties for their institution this Agreement must be signed by their institution as Author.

Appendix B: Acronym List

Table 6.1: Partial LIGO Acronym List (38)

Acronym	Meaning
AdL	Advanced LIGO
AdvLIGO	Advanced LIGO
ASC	Alignment Sensing / Control (detector subsystem)
AWG	Arbitrary Waveform Generator
BBH	Binary Black Hole pair
BH	Black Hole
BNS	Binary Neutron Star pair
BS	Beamsplitter(optical component)
BSC	BeamSplitter Chamber (large vacuum chamber)
CBC	Compact Binary Coalescence
CCD	Charged Coupled Device
CIT	California Institute of Technology or Caltech
DAQ	Data Acquisition, Diagnostics and Contols (AdvLIGO Subsystem name)
DARM	Differential Arm signal (main interferometer output signal for GW signal)
DMT	Data Monitoring Tool
eLIGO	Enhanced LIGO
ETM	End Test Mass (optical component); ETMy, ETMx for x or y 'arm'
FFT	Fast (Discrete) Fourier Transform
FM	Fold Mirror
GEO	British-German Cooperation for Gravity Wave Experiment
GPS	Global Positioning System
GW	Gravitational Wave
H1	Hanford 4K Interferometer
H2	Hanford 2K Interferometer (to be revised to 4K by AdvLIGO)
HAM	Horizontal Access Module
HEPI	Hydraulic External Pre-Isolator, and element of the SEI
HVAC	Heating Ventilation and Air Conditioning
Hz	Hertz

Table 6.2: Partial LIGO Acronym List, continued (38)

Acronym	Meaning
I/O	Input/Output
ITM	Input Test Mass (optical component); ITMx, ITM y for y or x 'arm'
kpc	Kiloparsec
L1	Livingston 4km Interferometer
LA	Louisiana
LAL	LIGO Algorithm Library
LHO	LIGO Hanford Observatory
LIGO	Laser Interferometer Gravitational-Wave Observatory
LISA	Laser Interferometer Space Antenna
LLO	LIGO Livingston Observatory
LMXB	Low-Mass X-Ray Binary
LSC	Length Sensing / Control (detector subsystem)
LVEA	Laser and Vacuum Equipment Area (of the LIGO observatories)
MC	Mode Cleaner
MIT	Massachusetts Institute of Technology
Mpc	Megaparsec
NS	Neutron Star
OMC	Output Mode Cleaner
OSEM	Ootical Sensor Electromagnetic Motor (suspension sensor/actuator unit)
PD	PhotoDiode
PEM	Physics Environment Monitoring
PRC	Power Recycling Cavity
PRM	Power Recycling Mirror
PSL	Pre-Stabilized Laser (detector subsystem)
PZT	Piezo-electric Transducer (mechanical hardware)
QPD	Quadrant Photo Diode
RM	Recycling Mirror
RMS	Root mean square
rtHz	noise or signal level in a one Hz bandwidth (read 'per root hertz')
SEI	Seismic Isolation
SUS	Suspension Subsystem (sometimes also Suspension assembly)
TAMA	Japanese Interferometric Gravitational-Wave Project
TCS	Thermal Compensation System
VIRGO	French-Italian Laser Interferometer Collaboration
WA	Washington
WFS	Wave Front Sensors

Vita

Jacob Slutsky was born in Detroit, Michigan, in 1982. He attended the University of Michigan, in Ann Arbor, from 2000 to 2004, and entered Louisiana State University pursuing his doctorate in 2004, recieving a Master of Science in physics degree along the way in 2008.